

Scale up of surfactant alternating gas foam processes

Salazar Castillo, Rodrigo

DOI

[10.4233/uuid:d249d287-dd0e-4db6-86b2-c013c172dd92](https://doi.org/10.4233/uuid:d249d287-dd0e-4db6-86b2-c013c172dd92)

Publication date

2019

Document Version

Final published version

Citation (APA)

Salazar Castillo, R. (2019). *Scale up of surfactant alternating gas foam processes*. [Dissertation (TU Delft), Delft University of Technology]. <https://doi.org/10.4233/uuid:d249d287-dd0e-4db6-86b2-c013c172dd92>

Important note

To cite this publication, please use the final published version (if applicable).
Please check the document version above.

Copyright

Other than for strictly personal use, it is not permitted to download, forward or distribute the text or part of it, without the consent of the author(s) and/or copyright holder(s), unless the work is under an open content license such as Creative Commons.

Takedown policy

Please contact us and provide details if you believe this document breaches copyrights.
We will remove access to the work immediately and investigate your claim.

SCALE UP OF SURFACTANT ALTERNATING GAS FOAM PROCESSES

SCALE UP OF SURFACTANT ALTERNATING GAS FOAM PROCESSES

Proefschrift

ter verkrijging van de graad van doctor
aan de Technische Universiteit Delft,
op gezag van de Rector Magnificus Prof.dr.ir. T.H.J.J. van der Hagen,
voorzitter van het College voor Promoties,
in het openbaar te verdedigen op woensdag 25 september 2019 om 10:00 uur

door

Rodrigo Orlando SALAZAR CASTILLO

Master of Science in Applied Physics,
Benemérita Universidad Autónoma de Puebla, Puebla, México,
geboren te Puebla, México.

Dit proefschrift is goedgekeurd door de
promotor: Prof. dr. W.R. Rossen

Samenstelling promotiecommissie:

Rector Magnificus, voorzitter
Prof. dr. W.R. Rossen, Technische Universiteit Delft

Onafhankelijke leden:

Prof. dr. M.A Hicks Technische Universiteit Delft
Prof.dr.ir. R.A.W.M. Henkes Technische Universiteit Delft
Dr. D. Voskov Technische Universiteit Delft
Dr. F. Douarche IFP Energies Noevelles
Dr. K. Ma Total E&P Research and Technology USA LLC
Dr. F.H.J. van der Heyden Shell Global Solutions International B.V.

This research was funded by the Joint Industry Project (JIP) on Foam for Enhanced Oil Recovery at Delft University of Technology, and partly by the Mexican Institute of Petroleum (IMP) through the program PCTRES and by the Mexican National Council of Science and Technology (CONACYT) through the program SENER-Hidrocarburos.



Keywords: Foam, Surfactant-Alternating-Gas, Mobility Control, Injectivity, non-Newtonian, Enhanced-Oil-Recovery

Printed by: Gilde Print

Cover Design by: R.O. Salazar Castillo.

Copyright © 2019 by R.O. Salazar Castillo

ISBN 978-94-6384-069-9

An electronic version of this dissertation is available at
<http://repository.tudelft.nl/>.

To Lidia Estefania and Rodrigo Oswaldo

CONTENTS

List of Figures	xi
List of Tables	xix
Summary	xxi
Samenvatting	xxv
Preface	xxx
1 Introduction	1
1.1 Research Objectives and Thesis Outline	9
1.1.1 Chapter 2: Foam Diversion in Heterogeneous Reservoirs: Effect of Permeability and Injection Method	9
1.1.2 Chapter 3: Fractional-Flow Theory for Non-Newtonian Surfactant-Alternating-Gas Foam Processes	9
1.1.3 Chapter 4: Scale-up of Laboratory Data for Surfactant-Alternating-Gas Foam EOR	9
1.1.4 Chapter 5: Coreflood Study of Non-Monotonic Fractional-Flow Behavior with Foam: Implications for Surfactant-Alternating-Gas Foam EOR	10
2 Foam Diversion in Heterogeneous Reservoirs: Effect of Permeability and Injection Method	11
2.1 Introduction	12
2.1.1 Study of Kapetas et al. (2017).	13
2.2 Method of Solution	16
2.2.1 Solution for One Layer: Gas Injection in SAG Flood	16
2.2.2 Solution for One Layer: Foam Injection	19
2.2.3 Diversion Between Layers	21
2.3 Results	22
2.3.1 Gas Injection Without Foam	22
2.3.2 Foam Injection.	23
2.4 SAG Injection	24
2.4.1 Surfactant filling all layers	27
2.4.2 Finite surfactant slugs	27
2.5 Discussion	35
2.6 Summary and Conclusions	40

3	Fractional-Flow Theory for Non-Newtonian Surfactant-Alternating-Gas Foam Processes	42
3.1	Introduction	43
3.1.1	Fractional-Flow Theory	43
3.1.2	Foam in Porous Media	44
3.2	Fractional-Flow Solutions for Gas Injection in Non-Newtonian SAG Processes	48
3.3	Application	55
3.4	Results	56
3.4.1	Shear-Thinning Foam ($n=0.33$)	56
3.4.2	Shear-Thickening Foam ($n=1.34$)	57
3.4.3	Finite-Difference Simulation	60
3.5	Conclusions	62
4	Scale-up of Laboratory Data for Single-Slug Surfactant-Alternating-Gas Foam for Enhanced-Oil-Recovery	64
4.1	Introduction	65
4.2	Experimental Apparatus	68
4.3	Materials	70
4.4	Experimental Procedure	70
4.5	Foam Model	71
4.6	Model-fitting	72
4.7	Results	74
4.8	Discussion and Conclusions	83
5	Coreflood Study of Non-Monotonic Behavior with Foam: Implications for Surfactant-Alternating-Gas Foam EOR	85
5.1	Introduction	86
5.2	Experimental Procedure	88
5.3	Results	89
5.4	Discussion	95
5.5	Conclusions	96
6	Conclusions and Recommendations	98
6.1	Conclusions	98
6.1.1	Chapter 2: "Foam Diversion in Heterogeneous Reservoirs: Effect of Permeability and Injection Method"	98
6.1.2	Chapter 3: "Fractional-Flow Theory for Non-Newtonian Surfactant-Alternating-Gas Foam Processes"	100
6.1.3	Chapter 4: "Scale-up of Laboratory Data for Single-Slug Surfactant-Alternating-Gas Foam EOR"	100
6.1.4	Chapter 5: "Coreflood Study of Non-Monotonic Behavior with Foam: Implications for Surfactant-Alternating-Gas Foam EOR"	101
6.2	Recommendations	102

A	Corey-Brooks Relative-Permeability Model and Foam Model	104
B	Discretization Scheme in our Finite-Difference Simulator	107
C	Dimensionless Pressure as Function of Dimensionless Time	108
D	Steady-State Foam Data	110
E	Description of Computer Programs for non-Newtonian SAG Processes	112
	Bibliography	115
	Acknowledgements	123
	Curriculum Vitæ	125
	List of Publications	126

LIST OF FIGURES

1.1	Energy demand in 2040 by country or region according to the International Energy Agency (2019).	1
1.2	Projected total primary energy demand (TPED) in the world in a sustainable development scenario (SDS), according the world energy outlook (WEO) model.	2
1.3	Projected total primary energy demand (TPED) in the world in the new policies scenario (NPS), according to the world energy outlook (WEO) model.	3
1.4	Schematic fractional-flow curves for gas and water with foam and no foam. For the foam curve, S_w^* corresponds to the nearly vertical portion of the curve, reflecting an abrupt transition in gas mobility. (Rossen and Zhou, 1995).	4
1.5	Fractional-flow analysis of a the injection of the first gas slug following the injection of a surfactant slug during a SAG process. On the left, fractional-flow curve. On the right, the resulting dimensionless time-distance diagram. In this example the range of data fitted to the model include the data relevant to a SAG process (adapted from Boeije and Rossen (2018)).	6
1.6	Portion of a fractional-flow curve with a shock to a weaker foam predicted to occur upon gas injection following the injection of a surfactant slug in a SAG process (Boeije and Rossen, 2018).	7
1.7	On the top, water saturation in a coreflood where foam is injected at the bottom. Slightly after foam (in blue) breaks through the outlet, a secondary desaturation wave (in green) emerges and propagates upstream. The surfactant concentration was 1.0% AOS and the permeability of the Bentheimer sandstone core was 2.5×10^{-12} m ² . The length of the core was 38.1 cm. The core was placed horizontally. On the bottom, pressure difference across 11 intervals of equal length along the core, as a function of number of pore volumes injected (adapted from Simjoo and Zitha (2015)). The secondary desaturation wave corresponds to a marked increase in pressure gradient.	8

2.1	Predicted total superficial velocity of foam in three sandstone formations as function of foam quality f_g at pressure gradient (A) 400 bar/m, (B) 40 bar/m, (C) 4 bar/m; based on model fit to coreflood data (Table 2.2). Corrected from Kapetas et al., 2017.	14
2.2	Schematic of hypothetical four-layer reservoir: Layer 1, Bentheimer, 2 Berea, 3 Sister Berea, 4 Bandera Gray. The heights h_i are adjusted to that the pore volume of each layer is equal. Layers are isolated by shale breaks.	15
2.3	Solution for gas injection into surfactant bank (blue curve, green shock) or water-saturated reservoir (red curve, light-blue shock), with foam properties of the Bentheimer formation.	17
2.4	Characteristics on dimensionless time-distance diagram for gas injection into surfactant bank in the Bentheimer formation. Legend gives total relative mobility λ_{rt} in $(Pas)^{-1}$ for each water saturation corresponding to the characteristics, listed from the shock water saturation of 0.266 (i.e., the steepest characteristic) to $S_{wr} = 0.250$	17
2.5	Construction of displacement for foam injection on fractional-flow curve (in this case, for Bandera Gray, using foam parameters corresponding to 4 bar/m). $J1$ represents injection of a foam with formation of a gas bank ahead of it (drawn in black), and $J2$ injection of a foam with no gas bank ahead (drawn in orange). In this case, with no surfactant adsorption, a diagonal line from the origin to I separates the two cases.	20
2.6	Cumulative layer pore volumes injected t_{Di} as function of total pore volumes injected t_{Dt} for gas injection without foam.	22
2.7	Dimensionless injection pressure P_{Dt} as function of total pore volumes injected t_{Dt} for gas injection without foam.	23
2.8	Dimensionless injection pressure P_{Dt} as function of reservoir pore volumes injected t_{Dt} for foam injection with $f_w = 0.01$ and foam parameters corresponding to 400 bar/m	24
2.9	Layer pore volumes injected t_{Di} as function of total pore volumes injected t_{Dt} for 99 %-quality ($f_w = 0.01$) foam injection with foam parameters corresponding to 400 bar/m.	25
2.10	Layer pore volumes injected t_{Di} as function of total pore volumes injected t_{Dt} for 70%-quality ($f_w = 0.3$) foam injection with foam parameters corresponding to 400 bar/m.	25
2.11	Dimensionless injection pressure P_{Dt} as function of reservoir pore volumes injected t_{Dt} for foam injection with $f_w = 0.01$ and foam parameters corresponding to 40 bar/m	25
2.12	Dimensionless injection pressure P_{Dt} as function of reservoir pore volumes injected t_{Dt} for foam injection with $f_w = 0.01$ and foam parameters corresponding to 4 bar/m	26

2.13	Relative gas injection rate R_i (Eq. 2.6) into the four layers as a function of total pore volumes injected t_{Dt} for gas injection in SAG with surfactant initially saturating all layers; STARS foam model.	27
2.14	Cumulative gas injection into the four layers t_{Di} as a function of total pore volumes injected t_{Dt} for gas injection in SAG with surfactant initially saturating all layers; STARS foam model.	28
2.15	Dimensionless injection pressure P_{Dt} as function of total pore volumes injected t_{Dt} for gas injection in SAG with surfactant initially saturating all layers; STARS foam model.	28
2.16	Cumulative gas injection into the four layers t_{Di} as a function of total pore volumes injected t_{Dt} for gas injection in SAG with surfactant initially saturating all layers; Namdar Zanganeh model.	28
2.17	Fraction of gas injected into the four layers R_i over time for a SAG process with a 10^{-8} PV surfactant slug; STARS foam model.	29
2.18	Fraction of gas injected into the four layers R_i over time for a SAG process with a 10^{-7} PV surfactant slug; STARS foam model.	30
2.19	Fraction of gas injected into the four layers R_i over time for a SAG process with a 10^{-6} PV surfactant slug; STARS foam model.	30
2.20	Cumulative gas injection into the four layers t_{Di} over time for a SAG process with a 10^{-7} PV surfactant slug; STARS foam model.	30
2.21	Dimensionless injection pressure P_{Dt} vs. time for SAG process with various surfactant slug sizes; STARS foam model. Arrow indicates 10^{-7} PV surfactant slug.	31
2.22	Fraction of gas injected into the four layers R_i over time for a SAG process with a 10^{-6} PV surfactant slug; Namdar Zanganeh foam model. . .	31
2.23	Fraction of gas injected into the four layers R_i over time for a SAG process with a 10^{-4} PV surfactant slug; Namdar Zanganeh foam model. . .	32
2.24	Fraction of gas injected into the four layers R_i over time for a SAG process with a 10^{-2} PV surfactant slug; Namdar Zanganeh foam model. . .	32
2.25	Fraction of gas injected into the four layers R_i over time for a SAG process with a 1 PV surfactant slug; Namdar Zanganeh foam model.	32
2.26	Dimensionless injection pressure P_{Dt} vs. time for SAG process with various surfactant slug sizes; Namdar Zanganeh model. Arrow indicates 10^{-4} PV surfactant slug.	33
2.27	Cumulative gas injection into the four layers over time for a SAG process with a 10^{-4} PV surfactant slug; Namdar Zanganeh model.	33
2.28	Cumulative gas injection into the four layers t_{Di} over time for a SAG process with surfactant filling all layers except the Bander Gray layer; STARS foam model.	34
2.29	Cumulative gas injection into the four layers t_{Di} over time for a SAG process with surfactant filling all layers except the Bander Gray layer; Namdar Zanganeh model.	34

2.30	Fraction of gas injected into the four layers R_i over time for a SAG process with finite surfactant slug injected into layers excluding the Bandera Gray layer; STARS foam model. From top to bottom, 10^{-8} , 10^{-6} , 10^{-4} , 10^{-2} and 1 PV surfactant slugs.	36
2.31	Dimensionless injection pressure P_{Dt} vs. time for SAG process with various surfactant slug sizes injected into all layers except the Bandera Gray layer; STARS foam model.	37
2.32	Fraction of gas injected into the four layers R_i over time for a SAG process with finite surfactant slug injected into layers excluding the Bandera Gray layer; Namdar Zanganeh foam model. From top to bottom, 10^{-8} , 10^{-6} , 10^{-4} , 10^{-2} and 1 PV surfactant slugs.	38
3.1	The two steady-state foam regimes. On the left, pressure difference across a 2-ft sandpack as a function of superficial velocities of water (U_w) and gas (U_g). In this case foam is shear-thinning in the high-quality (upper left) regime (Osterloh and Jante, 1992). On the right, pressure gradient as a function of superficial velocities in a coreflood study (Alvarez et al., 2001). This case is shear-thickening.	46
3.2	On the left, a fractional-flow curve adapted from Boeije and Rossen (2018). Black diamonds are coreflood data used to construct the fractional-flow curve. Red dots denote the initial (I) and injection (J) conditions. On the right, an expanded view of the same curve near the point of tangency defining the shock.	47
3.3	A dimensionless time-distance diagram (Rossen and Boeije, 2015). The mobilities of the shock and of a few of the characteristics are included.	47
3.4	Fractional-flow curves for different radii for a shear-thinning foam with a power-law exponent of $n=0.33$. The parameter $fmdry$ varies from 0.356 at the wellbore radius ($r_w=0.1$ m) (blue curve) to 0.312 at $r = 1.0$ m (red), 0.286 at $r = 10$ m (yellow), and 0.271 at the outer radius (r_e)=100 m (purple).	49
3.5	Fractional-flow curves for different radii for a shear-thickening foam ($n=1.34$), where $fmdry$ varies from 0.259 at $r_w=0.1$ m (blue curve) to 0.262 at $r = 1$ m (red), 0.266 at $r = 10$ m (yellow), and 0.271 at the outer radius $r_e = 100$ m (purple).	50
3.6	On the left, an augmented view of the dimensionless position (x_D) vs dimensionless time (t_D) diagram for a shear-thinning foam. The characteristics are straight lines within each increment in x_D . On the right, larger scale plot of the same diagram, showing how the characteristics curve.	51

3.7 Schematic of fractional-flow solution for a shear-thinning foam. The dashed lines represent the shock and the dotted lines represent a characteristic. a) Shock and a characteristic for the first increment in x_D , at the wellbore. b) The shock and the characteristic in the second increment. Note that the shock velocity decreases while the velocity of the characteristic behind it increases with respect to the first increment. c) The collision between the characteristic and the shock results in a new shock and the disappearance of the characteristic that had formerly been the shock. 52

3.8 Dimensionless time-distance diagram illustrating collision of characteristic and shock in a shear-thinning foam; cf. **Figure 3.7**. 52

3.9 Fractional-flow solution for a shear-thickening foam. The dashed line represent the shock and the dotted line represents a new characteristic. a) A shock forms in the first increment. b) As the shock enters the next increment, it imposes a new fractional-flow problem in the second increment with initial condition, I , and with injection condition, A' . c) Solution of the fractional-flow problem in the second increment including an accelerated shock and a new characteristic. 53

3.10 Dimensionless time-distance diagram corresponding to a shear-thickening foam. Dimensionless time-distance diagram corresponding to a shear-thickening foam. 54

3.11 Dimensionless time-distance diagram for the shear-thinning foam with a power-law exponent $n = 0.33$. Note that some characteristics collide with the shock. For illustration purposes we plot only 50 characteristics. 57

3.12 Total relative mobility (λ_{rt}) as a function of dimensionless position (x_D) at a fixed dimensionless time ($t_D = 0.5$) for a non-Newtonian foam with power-law exponent n equal to 0.33. 58

3.13 Water saturation behind the shock plotted as a function of $fmdry$, as both change with radial position, for shear-thinning foam with power-law exponent n equal to 0.33. The blue curve shows the water saturation behind the shock for the shear-thinning foam and the green curve shows the saturation for the shock calculated with the tangency condition for a fractional-flow curve at the same dimensionless position. . . 58

3.14 Total relative mobility behind the shock (blue curve) as a function of dimensionless position for a shear-thinning foam with power-law exponent n equal to 0.33. The green curve shows total relative mobility for the corresponding positions calculated from the tangency condition. 59

3.15 Dimensionless pressure rise (P_D) as a function of dimensionless time (t_D) for a shear-thinning foam with power law exponent n equal to 0.33. 59

3.16 Dimensionless time-distance diagram for a shear-thickening foam with a power-law exponent (n) of 1.34. For illustration purposes we plot only 50 characteristics. 60

3.17	Total relative mobility at shock as function of dimensionless position for a shear-thickening foam with power-law exponent $n = 1.34$	61
3.18	Total dimensionless pressure (P_D) as a function of dimensionless time (t_D) for the Newtonian foams that apply at the wellbore radius (on the left, $fmdry = 0.259$) and at the outer radius (on the right, $fmdry = 0.271$).	61
3.19	Effect of grid-block resolution on calculated injectivity using finite-difference simulation. In blue, the dimensionless pressure evolution calculated using 100 grid blocks, for a foam with power-law exponent $n = 1.34$. In green, using 500 grid blocks, for the same foam parameters; in red fractional-flow calculation.	62
4.1	On the left, a fractional-flow curve adapted from Boeije and Rossen (2018). The red dots denote the initial (I) and injection (J) conditions for injection of the first gas slug. On the right, the dimensionless time-distance diagram for the corresponding gas-injection process. The mobilities of the shock, solid line, and four of the characteristics, represented as dotted lines, are included.	66
4.2	Shock construction for the injection of the first gas slug in a SAG for a multivalued fractional-flow curve (Boeije and Rossen, 2018)	68
4.3	Experimental apparatus A , with controlled temperature. Apparatus B is substantially similar, with changes noted in the text.	69
4.4	Fractional-flow function $f_w(S_w)$ for a foam scan performed at a total superficial velocity of 4.21 ft/day (1.48×10^{-5} m/s) with $C_S = 0.5$ wt.%. In the blue curves, S_w was measured directly using a CT scanner. In the red curves, S_w is inferred using the $k_{rw}(S_w)$ function presented by Eftekhari and Farajzadeh (2017). In the green curves, S_w is inferred using the $k_{rw}(S_w)$ function reported by Kapetas et al. (2017) with no foam present.	73
4.5	Experimental data for the five foam scans performed in this study. The black dots denote the experimental data for the foam scan performed with $u_t = 2.94 \times 10^{-6}$ m/s and $C_S = 0.037$ wt.%; the red dots data for $u_t = 7.35 \times 10^{-6}$ m/s and $C_S = 0.037$ wt.%; the pink dots data with $u_t = 1.47 \times 10^{-5}$ m/s and $C_S = 0.1$ wt.%; the blue dots data with $u_t = 1.47 \times 10^{-5}$ m/s and $C_S = 0.5$ wt.%; the yellow dots with $u_t = 7.35 \times 10^{-6}$ m/s and $C_S = 1.0$ wt.% AOS. The dashed lines denote the model fit to the whole foam scan in each case.	75

4.6 Experimental data around the point of tangency corresponding to the foam scans presented in **Figure 4.5**. On the left, $f_w(S_w)$ curves predicted by the model fit performed using the whole foam scan. On the right, $f_w(S_w)$ curves obtained using the method of Rossen and Boeije (2015) for a SAG (middle estimate; see sensitivity analysis below). The solid lines correspond to the predicted shocks during a gas-injection process. 77

4.7 Four model fits for the data of Experiment 5. We performed two model fits using the method of Rossen and Boeije (2015) for a SAG; one without the NZ correction (here label as R&B STARS) and one with the NZ correction (here labelled R&B NZ). We performed the other two model fits using the method of Eftekhari and Farajzadeh (2017) to the entire foam scan; with and without the NZ correction, here labelled EFS STARS and EFS NZ, respectively. On the bottom, we present an expanded view near the tangency point. 80

4.8 Model fits from the sensitivity test of the method of Rossen and Boeije (2015) using different criterion. See description in the text. 81

4.9 Two fits using different $k_{rw}(S_w)$ functions for the data of Experiment 4 using the method of Rossen and Boeije (2015). We summarize the resulting foam parameters in **Table 4.4**. 82

5.1 Construction of displacement by the first gas slug in a SAG process on fractional-flow curve: monotonic $f_w(S_w)$ function. Modified from Boeije and Rossen (2018) 87

5.2 Non-monotonic $f_w(S_w)$ function and construction of displacement by the first gas slug in a SAG process. From Boeije and Rossen (2018) 88

5.3 Sectional differential pressures in bars in foam coreflood as function of pore volumes injected. Since all sections have the same length, these values are directly proportional to pressure gradient in each section. On the left, before foam breakthrough. On the right, steady-state pressure difference long after foam breakthrough. The nominal foam quality and total superficial velocity and the surfactant concentration of this experiment are 95%, 4.25 ft/day and 0.5 wt%, respectively. 90

5.4 Sectional differential pressures in bars as function of pore volumes injected. The nominal foam quality and total superficial velocity and the surfactant concentration of this experiment are 98%, 4.25 ft/day and 0.5 wt%, respectively. Breakthrough has no effect on the mobility of foam upstream of the core. 91

5.5	Fractional-flow function $f_w(S_w)$ for a foam scan performed at a total superficial velocity of 4.25 ft/day (1.48×10^{-5} m/s) with $C_S = 0.5$ wt%. The blue curves show S_w as measured directly using a CT scanner. The red curves show S_w as inferred using the $k_{rw}(S_w)$ function reported by Eftekhari and Farajzadeh (2017). The green curves show S_w as inferred using the $k_{rw}(S_w)$ function reported by Kapetas et al. (2017) based on data with no foam present.	91
5.6	Average cross-section water-saturation S_w along the core during displacements at two foam qualities. The direction of the flow is from left to right. The decline in S_w with time at 96% foam quality shows a slow upstream propagation of stronger foam.	93
5.7	Sectional differential pressures in bars as function of time in two core-flood experiments with identical injection conditions but different initial conditions. The nominal foam quality and total superficial velocity and the surfactant concentration of this experiment are 95%, 4.25 ft/day and 0.5 wt%, respectively. On the left, steady state is achieved after 8 hours when the experiment is started from a ‘wet’ initial condition, $f_w = 0.9$. In contrast, steady state is achieved only after 55 hours when starting from a ‘dry’ initial condition, $f_w = 0.01$, right.	94
5.8	Fractional flow as function of water saturation for one non-monotonic set of data. u_t and C_S are equal to 1.5×10^{-5} m/s and 0.5 wt% AOS, respectively. We plot the shock as a dashed line according to the solution method of Rossen and Bruining (2007). f_{wt} denotes the fractional flow at which S_w starts to increase with decreasing f_w , which is between 0.05 and 0.02 in this experiment.	94
C.1	Injectivity for different fits for the data of Experiment 4. We use the foam scan data corresponding to Experiment 4. The corresponding foam parameters and mobilities behind the shock are listed in Table 4.1 , Table 4.3 and Table 4.4	108
D.1	Experimental data of Experiment 1 at fixed foam quality of 80%.	111
D.2	Experimental data for Experiment 4 at a fixed foam quality of 95%. A stronger foam erupts at the core outlet (Section 6) at about 1.2 PV. Before this, the pressure gradient is nearly uniform along the core, as expected at local equilibrium in the high-quality regime Alvarez et al. (2001).	111
E.1	Flow diagram corresponding to the algorithm for the fractional-flow solution.	113
E.2	Flow diagram corresponding to the finite-difference simulator.	114

LIST OF TABLES

2.1	Corey Relative-Permeability Parameters for Four Formations from Kapetas et al. (2017).	15
2.2	Foam Parameters Fit to Coreflood Data for Four Formations from Kapetas et al. (2017).	16
2.3	Dimensionless injection pressure P_{Dt} at one reservoir pore volume injected for foam injection at various foam qualities and foam parameters corresponding to various pressure gradients.	24
2.4	Properties of Foam Predicted for Gas Injection in SAG in Each Layer for Parameters Fit to STARS Foam Model. Total relative mobilities λ_{rt} are given in $(Pas)^{-1}$	26
2.5	Properties of Foam Predicted for Gas Injection in SAG in Each Layer for Parameters Used in Namdar Zanganeh Model. Total relative mobilities λ_{rt} are given in $(Pas)^{-1}$	26
2.6	Properties of Foam Predicted for Gas Injection in SAG in Each Layer for Parameters Used in Namdar Zanganeh Model. Total relative mobilities λ_{rt} are given in $(Pas)^{-1}$	40
3.1	Summary of the input parameters used in this study Kapetas et al. (2017).	55
4.1	Foam parameters obtained by the least-squares routine used by Eftekhari and Farajzadeh (2017) and by Kapetas et al. (2017) . We include the predicted total relative mobility, λ_{rt} , behind the shock front in $[Pa\ s]^{-1}$ and the maximum dimensionless pressure, P_D , reached during gas injection	78
4.2	Foam parameters resulting from yhe method of Rossen and Boeije (2015) for SAG . We include the predicted total relative mobility, λ_{rt} , behind the shock front in $[Pa\ s]^{-1}$ and the maximum dimensionless pressure, P_D , reached during gas injection	79
4.3	Foam parameters resulting from the sensitivity test performed on Ex- perimen 4 for the method of Rossen and Boeije (2015) for SAG . We in- clude the predicted total relative mobility, λ_{rt} , behind the shock front in $[Pa\ s]^{-1}$ and the maximum dimensionless pressure, P_D , reached dur- ing gas injection	82
4.4	Foam parameters fit using the method of Rossen and Boeije (2015). We use two different $k_{rw}(S_w)$ functions. We include the maximum dimen- sionless pressure, $MaxP_D$, and the total relative mobility, λ_{rt} , behind the shock front during gas injection in $[Pa\ s]^{-1}$	83

5.1	Summary of Experimental Findings, f_{wt} denotes the fractional flow at which S_w starts to increase with decreasing f_w	95
A.1	Corey-Brooks parameters used in Chapter 4	105

SUMMARY

Foam increases sweep efficiency during gas injection in enhanced oil recovery (EOR) processes by reducing gas mobility. In fact, foam is the only EOR technology that is able to fight against both gravity segregation and geological heterogeneity. Surfactant Alternating Gas, or SAG, is the preferred method to place foam into the reservoir for both operational and injectivity reasons. For example, this method of injection avoids the difficulties of having foam in the injection lines. Injecting foam in this manner also offers better injectivity than in foam-injection processes in which pre-generated foam is injected into the reservoir.

Foam can divert flow from higher- to lower-permeability layers and thereby improve vertical conformance in gas-injection enhanced oil recovery processes. Permeability affects both the mobility reduction of wet foam in the "low-quality" foam regime and the limiting capillary pressure at which foam collapses in the high-quality regime (Kapetas et al., 2017). In **Chapter 2** we upscale a SAG process to a hypothetical field application using the foam properties measured by Kapetas et al. (2017) in cores from four sandstone formations ranging in permeability from 6 to 1900 md with approximately the same porosity. We consider a hypothetical reservoir containing four non-communicating layers with the properties of the formations in their study. These properties are modeled using the parameters corresponding to their fit to their own data. We examine the effects of the injection method on diversion in a dynamic foam process using fractional-flow modeling.

We find that the effectiveness of diversion varies greatly with the injection method. In a SAG process, diversion of the first slug of gas depends on foam behavior at very high foam quality. Mobility in the foam bank during gas injection depends on the nature of a shock front that bypasses most foam qualities usually studied in the laboratory. The foam with the lowest mobility at fixed foam quality does not necessarily give the lowest mobility in a SAG process. In particular, diversion in SAG depends whether and how foam collapses at low water saturation; this property varies greatly among the foams reported by Kapetas et al. (2017). Moreover, diversion depends on the size of the surfactant slug received by each layer before gas injection. This, of course, favors diversion away from high-permeability layers that receive a large surfactant slug, but there is an optimum surfactant slug size: too little surfactant and the diversion from high-permeability layers is not effective; too much surfactant and the mobility is reduced in low-permeability layers, too. For a SAG process, it is very important to determine if the foam collapses completely at irreducible water satu-

ration. In addition, we show the diversion expected in foam-injection processes as a function of foam quality. The faster propagation of surfactant and foam in the higher-permeability layers aids the diversion, as expected. This depends on the foam quality and on non-Newtonian foam mobility and varies with time during the injection process. Injectivity is extremely poor with the injection of preformed foam, but in some effective SAG foam processes, it is not necessarily worse than injectivity in a water-flood.

Laboratory data indicate that foam can be non-Newtonian at low water fractional flow f_w , and therefore during gas injection in a SAG process. We investigate in **Chapter 3** the implications of this finding for mobility control and injectivity by extending fractional-flow theory to gas injection in a non-Newtonian SAG process in radial flow. Non-Newtonian behavior at low f_w implies that the limiting water saturation for foam stability varies as the superficial velocity decreases with radial distance from the well. We discretize the flow domain radially and perform a Buckley-Leverett analysis on each small increment in radius. As the characteristics solution move outward, they do not carry a fixed water saturation S_w but maintain a constant f_w . We show the implications of non-Newtonian behavior for mobility control at the displacement front as well as for the injectivity. We base the foam-model parameters and the extent of non-Newtonian behavior on laboratory data in the absence of oil. We compare these results to values of the mobility and injectivity determined by conventional finite-difference simulation, where the grid resolution is usually limited.

We find that, for shear-thinning foam, mobility control improves as the foam front propagates from the well, but the injectivity declines somewhat with time. The change of mobility ratio at the front can be considerable, given the huge velocity difference between the wellbore and further into the reservoir. This change is not simply that measured at steady state at fixed water fractional flow in the laboratory, however, because the shock front in a non-Newtonian SAG process does not propagate at fixed f_w (though individual characteristics do). Moreover, the shock front is not governed by the conventional condition of tangency of the shock to the fractional-flow curve, though it continuously approaches this condition. The injectivity benefits from the increased mobility of the shear-thinning foam near the well. The foam front, which maintains a constant dimensionless velocity for Newtonian foam, decelerates somewhat with time for the shear-thinning foam. For shear-thickening foam, mobility control deteriorates as the foam front advances, though the injectivity improves somewhat with time. Overall, however, the injectivity suffers from the reduced foam mobility at high superficial velocity near the well. The shock front for a shear-thinning foam accelerates somewhat with time. Overall, mobility and injectivity are complex results of changing saturation and varying superficial velocities with distance from the well. Conventional simulators cannot adequately represent these effects or estimate injectivity accurately in the absence of an extraordinarily fine grid

resolution near the injection well.

Dynamic SAG corefloods are unreliable for direct scale-up to the field because of core-scale artifacts. In **Chapter 4** we scale-up local-equilibrium (LE) data measured at very low f_w measured in a Bentheimer core for different surfactant concentrations and total superficial velocities. We fit LE data to an Implicit-Texture foam model for scale-up to a dynamic foam process on the field scale using fractional-flow theory. We apply two different parameter-fitting methods. The first method (Eftekhari and Farajzadeh, 2017; Kapetas et al., 2017) relies on a least-squares fit to the entire foam-quality scan. The second method (Rossen and Boeije, 2015) relies on visual inspection and therefore on the criterion used in performing the fit. We compare the resulting fits to our data and their predictions for scale-up. We also test the implications of complete foam collapse at irreducible water saturation S_{wr} for injectivity.

Each set of data predicts a shock front with sufficient mobility control at the leading edge of the foam bank. Mobility control improves with increasing surfactant concentration. For each case, scaled-up injectivity is much better than with co-injection of gas and liquid. The results illustrate also how the foam model, without the constraint of foam collapse at irreducible water saturation (Namdar Zanganeh et al., 2014), can greatly underestimate the injectivity of strong foams. For the first time, we examine how the method of fitting the parameters to coreflood data affects the resulting scale-up to field behavior. Since the method of Rossen and Boeije (2015) relies on the criteria used in performing the fit, it does not give a unique parameter fit. However, the predicted mobility at the foam front using different criteria is the same within the experimental uncertainty. The predicted injectivity, however, does vary somewhat among the parameter fits. Gas injection in a SAG process depends especially on the behavior at low injected water fraction and whether foam collapses at the irreducible water saturation, which may not be apparent from a conventional scan of foam mobility as a function of the gas fraction in the injected foam. In two of the five cases examined this method of fitting the whole scan gives a poor fit for the shock in gas injection in SAG. We have also tested the sensitivity of the scale-up to the $k_{rw}(S_w)$ function assumed in the fit to data. For the two functions tested here, the predicted injectivity is practically the same, whereas the mobility at the shock front is very different.

About half the published laboratory studies of foam fractional-flow curves report non-monotonic behavior, where at some point the water saturation S_w increases with decreasing liquid fractional flow f_w . Rossen and Bruining (2007) warn that such behavior would result in foam collapse during the injection of the first gas slug in a SAG process at the field scale. In **Chapter 5** we report and analyze a series of steady-state and dynamic coreflood experiments to investigate the occurrence of non-monotonic fractional-flow behavior. These corefloods differ in surfactant con-

centration, injected gas fraction (foam quality) and total superficial velocity and are supported by CT measurements of S_w . The CT data confirm that, in these cases, as foam weakens with decreasing f_w , liquid saturation S_w increases, confirming the non-monotonic $f_w(S_w)$ behavior.

In our results, every case of non-monotonic fractional-flow behavior begins with the propagation of foam from the inlet, followed by an eruption of a much-stronger foam at the outlet of the core and backwards propagation of the stronger foam state to the inlet, similar to behavior reported by Apyadin and Kavscek (2001) and Simjoo and Zitha (2015). This suggests that there may be more than one stable local-equilibrium (LE) foam state. The initial creation of the stronger foam near the outlet is at least in part due to the capillary end effect. It is thus not clear which LE foam state controls the behavior in a SAG process in the field. In our experiments, the subsequent transition from a stronger- to a weaker-foam state, leading to the non-monotonic $f_w(S_w)$ behavior, coincides with conditions for weaker foam (lower surfactant concentration, lower f_w) and less-vigorous foam generation (lower superficial velocity); this agrees with the theory of foam propagation of Ashoori et al. (2012). It is at least plausible that the coreflood data relevant to a SAG process in the field are those that are unaffected by the capillary end effect. In our study, we could obtain data excluding this effect either at low surfactant concentration or by using data from pre-generated foam, propagating at apparent local equilibrium before foam breakthrough at the core outlet.

SAMENVATTING

Schuim verbetert de ‘sweep’ efficiency van gas injectie om meer olie uit een reservoir te verkrijgen (Engels: Enhanced Oil Recovery (EOR)) door het verlagen van de gas mobiliteit. Schuimstroming is de enige EOR methode die zwaartekracht effecten en geologische heterogeniteit effecten overwint. Het afwisselend injecteren van een zeepoplossing en gas (Engels: Surfactant Alternating Gas (SAG)) is de voorkeursmethode om schuim in een reservoir te injecteren vanwege operationele en injectie redenen. Omdat bij deze methode schuim geproduceerd wordt in het reservoir, heeft deze methode niet de moeilijkheden die optreden bij de aanwezigheid van schuim in de injectieleidingen. Bovendien heeft het injecteren van schuim op deze manier een betere injectiviteit dan schuim-injectie methoden waarbij voorgegenereerde schuim wordt geïnjecteerd in het reservoir.

Schuim in een reservoir kan de stroming van vloeistoffen omleiden van hogere naar lagere permeabiliteit gesteentelagen en daarmee de verticale conformiteit verbeteren bij gas EOR methoden. Permeabiliteit beïnvloedt de mobiliteit reductie van nat schuim in het zogenaamde lage kwaliteit schuimregime en de limiterende capillaire druk waarbij het schuim uiteenvalt in het hoge kwaliteit schuimregime (Kapetas e.a., 2017). In **Hoofdstuk 2** schalen wij een SAG proces op naar hypothetische veldomstandigheden waarbij wij de schuimeigenschappen gebruiken die waren gemeten door Kapetas e.a. (2017) in kernen van vier verschillende zandsteen formaties die variëren in permeabiliteit van 6 tot 1900 mD met ongeveer dezelfde porositeit. Wij beschouwen een hypothetisch reservoir dat vier niet-communicerende lagen bevat met de eigenschappen van de formaties uit hun studie. Deze eigenschappen zijn gemodelleerd met de parameters die overeenkomen met de fits van hun data. Wij bestuderen de effecten van de injectiemethode op de omleiding van de stroming van vloeistoffen in een dynamisch schuimstroming proces, waarbij wij gebruikmaken van fractionele-stroming modelering.

Wij vinden dat de effectiviteit van de omleiding in grote mate varieert met de injectiemethode. In een SAG proces hangt de omleiding van het eerst geïnjecteerde volume aan gas af van het stromingsgedrag van het schuim in het in de hoge kwaliteit schuimregime. Mobiliteit in de schuimlaag tijdens gasinjectie hangt af van de aard van de schuimstromingsschok die de meeste schuimkwaliteit regimes overbrugt, hetgeen bestudeerd kan worden in een laboratorium. Schuimstroming met de laagste mobiliteit bij een bepaalde schuimkwaliteit is niet persé hetzelfde als schuim dat de laagste mobiliteit geeft in een SAG proces. In het bijzonder, hangt de omleiding van

SAG af van hoe en of schuim uiteenvalt bij een lage watersaturatie; deze eigenschap varieert in grote mate bij de schuimen gerapporteerd door Kapetas e.a. (2017). Bovendien, hangt de omleiding van de grootte van het geïnjecteerde volume aan zeepoplossing dat door elke formatie stroomt voorafgaand aan de gasinjectie. Dit leidt natuurlijk tot een voorkeur voor omleiding van de hoge permeabiliteit lagen waar een groot volume zeepoplossing instroomt, maar er is een optimale grootte voor het geïnjecteerde volume van de zeepoplossing volume: bij te weinig geïnjecteerde zeepoplossing is de omleiding van de hoge permeabiliteit lagen niet effectief; bij te veel zeepoplossing wordt de mobiliteit ook verlaagd in de lage permeabiliteit lagen. Voor een SAG proces is het belangrijk om te bepalen of een schuim volledig uiteenvalt bij de kritische water saturatie. Bovendien tonen wij aan dat de omleiding in een schuimstroming proces een functie is van de schuimkwaliteit. Zoals verwacht draagt de snelle voortbeweging van zeepoplossing en schuim in de hogere-permeabiliteit lagen bij aan de omleiding, zoals verwacht. Dit hangt af van de schuimkwaliteit en de niet-Newtonse schuimmobiliteit en dit varieert met de injectietijd. De injectiviteit is heel laag bij de injectie van voorgegenereerde schuim, maar in sommige effectieve SAG processen is die niet noodzakelijk lager dan bij waterinjectie.

Laboratorium data geven aan dat schuimeen niet-Newtons gedrag kan vertonen bij lage water fractionele-stroming f_w , dus tijdens de gasinjectie van een SAG proces. Wij onderzoeken in **Hoofdstuk 3** de implicaties van onze bevindingen voor de mobiliteit controle en injectiviteit door fractionele-stroming theorie uit te bouwen naar gasinjectie in een niet-Newtons SAG proces met radiale stroming.

Niet-Newtons gedrag bij lage f_w impliceert dat de limiterende watersaturatie voor de schuimstabiliteit varieert als de superficiële stromingssnelheid omlaag gaat met de radiële afstand van de injectieput. Wij discretiseren het stromingsdomein in de radiële richting en voeren een Buckley-Leverett analyse uit voor een zeer kleine toename van de radius. Als de karakteristieke oplossingen naar buiten bewegen heeft het schuim niet een vaste watersaturatie S_w maar blijft f_w wel constant. Wij tonen aan dat er implicaties zijn van het niet-Newtons gedrag op zowel de mobiliteitscontrole bij het verplaatsingsfront als op de injectiviteit. Wij baseren de modelparameters van de schuimstroming en de mate van niet-Newtons gedrag op laboratorium data, in de afwezigheid van olie. Wij vergelijken onze resultaten met de mobiliteit en de injectiviteit zoals bepaald met een conventionele eindige differentiemethode simulatie, waar de grid resolutie vaak gelimiteerd is.

Wij vinden dat voor afschuifverdundend schuim de mobiliteitscontrole verbetert naarmate het schuimfront voortbeweegt vanaf de injectieput, maar de injectiviteit omlaag gaat met de tijd. Het verschil in de mobiliteitsratio van het front kan significant zijn, gegeven dat er een groot snelheidsverschil is in de schuimstroming in de injectieput en verder in het reservoir. Dit verschil is niet gemakkelijk te meten in een sta-

biele toestand bij een gecontroleerde water fractionele-stroming in een laboratorium omdat het schokfront in een niet-Newtons SAG proces niet propageert bij een vaste fractionele stroming (maar individuele karakteristieken doen dat wel). Bovendien wordt het schokfront niet bepaald door de conventionele voorwaarde dat de schok een raakpunt heeft op de fractionele stromingscurve, maar het komt wel steeds in de buurt van deze conditie. Injectiviteit heeft baat bij de verhoogde mobiliteit van afschuifverdundend schuim bij de injectieput. Het schuimfront, dat een constant dimensieloze snelheid voor Newtons schuim heeft, vertraagt met tijd voor afschuifverdundend schuim. Voor afschuifverdikkend schuim wordt mobiliteit controle slechter met de voortbeweging van het schuimfront, maar de injectiviteit wordt wel beter met de tijd. Het schuimfront voor een afschuifverdundend schuim versnelt met de tijd. Uiteindelijk zijn mobiliteit en injectiviteit het complexe resultaat van veranderende saturatie en variërende superficiële stromingssnelheden als functie van de afstand tot de injectieput. Conventionele simulatiemodellen deze niet op een adequate manier representeren en de injectiviteit nauwkeurig voorspellen in wanneer niet een ontzettend fijn rekenrooster wordt gebruikt bij de injectieput.

Dynamische SAG kernstromingen zijn onbetrouwbaar om direct mee op te schalen naar veldomstandigheden vanwege kern gerelateerde artefacten. In **Hoofdstuk 4** schalen wij lokaal evenwicht (Engels: local-equilibrium (LE)) data op voor heel lage waarden van f_w , zoals gemeten in een Bentheimer kern met verschillende concentraties van de surfactant en van de totale superficiële stromingssnelheid. Wij fitten LE data met een Implicit-Texture schuimmodel en schalen dit op tot een dynamisch schuim bij veldomstandigheden, waarbij wij gebruikmaken van de fractionele stromingstheorie. Wij passen twee verschillende parameter fitting methodes toe. De eerste methode (Eftekhari en Farajzadeh, 2017; Kapetas e.a., 2017) maakt gebruik van een kleinste kwadratenmethode voor de gehele schuimkwaliteitsscan. De tweede methode (Rossen en Boeije, 2015) maakt gebruik van een visuele inspectie en hangt daarom af van het criterium dat gebruikt wordt voor de fit. Wij vergelijken de gefitte meetdata met hun voorspellingen bij het opschalen. Wij testen ook de implicaties voor het algehele uiteenvallen van het schuim bij de kritische watersaturatie, S_{wr} , voor injectiviteit.

Elke dataset voorspelt een schokfront met een toereikende mobiliteitscontrole bij de voorrand van de schuimlaag. De mobiliteitscontrole verbetert met toenemende surfactant concentratie. Voor al de opgeschaalde gevallen is de injectiviteit beter met co-injectie van gas en zeepoplossing. De resultaten illustreren ook hoe het schuimmodel, zonder de beperking dat schuim uiteenvalt bij de S_{wr} (Namdar Zanganeh e.a., 2014), er toe kan leiden dat de injectiviteit wordt onderschat bij een schuim. Voor het eerst hebben wij onderzocht hoe de methode van fitten van de parameters aan kernstromingsdata invloed heeft op het opgeschaalde stromingsgedrag bij veldomstandigheden. Aangezien de methode van Rossen en Boeije (2015) afhangt van

het criterium dat gebruikt wordt bij het uitvoeren van de fit, resulteert het niet in een unieke parameter fit. Echter, de voorspelde mobiliteit van het schuimfront, waarbij verschillende criteria in acht worden genomen, is hetzelfde binnen de experimentele onzekerheid. De voorspelde injectiviteit varieert wel met de parameter fits, maar gasinjectie in een SAG proces hangt vooral af van het gedrag bij lage f_w en of het schuim uiteenvalt bij de kritische watersaturatie, hetgeen onduidelijk kan zijn bij de conventionele kwaliteitsscan van de schuimmobiliteit als een functie van de gasfractie in het geïnjecteerde schuim. In twee van de vijf gevallen die wij onderzochten geeft deze methode om de gehele scan te fitten een slechte fit voor de schok bij de gasinjectie in SAG. Wij onderzochten ook de gevoeligheid van het opgeschaalde model voor de $k_{rw}(S_w)$ functie waarbij wij uitgingen van de data fit. Voor de twee functies die wij hier hebben getest, is de voorspelde injectiviteit praktisch hetzelfde, terwijl de mobiliteit bij het schokfront zeer verschilt.

Ongeveer de helft de gepubliceerde laboratoriumstudies voor fractionele stromingscurves van schuim rapporteert niet-monotonisch gedrag, waarbij bij een zeker punt de water saturatie, S_w , hoger wordt met dalende f_w . Rossen en Bruining (2007) waarschuwen dat dit soort schuimstromingsgedrag kan resulteren in het uiteenvallen van het schuim tijdens het injecteren van het eerste volume aan gas in een SAG proces bij veldomstandigheden. In **Hoofdstuk 5** analyseren wij een reeks van statische en dynamische kernstroming experimenten om de aanwezigheid van niet-monotonisch fractioneel stromingsgedrag te onderzoeken. Wij variëren daarbij de surfactant concentratie, de geïnjecteerde gasfractie (schuimkwaliteit) en de totale superficiële stromingssnelheid en maken gebruik van S_w data bepaald aan de hand van CT metingen. De CT data tonen dat in deze gevallen het schuim afzwakt met dalende f_w en de S_w stijgt, waarmee het niet-monotonisch $f_w(S_w)$ gedrag wordt bevestigd.

In onze experimenten begint elk geval van niet-monotonisch $f_w(S_w)$ gedrag met het voortbewegen van schuim vanaf de ingang van de kern en dit wordt gevolgd door een uitbarsting van een sterker schuim bij de uitgang van de kern. Het sterke schuim beweegt zich voort naar de ingang van de kern, wat vergelijkbaar is met het gedrag dat is gerapporteerd door Apaydin en Kavscek (2001) en Simjoo en Zitha (2015). Dit suggereert dat het mogelijk is dat er meer dan één stabiele lokaal-evenwicht schuimtoestand is. De initiële creatie van een sterker schuim bij de uitgang van de kern is ten minste gedeeltelijk te verklaren met het capillair eindeffect. Het is daarom niet duidelijk welke LE schuimtoestand zal plaatsvinden bij een SAG proces voor veldomstandigheden. In onze experimenten leidt, de opvolgende transitie van een sterkere naar een zwakkere schuimtoestand tot een niet-monotonisch $f_w(S_w)$ gedrag, wat overeenkomt met het gedrag voor een zwak schuim (lagere surfactant concentratie, lagere f_w) en met een minder heftige schuimgeneratie (lagere superficiële stromingssnelheid); dit komt overeen met de theorie van schuimvoortbeweging van Ashoori e.a. (2012). Het is mogelijk dat de data voor de kernstroming relevant zijn voor

een SAG proces bij veldomstandigheden waarbij een capillair eindeffect geen invloed heeft. In ons onderzoek hebben wij data verkregen in afwezigheid van dit effect bij lage surfactant concentratie of door gebruik te maken van data van een voorgege-
neerd schuim, waarbij het schuim zich voortbeweegt bij een schijnbaar lokaal even-
wicht, althans tot het moment dat het schuim doorbreekt tot de uitgang van de kern.

PREFACE

This thesis compiles our efforts on the study of Surfactant Alternating Gas foam for Enhanced Oil Recovery processes. In particular, we were interested in upscaling laboratory data to field applications. Saying that the journey was difficult is not enough to express the amount of effort that I and all the people involved in this collection of papers have invested in achieving the goals summarized here.

I started my Ph.D. at TU Delft after completing my M.Sc. in Applied Physics back in Mexico. I decided that I wanted to learn about the oil industry and I was honoured to have received a scholarship from the Mexican Institute of Petroleum to pursue that goal. Prof. William Rossen kindly agreed to guide me through this path. He did so even when the project was not giving the expected progress, and he always maintained the high standards of his group. This thesis would have not been possible without his supervision.

Through this journey I learned the basics of foam, and this thesis could be a good starting point for engineers or scientist interested in the physics of foam for EOR.

Finally, the reader must be aware that this thesis is based on four papers produced during my stay at TU Delft. One of these papers is already published and the others are either under review or intended for submission to scientific journals. I have made an effort to be consistent in notation and citation, and I apologize in advance for any errors I may have made during the transcription.

Rodrigo Orlando Salazar Castillo
Delft, September 2019

1

INTRODUCTION

THE access of billions of people around the world to food, medicine and transportation depends today on energy provided by oil. The demand for reliable energy will continue rising as the world's population and the middle class in the developing economies grow. According to Biorol (2019), by 2040 most of the energy demand will come from China. Also, according to the presented predictions the economies of Africa will demand about 1600 million tonnes of oil equivalent (Mtoe). This demand will be for the first time similar to that of the European Union, as illustrated in Figure 1.1.

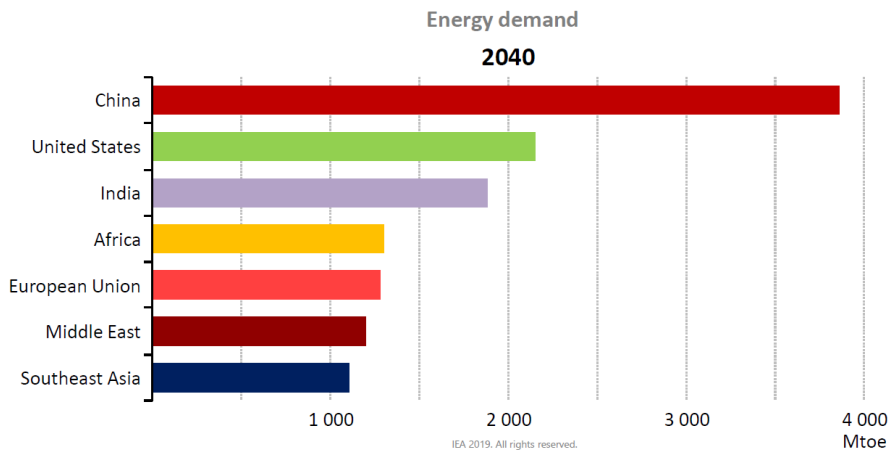


Figure 1.1: Energy demand in 2040 by country or region according to the International Energy Agency (2019).

New technologies to generate renewable energy are being developed and implemented to mitigate the effects of global warming. It is accepted that global warming is produced by the increasing concentration of CO₂ in the atmosphere. Therefore, we expect that political decisions will promote the use of renewable sources of energy. However, according to accepted economic models (Birol et al., 2018), even in a sustainable development scenario (SDS) there will be the need for oil in the foreseeable future. This means that in the less-favourable scenario for oil, humankind would need to replace the reserves of oil approximately at the same rate as they are being consumed over the next two decades, as illustrated in Figure 1.2. In the same report, the Energy Information Administration considers a scenario that is more politically realistic, if less optimistic in terms of global warming (Figure 1.3), with limited new policies that will be implemented around the world. In this scenario (NPS) the demand for oil would actually increase in the coming decades.

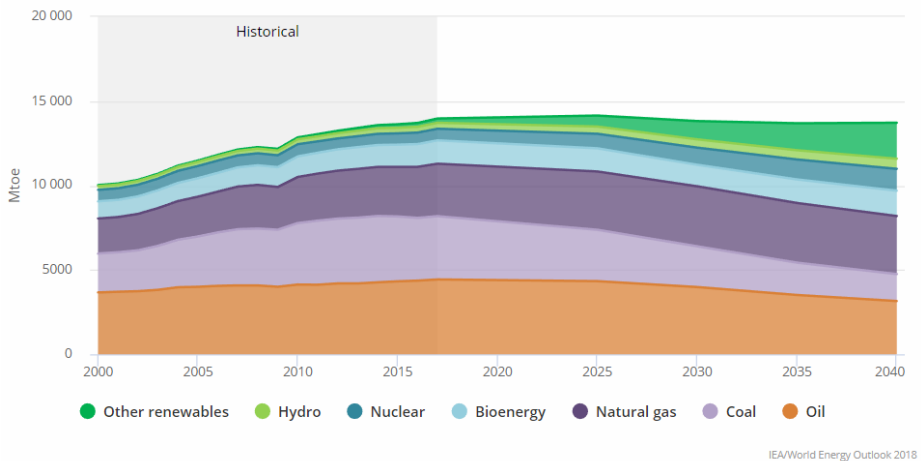


Figure 1.2: Projected total primary energy demand (TPED) in the world in a sustainable development scenario (SDS), according the world energy outlook (WEO) model.

There is a need to increase the oil reserves in already-producing reservoirs. In fact, an average of only 1/3 of the initially residing oil in place can be produced with current technologies (Lake et al., 2014). During “primary production” oil comes out under its own pressure, followed by “secondary production,” where water or gas (e.g., CO₂, N₂) are injected into the reservoir to maintain pressure and displace the oil in place. However, even after prolonged injection of water and gas, nearly 2/3 of the oil initially in place cannot be recovered. This is due to two main factors: first, the natural heterogeneity of the reservoir causes the fluids to bypass the low-permeability zones; and second, even where water contacts oil, it leaves much of it behind because oil is trapped by interfacial forces. In other words, “displacement efficiency” is

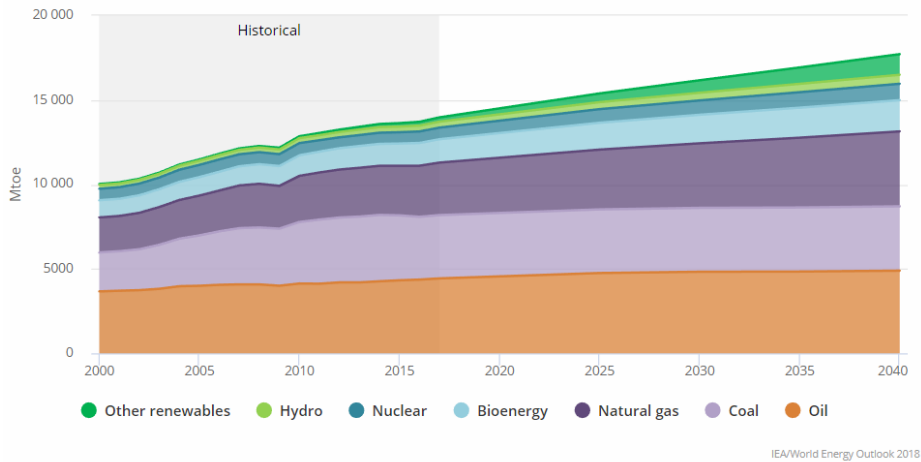


Figure 1.3: Projected total primary energy demand (TPED) in the world in the new policies scenario (NPS), according to the world energy outlook (WEO) model.

incomplete.

Even though gas's displacement efficiency is better than water's (approaching 100% in some cases) geological heterogeneity remains a problem. Furthermore, the large density and viscosity contrasts between gas and oil give rise to new challenges. For instance, the lower density of gas causes it to override to the top of the reservoir and its lower viscosity causes early breakthrough, especially in heterogeneous reservoirs. Foam can be used to solve these problems (Bond and Holbrook, 1958; Rossen, 1996). For instance, foam offers greater resistance to flow in higher-permeability layers (Alvarez et al., 2001) and therefore reduces the effects of geological heterogeneity. Even more, it can mitigate gravity override if it is injected as alternating slugs of surfactant solution and gas (Shan and Rossen, 2004).

Foam is made of gas bubbles separated by liquid films. The films are stabilized by surfactant solution. In porous media, foam is continuously generated in the formation. It can segregate during flow and it collapses if it dries out to a limiting water saturation, S_w^* . Therefore, the capillary pressure P_c affects foam texture in several ways. In other words, as one increases gas saturation, and by implication reduces water saturation, in a porous medium, P_c rises until it reaches a limiting capillary pressure, P_c^* , where the films start to break and the foam texture becomes coarser. The stability and texture of foam depends, then, on this limiting capillary pressure, which varies with the type of surfactant, its concentration, the salinity and other factors like the temperature and the porous medium. The limiting capillary pressure

also depends on gas velocity.

At local equilibrium it is possible to distinguish two foam-flow regimes at different foam qualities (Alvarez et al., 2001; Osterloh and Jante, 1992). The quality of a foam is defined as its gas fractional flow, f_g . In the high-quality (dry) regime, pressure gradient is independent of the gas superficial velocity; the low-quality regime, pressure gradient is independent of the surfactant-solution superficial velocity. In the high-quality regime bubble size is controlled by the limiting capillary pressure, whereas in the low-quality regime the bubble size is fixed. The rheology of foam in the low-quality regime is consistently shear-thinning, whereas in the high-quality regime it can be Newtonian, shear-thinning, or shear-thickening.

Assuming that the presence of foam alters only gas mobility and not the capillary-pressure function $P_c(S_w)$, it is possible to state that the limiting capillary pressure corresponds to a specific water saturation, S_w^* . This last result is important because it allows one to identify S_w^* from the fractional-flow curve (Figure 1.4). The nearly vertical part of the curve, where gas mobility changes abruptly near a single water saturation, occurs at S_w^* .

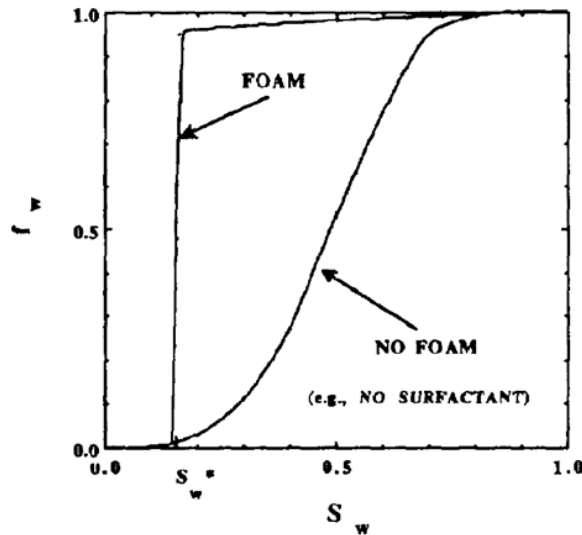


Figure 1.4: Schematic fractional-flow curves for gas and water with foam and no foam. For the foam curve, S_w^* corresponds to the nearly vertical portion of the curve, reflecting an abrupt transition in gas mobility. (Rossen and Zhou, 1995).

The mobility of the foamed gas is very great at very high qualities, whereas at larger water fractional flows it is very low. This variation in mobility is key when se-

lecting the best method to place foam in the reservoir. In this thesis we discuss two methods to place foam into the reservoir: the first is co-injection of surfactant solution and gas at a fixed foam quality, and the second is SAG (Surfactant-Alternating-Gas) injection, in which alternating injection of slugs of surfactant solution and gas takes place. This last method relies on foam generation in the reservoir. SAG is preferred over co-injection because it offers greater injectivity. Also, it offers greater sweep efficiency because it reduces gravity override (Shan and Rossen, 2004). The main objective of this thesis is to study the injection of the first gas slug during a SAG, just after the injection of the first surfactant slug. In particular, we are focus in up-scaling laboratory data to the field scale.

There are other two methods to place foam into the reservoir that are worthy to be mentioned but will not be discussed further in the remainder of this thesis. The first is the dissolution of surfactant into the injected gas, usually CO₂ (Le et al., 2008; Xing et al., 2012). Using this technique one aims to form foam in the formation as the dissolved surfactant meets the water in place. The second method is another co-injection method, in which surfactant solution and gas are injected into the reservoir from different well intervals (Rossen et al., 2010; Stone, 2004). In this method, gas is usually injected from the deeper interval and foam is created in the reservoir where gas and surfactant solution meet.

The injection of the first gas slug following a slug of surfactant solution can be modelled using fractional-flow theory. Fractional-flow theory is able to estimate injectivity and mobility control for the injection of the first gas slug during a SAG process as long as enough experimental data near the point of tangency are available (Boeije and Rossen, 2018). On the left of Figure 1.5, the initial condition (100% surfactant saturation) and the injection condition (residual water saturation) for the gas-injection process are represented by the letters I and J , respectively. Both boundary conditions lie on the same fractional-flow curve. The path connecting I and J does not have monotonically increasing slopes; therefore a portion of the trajectory has to be replaced by a discontinuity, or shock. In a SAG process a shock, connecting I to the point of tangency, is always present. The data suggests that a spreading wave forms behind the shock. The spreading wave is made of characteristics that travel with fixed saturation. On the right of Figure 1.5, we present a typical dimensionless time-distance diagram corresponding to the injection of the first gas slug. From the diagram, we can immediately identify the mobility control achieved during gas injection when using the given formulation. The mobility behind the shock is equal to that at the leading edge of the foam front in the diagram. Also, one can calculate the injectivity by integrating the mobilities of the shock and the characteristics depicted in the diagram. At a fixed dimensionless time, along the spreading wave, the mobility of each characteristic continuously increases as one approaches the injection well. This is beneficial to injectivity. If foam does collapse at irreducible water

saturation S_{wr} the injectivity increases significantly (Namdar Zanganeh et al., 2014).

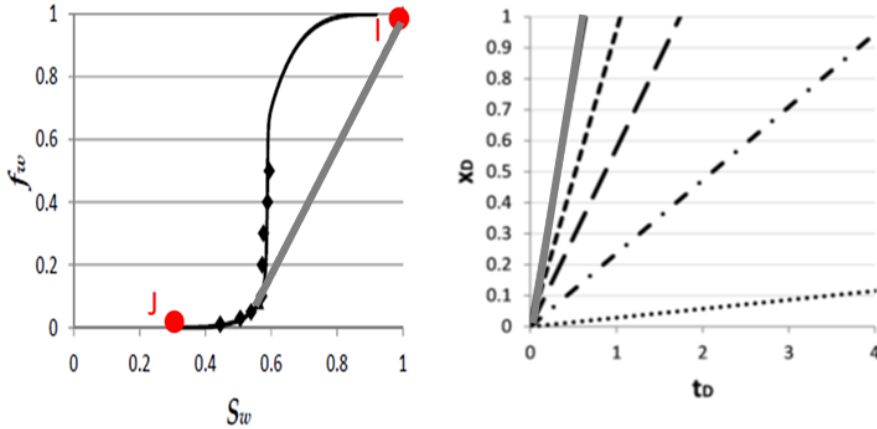


Figure 1.5: Fractional-flow analysis of the injection of the first gas slug following the injection of a surfactant slug during a SAG process. On the left, fractional-flow curve. On the right, the resulting dimensionless time-distance diagram. In this example the range of data fitted to the model include the data relevant to a SAG process (adapted from Boeije and Rossen (2018)).

As can be observed from Figure 1.5, collecting data at the driest (high f_g) conditions is critical in order to correctly model a SAG process for a given surfactant formulation in a given porous medium. Unfortunately, data in this region is not easy to obtain and there are very few such studies published. One might think that in such a case one could rely on the pressure-gradient data recorded during a dynamic SAG coreflood, where gas is injected into a surfactant-saturated core. However, at the field scale it is assumed that local equilibrium (LE) applies; that is, the processes of creation and destruction of foam films are at equilibrium at each location. Therefore a coreflood experiment could be misleading when it is performed at laboratory dimensions (hours and centimetres) if the main goal is to predict the behaviour in the field. In other words, laboratory-scale corefloods can be distorted by lack of LE and also by the capillary end-effect and dispersion. That is why, in one part of our study, we focus on fitting steady-state data to LE foam models. To do so, we use the parameters of the STARS foam model (Cheng et al., 2000), as did Kapetas et al. (2017) and Boeije and Rossen (2015a).

Another complication in laboratory foam corefloods is the capillary end effect at the core outlet, where foam generation occurs because of a higher water saturation there (Ransohoff and Radke, 1988). Experimental studies (Apaydin and Kovscek,

2001; Nguyen et al., 2003; Simjoo and Zitha, 2015) have reported a secondary desaturation wave that propagates upstream into the core slightly after foam breakthrough, as illustrated in Figure 1.7. Apaydin and Kovscek (2001) observed this behaviour at relatively high surfactant concentrations. They claim it is initiated by the capillary end-effect, and upstream propagation of the foam front reflects greater gas trapping just upstream of the foam. However, the mechanism for this increased trapping is not specified. Moreover, estimation of gas trapping in coreflood experiments (Nguyen et al., 2009) is difficult. Thus, there is still no complete explanation for the upstream propagation of this stronger foam state. Nevertheless, it is clear that the eruption of a much stronger foam depends on behaviour near the core outlet. Therefore, its relevance to a foam process in a homogenous reservoir at the field scale is dubious, and its relevance to heterogeneous reservoirs is unclear.

Kibodeaux and Rossen (1997) found that S_w does not decrease monotonically as f_w decreases, such a case is illustrated in Figure 1.6. In fact, about half of the published fractional-flow curve for foam SAG are non-monotonic in this sense. Experimental and theoretical studies suggest that the fractional-flow function for foam can, then, be either multivalued or comprise more than one fractional-flow curve representing two or even more foam states. The dynamics between curves could include jumps governed by limiting conditions. If that is the case, the fractional-flow analysis of Rossen and Bruining (2007) suggests that the corresponding SAG process would not be successful at the field scale. The shock is to a weakened or collapsed foam at a very low f_w , as illustrated in Figure 1.6. However, the mechanisms behind a non-monotonic fractional-flow curve have not been explored.

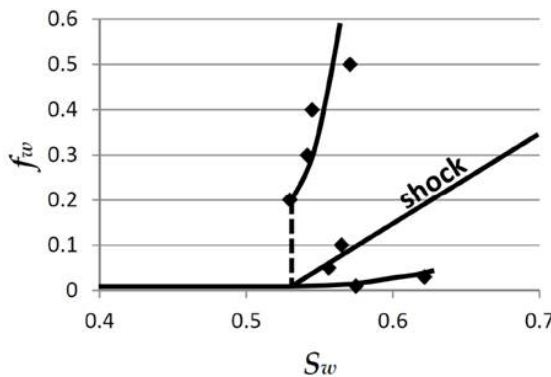


Figure 1.6: Portion of a fractional-flow curve with a shock to a weaker foam predicted to occur upon gas injection following the injection of a surfactant slug in a SAG process (Boeije and Rossen, 2018).

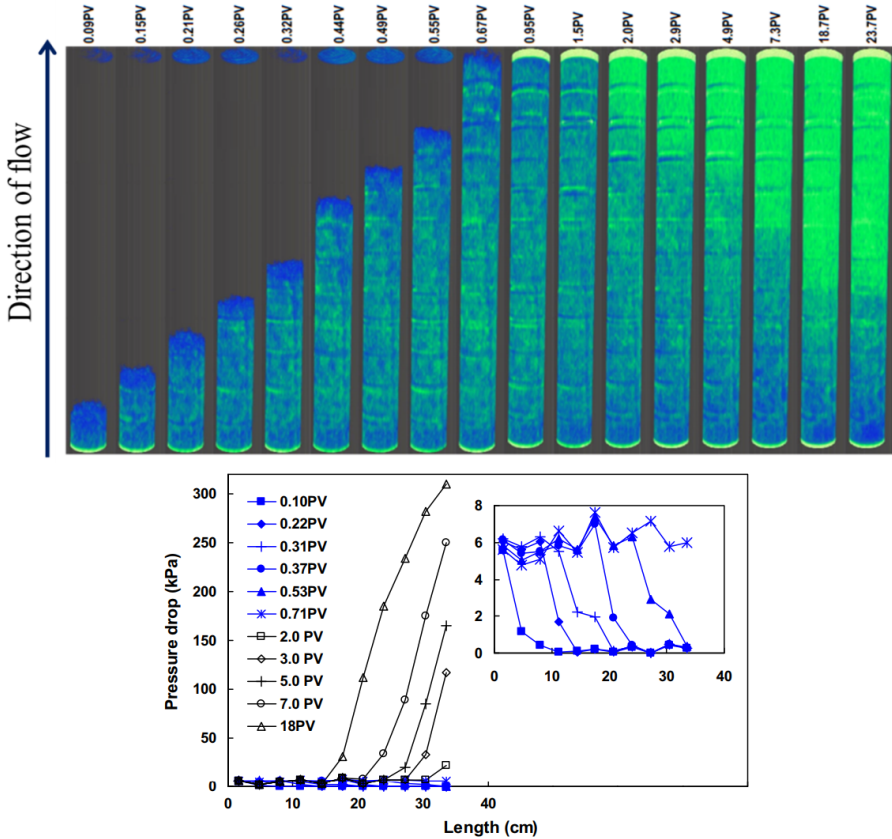


Figure 1.7: On the top, water saturation in a coreflood where foam is injected at the bottom. Slightly after foam (in blue) breaks through the outlet, a secondary desaturation wave (in green) emerges and propagates upstream. The surfactant concentration was 1.0% AOS and the permeability of the Bentheimer sandstone core was $2.5 \times 10^{-12} \text{ m}^2$. The length of the core was 38.1 cm. The core was placed horizontally. On the bottom, pressure difference across 11 intervals of equal length along the core, as a function of number of pore volumes injected (adapted from Simjoo and Zitha (2015)). The secondary desaturation wave corresponds to a marked increase in pressure gradient.

1.1. RESEARCH OBJECTIVES AND THESIS OUTLINE

1.1.1. CHAPTER 2: FOAM DIVERSION IN HETEROGENEOUS RESERVOIRS: EFFECT OF PERMEABILITY AND INJECTION METHOD

When injecting foam into a heterogeneous reservoir one is mainly interested in achieving diversion of foam from the high-permeability layers into the low-permeability layers and at the same time obtaining a good injectivity. In **Chapter 2**, using fractional-flow theory, we aim to help answering the question: which method for placing foam (co-injection or a SAG) into a heterogeneous reservoir is better (in terms of injectivity and diversion)? To that end, we implement the method of characteristics to a set of foam displacements in a hypothetical four-layered reservoir. To feed our model we use the foam parameters measured by Kapetas et al. (2017) for four sandstones with different permeability but similar pore volume. The results of our calculation can also be found in Al Ayesh et al. (2017).

1.1.2. CHAPTER 3: FRACTIONAL-FLOW THEORY FOR NON-NEWTONIAN SURFACTANT-ALTERNATING-GAS FOAM PROCESSES

Foam rheology in the high-quality regime can be either Newtonian (**Chapter 4**), shear-thinning (Osterloh and Jante, 1992) or shear thickening (Alvarez et al., 2001). In **Chapter 3** we explore how a non-Newtonian rheology (either shear-thinning or shear-thickening in the high-quality regime) would impact a SAG if this behavior were maintained at the field scale. In particular, we study the impacts of non-Newtonian foam on injectivity and mobility control during the injection of the first gas slug following the injection of a surfactant slug during a SAG. To that end, we develop, and implement in *Matlab*, a methodology using fractional-flow theory to map and track the effects of a given non-Newtonian rheology on the shock and the characteristics. This chapter is mainly based on the theses of three bachelor students (Bos, 2017; Ponnens, 2017; Ter Haar, 2018).

1.1.3. CHAPTER 4: SCALE-UP OF LABORATORY DATA FOR SURFACTANT-ALTERNATING-GAS FOAM EOR

In this chapter, we focus in measuring local- equilibrium data in a Bentheimer sandstone core and upscaling the results to the field scale. In our experiments, we vary surfactant concentration and the total superficial velocity. We study the impact of velocity and surfactant concentration on the field-scale behavior (mobility control and injectivity). We also perform a sensitivity analysis of the role of the fitting method and the criteria different individuals might use in fitting the data using visual inspection on the calculated mobility control and injectivity at the field scale. Finally, we test the impact of the Namdar Zanganeh et al. (2014) correction, which forces complete foam collapse at irreducible water saturation, S_{wr} , on the obtained foam parameters

and more importantly on the field- scale behavior.

1.1.4. CHAPTER 5: COREFLOOD STUDY OF NON-MONOTONIC FRACTIONAL-FLOW BEHAVIOR WITH FOAM: IMPLICATIONS FOR SURFACTANT-ALTERNATING-GAS FOAM EOR

In this chapter we explore the connection between the occurrence of non-monotonic fractional-flow curves and the capillary end effect for high surfactant concentrations. To that end, we perform a series of foam scans at different surfactant concentrations and different total superficial velocities in a Bentheimer core. In one of the foam scans we measured water saturation using a CT scanner to confirm the non-monotonic trend. Finally, we conduct a transient experiment to explore the role of the capillary end- effect on foam generation in the transition from a 'strong' foam to a 'stronger' foam. The results of this work leads to two possible implications of the occurrence of non-monotonic fractional-flow curves. The first one is that the capillary end effect at high surfactant concentrations and high total superficial velocities introduces an experimental artifact that must be avoided in order to obtain local equilibrium mobility data for homogenous porous media. The second one is that foam in porous media exhibits two stable local- equilibrium states. The implications on a SAG of this second possibility require further study.

2

FOAM DIVERSION IN HETEROGENEOUS RESERVOIRS: EFFECT OF PERMEABILITY AND INJECTION METHOD

Foam can divert flow from higher- to lower-permeability layers and thereby improve vertical conformance in gas-injection enhanced oil recovery. Recently, Kapetas et al. (2017) measured foam properties in cores from four sandstone formations ranging in permeability from 6 to 1900 md, and presented parameter values for foam model fit to those data. Permeability affects both the mobility reduction of wet foam in the "low-quality" foam regime and the limiting capillary pressure at which foam collapses. Kapetas et al. showed how foam would divert injection between layers of these formations if all layers were full of foam injected at a given quality (gas fractional flow). Here we examine the effects of injection method on diversion in a dynamic foam process using fractional-flow modeling and the model parameters derived by Kapetas et al. (2017). Like them, we consider a hypothetical reservoir containing non-communicating layers with the properties of the four formations in their study.

The effectiveness of diversion varies greatly with injection method. In a SAG (surfactant-alternating-gas) process, diversion of the first slug of gas depends on foam behavior at very high foam quality. Mobility in the foam bank during gas injection depends on the nature of a shock front that bypasses most foam qualities usually studied in the laboratory. The foam with the lowest mobility at fixed foam quality does not necessarily give the lowest mobility in a SAG process. In particular, diversion in SAG depends on

how and whether foam collapses at low water saturation; this property varies greatly among the foams reported by Kapetas et al. (2017). Moreover, diversion depends on the size of the surfactant slug received by each layer before gas injection. This of course favors diversion away from high-permeability layers that receive a large surfactant slug, but there is an optimum surfactant slug size: too little surfactant and diversion from high-permeability layers is not effective; too much and mobility is reduced in low-permeability layers, too. For a SAG process, it is very important to determine if foam collapses completely at irreducible water saturation.

In addition, we show the diversion expected in a foam-injection process as a function of foam quality. The faster propagation of surfactant and foam in the higher-permeability layers aids in diversion, as expected. This depends on foam quality and non-Newtonian foam mobility and varies with time of injection. Injectivity is extremely poor with foam injection, but in some effective SAG foam processes it is not necessarily worse than injectivity in a waterflood.

2.1. INTRODUCTION

Gas injection can have excellent displacement efficiency in enhanced oil recovery (EOR), but suffers from poor sweep efficiency because of reservoir heterogeneity, gravity override, and viscous instability (Lake et al., 2014). Foam can overcome these problems and thereby improve sweep efficiency in gas-injection EOR (Rossen, 1996; Schramm, 1994).

In the absence of oil, foam exists in two flow regimes, depending on foam quality (gas fractional flow) and other factors (Alvarez et al., 2001; Osterloh and Jante, 1992). In the "low-quality regime," bubble size is thought to be relatively unchanging, and gas mobility is controlled by viscous drag on bubbles and bubble trapping and mobilization. Foam is strongly shear-thinning in this regime; that is, apparent viscosity decreases with increasing superficial velocity. In the "high-quality regime," foam exists near the limit of stability of the thin films, or lamellae, that separate bubbles (Ettinger and Radke, 1992; Khatib et al., 1988; Rossen and Zhou, 1995). As a result, water saturation is nearly constant in this regime (Persoff et al., 1991). Apparent viscosity can be shear-thinning (apparent viscosity increasing with decreasing superficial velocity), shear-thickening, or Newtonian in this regime (Alvarez et al., 2001).

There are two approaches to modeling foam for EOR. Population-balance (PB) models (Falls et al., 1988; Friedmann et al., 1991; Kam et al., 2007; Kovscek and Radke, 1994; Kovscek et al., 2010) attempt to represent the mechanisms of creation and destruction of lamellae, along with the mechanisms of gas mobility as a function of bubble size and other factors. Implicit-texture (IT) models (Cheng et al., 2000; Fisher et al., 1990; Islam and Farouq-Ali, 1990; Kular et al., 1989; Law et al., 1992; Lotfolahi et al., 2016; Mohammadi and Coombe, 1992; Patzek and Myhill, 1989) represent

the effect of foam on gas mobility through a factor that reduces gas mobility according to water and oil saturations, surfactant concentration, superficial velocities, and other factors. All IT models assume local equilibrium between the various processes creating and destroying lamellae. Current application of PB models (Ashoori et al., 2011a,b; Kam et al., 2007; Kavscek et al., 2010; Rossen et al., 1999) also predict rapid attainment of LE even on the laboratory scale, which suggests that this assumption is sufficiently accurate for field-scale application of foam. There are situations that can be represented only by PB models: the rapid changes in foam properties very near the injection face and at shock fronts, situations where foam generation is in doubt, and cases like fractured reservoirs where foam may not achieve local equilibrium. IT models fit steady-state mobility data for foam in the two flow regimes, such as those of Kapetas et al., as well as PB models (Lotfollahi et al., 2016). We employ an IT foam model, the STARS foam model (CMG, 2015) in this study. Relevant details of the STARS foam model can be found in Appendix A.

2.1.1. STUDY OF KAPETAS ET AL. (2017)

Kapetas et al. (2017) conducted room-temperature steady-state foam corefloods without oil in cores from four sandstone formations: Bentheimer, Berea, Sister Berea, and Bandera Gray. These formations differ greatly in permeability (see Figure 2.2 below). Like many laboratory studies, this study found large pressure gradients with foam, too large for practical field application (Norris et al., 2014; Skauge et al., 2002). Kapetas et al. (2017) also measured the relative-permeability curves for gas and water for cores from the same formations. Table 2.1 gives the relative-permeability parameters of the cores. In foam corefloods, Kapetas et al. (2017) measured pressure gradient, or, equivalently, apparent foam viscosity, in a scan of foam quality (injected gas volume fraction f_g) at a fixed total superficial velocity. From this plot they derived foam parameters for the STARS foam model (Chen and Mohanty, 2014; CMG, 2015; see also Appendix A), which would allow one to predict foam mobility at other superficial velocities and foam qualities in the same formation under the same conditions. The foam parameters they fit to these data are listed in Table 2.2. Though limited in scope (e.g., absence of oil, at room temperature) this study represents one of the most complete studies available of foam behavior for a single foam formulation in formations of different permeability. In particular, it correlates the behavior of foam in both the low-quality and high-quality foam regimes and estimates the effect of non-Newtonian behavior in the low-quality regime. A separate study by Moradi-Araghi et al. (1997) (see also Farajzadeh et al. (2015)) shows that foams exhibit higher resistance factor in higher permeability zones as well as shear-thinning behavior.

Kapetas et al. (2017) found that foam was stronger (had lower relative mobility) in the higher-permeability formations. They also found strongly shear-thinning behavior (represented by a large, positive value of $epcap$) in some of the formations, especially in the Sister Berea formation. They illustrated their findings for diversion in plots of superficial velocities predicted for three of the formations at three pres-

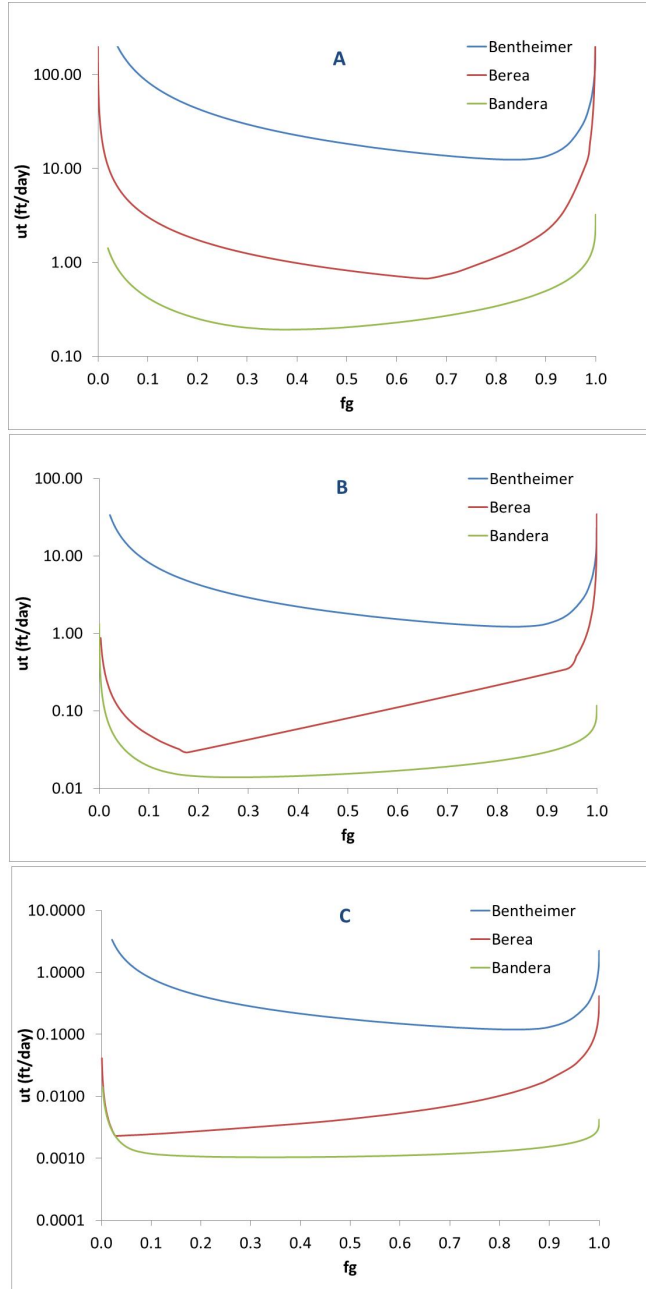


Figure 2.1: Predicted total superficial velocity of foam in three sandstone formations as function of foam quality f_g at pressure gradient (A) 400 bar/m, (B) 40 bar/m, (C) 4 bar/m; based on model fit to coreflood data (Table 2.2). Corrected from Kapetas et al., 2017.

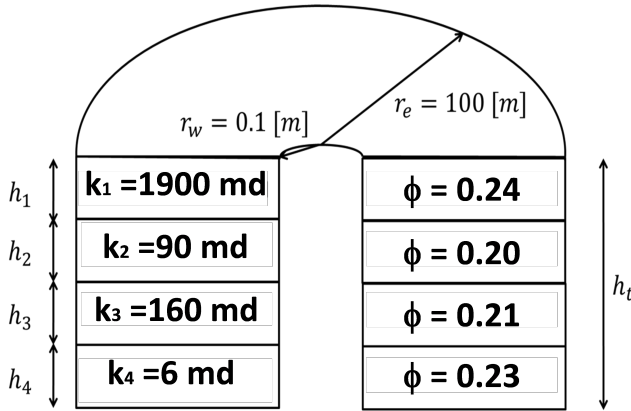


Figure 2.2: Schematic of hypothetical four-layer reservoir: Layer 1, Bentheimer, 2 Berea, 3 Sister Berea, 4 Bandera Gray. The heights h_i are adjusted to that the pore volume of each layer is equal. Layers are isolated by shale breaks.

Layer	k_{rw0}	n_w	k_{rg0}	n_g	S_{wr}	S_{gr}
1. Bentheimer	0.39	2.86	0.59	0.70	0.25	0.20
2. Berea	0.39	4.09	0.99	1.97	0.23	0.12
3. Sister Berea	0.14	5.25	0.47	1.22	0.25	0.25
4. Bandera Gray	1.00	3.56	0.73	2.43	0.46	0

Table 2.1: Corey Relative-Permeability Parameters for Four Formations from Kapetas et al. (2017).

sure gradients. An error was subsequently found in the plots in the paper; the corrected version is reproduced here in **Figure 2.1** (Kapetas et al. (2017) excluded the Sister Berea formation from this plot because its behavior was so non-Newtonian, and therefore very sensitive to pressure gradient.) This calculation assumes that foam completely fills all three formations, and that pressure gradient is the same in each. As they noted, foam causes partial diversion away from the highest-permeability Bentheimer formation. For instance, at a foam quality of 90% and a pressure gradient of 4 bar/m, the ratio of superficial velocities in Bentheimer and Berea or Bandera Gray sandstones, respectively, are 7 and 86, while the permeability ratios are 21 and 317. The extent of diversion varies strongly with foam quality and also with pressure gradient. Diversion is not as great at lower foam quality and larger pressure gradient.

In this study we extend the analysis of **Figure 2.1** to both foam injection (where foam advances in all layers with time) and gas injection in a surfactant-alternating-gas (SAG) flood. We include the Sister Berea layer, to illustrate the effect that strongly shear-thinning foam rheology can have on diversion.

Layer	$fmmob$	$epdry$	$fmdry$	$epcap$	$fmcap$
1. Bentheimer	47700	400	0.271	0.01	9.35×10^{-6}
2. Berea	869000	19600	0.336	0.923	9.87×10^{-6}
3. Sister Berea	30700	8890	0.396	4.39	9.97×10^{-5}
4. Bandera Gray	68200	152	0.549	0.442	1.57×10^{-6}

Table 2.2: Foam Parameters Fit to Coreflood Data for Four Formations from Kapetas et al. (2017).

2.2. METHOD OF SOLUTION

We assume a cylindrical region with an open outer boundary of radius $r_e = 100$ m, with an injection well of radius $r_w = 10$ cm (Figure 2.2). The four formations, each assumed to be uniform in properties, are isolated by shale breaks. We ignore possible gravity segregation in each layer and focus on vertical conformance at the injection well. Each of the four formations has an equal pore volume; because of modest differences in porosity between layers, this makes them slightly different in thickness; see Al Ayesh (2016) for details. This reservoir has a Lorentz coefficient of 0.67 and a Dykstra-Parsons coefficient of 0.87 (cf. Lake et al. (2014)).

The method of solution proceeds first by determining the positions and mobilities of banks in each individual layer as a function of volume of gas or foam injected into that layer. Then these solutions are combined to determine injection rates into the various layers, positions of the banks in each layer, and overall injectivity over time. The effect of oil on foam is complex (Farajzadeh et al., 2012). For simplicity we assume here that oil saturation is zero within the region of interest, in part because we have no data on the effect of oil on foam for our surfactant formulation in the formations examined here.

2.2.1. SOLUTION FOR ONE LAYER: GAS INJECTION IN SAG FLOOD

The fractional-flow solutions for foam injection and gas injection in a SAG process are described elsewhere (Lake et al. (2014), Shan and Rossen (2004), and Zhou and Rossen (1994)). Briefly, one constructs the fractional-flow curve for gas-water flow with and without surfactant (i.e., with or without foam). In a displacement, each water saturation S_w between the initial saturation I and the injected saturation J moves with a dimensionless velocity equal to the slope of the fractional-flow function (df_w/dS_w) at that value of S_w . Dimensionless time t_D is pore volumes of fluid injected into the layer. Dimensionless position x_D is defined as

$$x_D = \frac{r^2 - r_w^2}{r_e^2 - r_w^2} \tag{2.1}$$

where r is radial position.

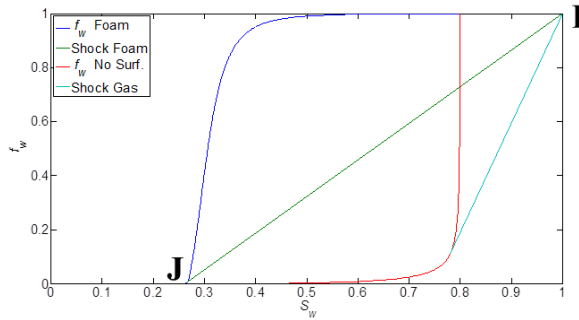


Figure 2.3: Solution for gas injection into surfactant bank (blue curve, green shock) or water-saturated reservoir (red curve, light-blue shock), with foam properties of the Bentheimer formation.

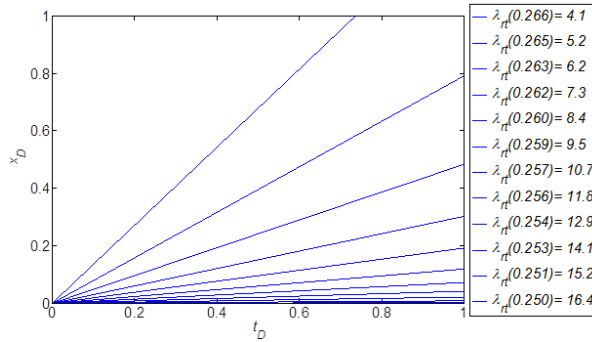


Figure 2.4: Characteristics on dimensionless time-distance diagram for gas injection into surfactant bank in the Bentheimer formation. Legend gives total relative mobility λ_{rt} in $(Pas)^{-1}$ for each water saturation corresponding to the characteristics, listed from the shock water saturation of 0.266 (i.e., the steepest characteristic) to $S_{wr} = 0.250$.

If (df_w/dS_w) is not monotonically increasing from J to I on the fractional-flow curve, there is a discontinuous jump in S_w , i.e. a shock. This shock travels with dimensionless velocity $(\Delta f_w/\Delta S_w)$, where Δ indicates the differences in f_w or S_w across the jump. For our cases, there is a shock at the leading edge of the displacement, from a point of tangency to the fractional-flow curve to the initial condition I at $S_w = 1$; see **Figure 2.3**. Each characteristic, corresponding to a fixed value of S_w and fixed total relative mobility λ_{rt} , travels from the injection point with a fixed velocity (**Figure 2.4**).

For gas injection with no prior surfactant injection, this construction suffices until some values of S_w have passed beyond r_e ; at that point they are excluded from the

displacement. For gas injection in a SAG process, this construction suffices until gas breaks through the furthest extent of surfactant penetration into the given layer; we call this position r_f .

One can estimate r_f from the volume of the previous surfactant slug, v_s , as follows. The volume of surfactant solution injected is equal to the volume of surfactant solution in the foam bank at the moment of gas breakthrough. In the STARS model, during gas injection in a SAG process, almost the entire foam bank is at a water saturation close to $fmdry$ (cf. **Figures 2.3** and **2.4**), the water saturation around which foam collapses; most of the change in slope (df_w/dS_w) occurs near this saturation and therefore most of the characteristics have water saturation close to this. Therefore the radius of the foam bank at the moment of gas breakthrough is approximately given by

$$\pi(r_f^2 - r_w^2) \cdot h \cdot \phi \cdot fmdry \approx v_s \quad (2.2)$$

where h is formation thickness and ϕ the porosity. We have neglected adsorption here for simplicity; we have no data on adsorption for these formations. Adsorption would represent a second fate of injected surfactant, also proportional to pore volume, and reduce the estimate of r_f^2 by a separate factor for each layer. Water saturation within the foam bank would decline very slowly with time as the characteristics advance (**Figure 2.4**), which would lead to a slight increase in r_f over time. For simplicity we neglect that change here.

After gas breaks through the edge of the surfactant bank, a gas flood without surfactant is initiated beyond this region. Water fractional flow beyond the foam bank is nearly zero, and the radius of the foam region remains unchanged. Thus this gas breakthrough represents a gas flood beyond the foam bank. The analysis is identical to that for a gas flood without surfactant described above, except that dimensionless radius is rescaled to the region beyond the foam bank

$$x_D = \frac{r^2 - r_f^2}{r_e^2 - r_f^2} \quad (2.3)$$

and dimensionless time is reset so that time zero is the moment gas breaks through the edge of the surfactant bank. More details are in Al Ayesh (2016).

We derive pressure difference between the injection well and the outer radius r_e as follows. At each dimensionless time we monitor the positions of 200 values of S_w (i.e., 200 characteristics) between I and the value of S_w at the shock for the foam bank and/or gas bank, depending on the process. We integrate for pressure difference between the positions of each consecutive pair of S_w values from Darcy's law and sum up the pressure difference between the injection well and the shock at the

leading edge of the gas bank. If there is a water bank remaining ahead of the gas, its total relative mobility λ_{rt} is uniform at $(1/\mu_w)$, where μ_w is the viscosity of water. If the process modeled is gas injection in a SAG displacement, we carry out the integration first for gas within the foam bank and then for gas ahead of the foam bank after gas breakthrough has occurred. Then we add the pressure difference for all the banks. Finally, to non-dimensionalize the result, we divide by the pressure difference for injecting water at the same volumetric injection rate into the same formation fully saturated with water (for which, as noted, λ_{rt} is uniform at $(1/\mu_w)$). More details are in Al Ayesh (2016). This result is P_D , the dimensionless pressure rise at the injection well for a given pore volume of gas injected. Similarly, $(1/P_D)$ is the dimensionless injectivity into the formation, normalized by the injectivity of water into the same formation fully saturated with water.

The procedure described applies to a process with Newtonian mobilities, unaffected by superficial velocity or pressure gradient. During gas injection in a SAG process the shock (Figure 2.2) is to a very low value of water fractional flow in the high-quality regime. While non-Newtonian behavior is sometimes reported in the high-quality regime (Alvarez et al., 2001; Osterloh and Jante, 1992), the version of the STARS model used here and in the study of Kapetas et al. (2017) does not represent it. Therefore, in this study we use the STARS parameters $fmmob$, $fmdry$, and $epdry$ in Table 2.1 without modification for shear-thinning rheology (i.e., without the factor F_5 described in Appendix A).

2.2.2. SOLUTION FOR ONE LAYER: FOAM INJECTION

In this case there are up to three banks with uniform water saturation and mobility, illustrated in Figure 2.5: the foam bank at the injected foam quality, a gas bank ahead of it, and a water bank representing the initial state of the reservoir. As illustrated in Figure 2.5, for low values of injected water fraction (high foam quality), the propagation of foam is limited by surfactant, and there is a gas bank GB ahead of the foam. (Close examination of Figure 2.5 shows that there is a narrow spreading wave before the shock from GB to I . This spreading wave has high mobility and makes little difference to overall injectivity, so we neglect it, drawing the shock directly from GB to I .) For low foam qualities (high injected water fractional flow) the propagation of foam is limited by gas. There is a surfactant bank SB ahead of the foam with the same mobility as the water bank ahead of it. The water and gas banks each disappear when their trailing shocks reach the outer radius r_e .

Again, in the absence of data for surfactant adsorption for the given surfactant and sandstones, we exclude adsorption from our analysis. Adsorption slows the propagation of surfactant more for higher foam qualities (because there is less surfactant solution per volume of injected foam), which would alter the comparison of diversion over time as a function of foam quality given below. Propagation of foam would be much slower at very high foam quality (low f_w) (Zhou and Rossen (1994)).

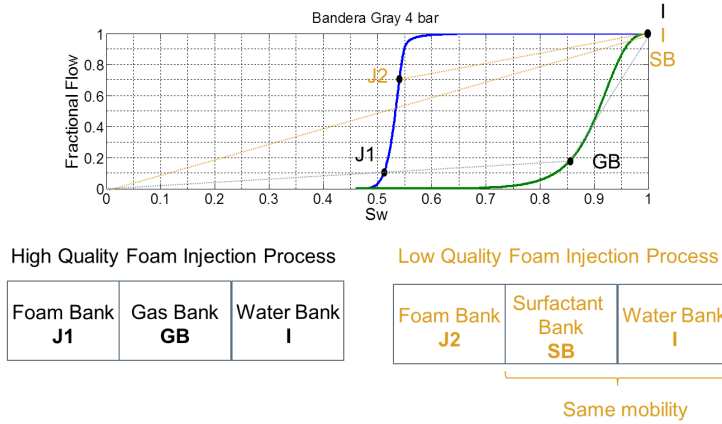


Figure 2.5: Construction of displacement for foam injection on fractional-flow curve (in this case, for Bandera Gray, using foam parameters corresponding to 4 bar/m). $J1$ represents injection of a foam with formation of a gas bank ahead of it (drawn in black), and $J2$ injection of a foam with no gas bank ahead (drawn in orange). In this case, with no surfactant adsorption, a diagonal line from the origin to I separates the two cases.

Shear-thinning rheology is important for foam in the low-quality regime. Accounting for shear-thinning with the STARS model would be complex, requiring iterative estimation of mobilities and saturations at each time at each position. Moreover, the whole construction of the solution, with banks of uniform saturations, would not apply if mobility depends on position and time as well as saturation. If one represents non-Newtonian foam behavior as a function of superficial velocity rather than pressure gradient (Chen and Mohanty (2014)), then one can construct fractional-flow solutions for foam in a single layer in cylindrical flow (Rossen et al. (2011)). In this case mobility depends on water saturation and radial position (because total superficial velocity depends on radial position). In considering diversion between four layers here, however, this solution again becomes ungainly: injection rates into the four layers varies with time, and mobilities in the layers depend on injection rates which in turn depends on mobilities in all the layers: the fractional-flow solution is much more complex.

Therefore, for a simple illustration of the effects of non-Newtonian rheology in foam injection, we use the foam parameters for the three pressure gradients in Figure 2.1: 4, 40 and 400 bar/m, without accounting for varying pressure gradient radially within each layer or with time as injection rate shifts between layers. Even the lower value is greater than expected field pressure gradients, except close to an injection well. We choose not to extrapolate too far from the range of the pressure gradients in the ex-

periments, however. With the given range we illustrate the effects of non-Newtonian rheology on diversion in a simple, though not comprehensive or predictive, way.

2.2.3. DIVERSION BETWEEN LAYERS

The analysis above gives dimensionless injectivity ($1/P_D$) for each of the four formations as a function of pore volumes injected into each layer. It remains to combine these results into a representation of diversion between the four layers over time. All the properties of a given layer i , including dimensionless time t_D and injectivity as a function of time $P_D(t_D)$, now carry an additional subscript i to represent the value for the given layer. Also, we distinguish between dimensionless injectivity into a particular layer, $(1/P_{Di})$, and total injectivity $(1/P_{Dt})$; both are normalized by the injectivity of water into the given layer or the four-layer reservoir with water completely saturating the layer or reservoir. Also, we distinguish between dimensionless time for a layer, t_{Di} , i.e. layer pore volumes injected into that layer, and total dimensionless time, t_{Dt} , the reservoir pore volumes injected into the reservoir.

The fraction of an individual layer i 's pore volume to the total reservoir pore volume is

$$\frac{\pi(r_e^2 - r_w^2)h_i\phi_i}{\sum_{j=1}^4 \pi(r_e^2 - r_w^2)h_j\phi_j} = \frac{h_i\phi_i}{\sum_{j=1}^4 h_j\phi_j} = \frac{1}{4} \quad (2.4)$$

according to our choice of interval thicknesses to give equal pore volume to all layers. Because of this difference, a reservoir pore volume comprises four layer pore volumes. If all the injected fluid entered one layer i , a given increment in dimensionless time Δt_{Dt} for the reservoir would have no effect on the other three layers, while the dimensionless time in layer i would advance by $\Delta t_{Di} = (4\Delta t_{Dt})$.

We integrate forward by finite difference in time. At the start ($t = 0$), the fraction of fluid R_i injected into a given layer i simply reflects layer thicknesses and permeabilities:

$$R_i(t = 0) = \frac{k_i h_i}{\sum_{j=1}^4 k_j h_j} \quad (2.5)$$

this ratio determines the size of the surfactant slug injected into each layer before gas injection in a SAG process. Later, as injectivity into the various layers is affected by gas injection or foam,

$$R_i = \frac{k_i h_i / P_{Di}}{\sum_{j=1}^4 k_j h_j / P_{Dj}} \quad (2.6)$$

In figures below, R_i is labelled "injectivity ratio.". During an increment in reservoir dimensionless time, Δt_{Dt} , the increment in layer dimensionless time for layer i ,

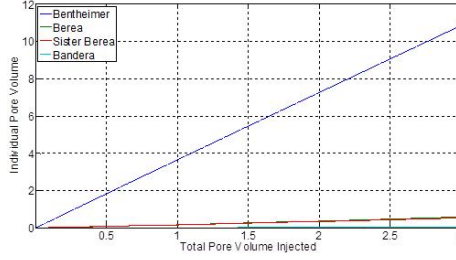


Figure 2.6: Cumulative layer pore volumes injected t_{Di} as function of total pore volumes injected t_{Dt} for gas injection without foam.

Δt_{Dt} , is

$$\Delta t_{Di} = \frac{k_i h_i / P_{Di}}{\sum_{j=1}^4 k_j h_j / P_{Dj}} 4 \Delta t_{Dt} \quad (2.7)$$

Because foam is so strong, in radial flow large changes in injectivity occur rapidly at the start. However, after the near-well region is filled with foam, injectivity changes more slowly. Therefore, we used 10000 time steps Δt_{Dt} , starting with 10^{-12} PV, and increase logarithmically in time up to 10 PV. At each time step we evaluate P_{Di} for each layer, determine the fraction of fluid injected into each layer in the next time step, and then increment dimensionless time in that layer according to the fluid injected into that layer.

As noted, overall injectivity ($1/P_{Dt}$) is normalized by injectivity of water at time zero (when $P_{Di} = 1$ in all layers):

$$P_{Dt} = \frac{\sum_{i=1}^4 k_i h_i}{\sum_{j=1}^4 k_j h_j / P_{Dj}} \quad (2.8)$$

2.3. RESULTS

We consider first gas injection with no foam. Then we examine foam injection, and finally SAG injection as a function of surfactant slug size, using both the STARS model and the modification proposed by Namdar Zanganeh et al. (2014) (Appendix A).

2.3.1. GAS INJECTION WITHOUT FOAM

Because high-mobility gas quickly sweeps the Bentheimer layer, making the injectivity contrast worse, vertical conformance is worse than indicated by the permeability ratios. Figure 2.6 shows the pore volumes injected into each layer over the first three reservoir pore volumes injected.

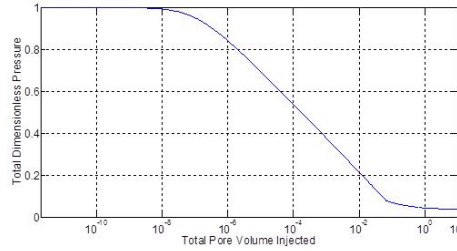


Figure 2.7: Dimensionless injection pressure P_{Dt} as function of total pore volumes injected t_{Dt} for gas injection without foam.

Injectivity, meanwhile, quickly increases. **Figure 2.7** shows the evolution of total injectivity over time (on a logarithmic time scale). Mostly this reflects the injectivity rise in the Bentheimer layer, and in particular the sweep of the near-wellbore region of that layer early in the process. In this and figures to follow, we plot dimensionless injection pressure P_{Dt} , i.e. the inverse of total injectivity.

2.3.2. FOAM INJECTION

In all four formations tested by Kapetas et al. (2017), foam reduced gas mobility greatly (Table 2.2). One expects an advantage of foam injection over the diversion shown in **Figure 2.1**, where foam fills all layers, because foam enters first and partially blocks the layers with the highest permeability. One also expects large declines in injectivity because foam is so strong in all layers. We show results for foam qualities of 0.5, 0.7, 0.9 and 0.99 ($f_w = 0.5, 0.3, 0.1$ and 0.01), using fixed foam parameters corresponding to pressure gradients of 4, 40 and 400 bar/m to illustrate the effect of shear-thinning on diversion with this foam.

Injectivity is indeed extremely poor (Table 2.3). Injectivity is somewhat better, and slower to decrease during injection, at the highest foam quality. Foam propagation is slower at low water fractions because foam propagation rate is limited by the small injected liquid fraction; as noted, adsorption, if included in the model, would further slow foam propagation at low water fraction. Injectivity decreases rapidly in all cases, however. **Figure 2.8** shows dimensionless injection pressure P_{Dt} for the case with the greatest injectivity, i.e., $f_w = 0.01$, and foam parameters corresponding to 400 bar/m.

Diversion into two of the layers is effective for the highest foam quality with foam parameters corresponding to 400 bar/m (**Figure 2.9**). In none of the cases is diversion effective into the lowest-permeability Bandera Gray layer, however. **Figure 2.10** shows vertical conformance with the same foam parameters (i.e., for 400 bar/m) with $f_w = 0.3$.

P_{Dt} at 1 PV injected

f_w	4 bar/m	40 bar/m	400 bar/m
0.01	300*	250*	145*
0.1	1200	1050	450*
0.3	1150	1050	450
0.5	900	850	370

Table 2.3: Dimensionless injection pressure P_{Dt} at one reservoir pore volume injected for foam injection at various foam qualities and foam parameters corresponding to various pressure gradients.

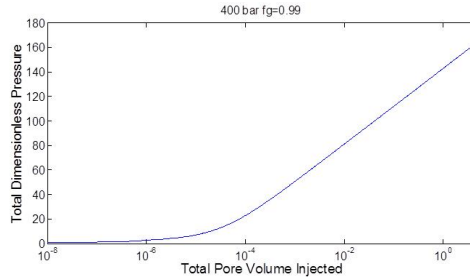


Figure 2.8: Dimensionless injection pressure P_{Dt} as function of reservoir pore volumes injected t_{Dt} for foam injection with $f_w = 0.01$ and foam parameters corresponding to 400 bar/m

For comparison, **Figures 2.11** and **2.12** show diversion for $f_w = 0.01$ using foam parameters corresponding to 40 and 4 bar/m, respectively. Clearly the effect of shear-thinning on foam parameters affects diversion in this case. In particular, foam in the Sister Berea layer, and to a lesser extent in the Berea layer, is more viscous at lower pressure gradient and this harms diversion into those layers.

Despite effective diversion attainable at the highest foam quality, extremely poor injectivity (**Table 2.3**) would make direct foam injection impractical in this hypothetical field application.

2.4. SAG INJECTION

As noted, during gas injection in a SAG process the entire foam bank exists at low water fractional flow, i.e. in the high-quality regime. Therefore we neglect the F_5 factor that accounts for non-Newtonian behavior in the STARS foam model for SAG injection (i.e., assume $F_5 = 1$). Within the foam bank, total relative mobility varies between its value at the shock and at S_{wr} (**Fig. 2.4**). Foam mobility at S_{wr} dominates the near-well region and is crucial to injectivity and diversion. Therefore, it is extremely important whether foam completely collapses as foam dries out to S_{wr} .

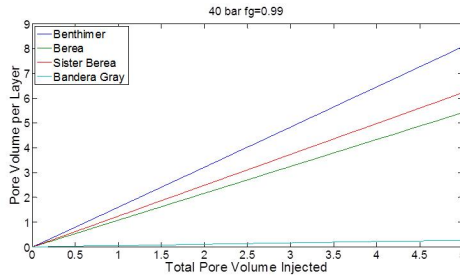


Figure 2.9: Layer pore volumes injected t_{Di} as function of total pore volumes injected t_{Dt} for 99 %-quality ($f_w = 0.01$) foam injection with foam parameters corresponding to 400 bar/m.

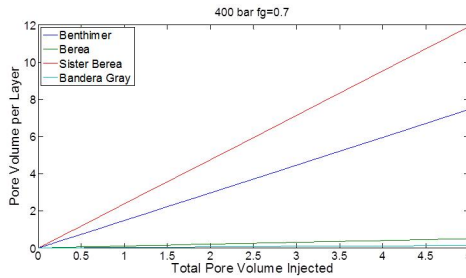


Figure 2.10: Layer pore volumes injected t_{Di} as function of total pore volumes injected t_{Dt} for 70%-quality ($f_w = 0.3$) foam injection with foam parameters corresponding to 400 bar/m.

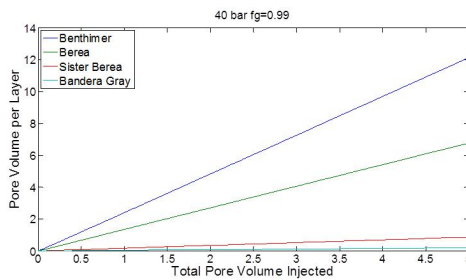


Figure 2.11: Dimensionless injection pressure P_{Dt} as function of reservoir pore volumes injected t_{Dt} for foam injection with $f_w = 0.01$ and foam parameters corresponding to 40 bar/m

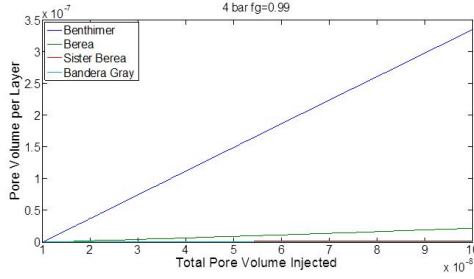


Figure 2.12: Dimensionless injection pressure P_{Df} as function of reservoir pore volumes injected t_{Df} for foam injection with $f_{iw} = 0.01$ and foam parameters corresponding to 4 bar/m

Layer	$S_{w,shock}$	$(\frac{df_w}{dS_w})_{S_{w,shock}}$	$(\lambda_{rt})_{S_{w,shock}}$	S_{wr}	$(\lambda_{rt})_{S_{wr}}$
Bentheimer	0.266	1.36	4.10	0.25	16.4
Berea	0.328	1.48	20.0	0.23	369.0
Sister Berea	0.393	1.64	43.4	0.25	2760
Bandera Gray	0.507	1.99	8.77	0.46	22.8

Table 2.4: Properties of Foam Predicted for Gas Injection in SAG in Each Layer for Parameters Fit to STARS Foam Model. Total relative mobilities λ_{rt} are given in $(Pas)^{-1}$.

For this reason, we consider two cases, the model fit of Kapetas et al. (2017) using the STARS foam model, and the same model parameters applied in the modification proposed by Namdar Zanganeh et al. (2014), in which foam collapses completely at S_{wr} (see **Appendix A**). **Tables 2.4** and **2.5** show total relative mobility with foam just behind the shock (i.e., at the leading edge of the foam bank) and at S_{wr} for the four layers, for both the original STARS model fit and for the Namdar Zanganeh model. The Namdar Zanganeh adjustment to the model makes little difference to the mobility or velocity of the shock, but an enormous difference to mobility near the injection well.

Layer	$S_{w,shock}$	$(\frac{df_w}{dS_w})_{S_{w,shock}}$	$(\lambda_{rt})_{S_{w,shock}}$	S_{wr}	$(\lambda_{rt})_{S_{wr}}$
Bentheimer	0.266	1.36	5.10	0.25	29500
Berea	0.328	1.48	21.3	0.23	49500
Sister Berea	0.393	1.64	44.3	0.25	23500
Bandera Gray	0.511	2.01	13.5	0.46	36500

Table 2.5: Properties of Foam Predicted for Gas Injection in SAG in Each Layer for Parameters Used in Namdar Zanganeh Model. Total relative mobilities λ_{rt} are given in $(Pas)^{-1}$.

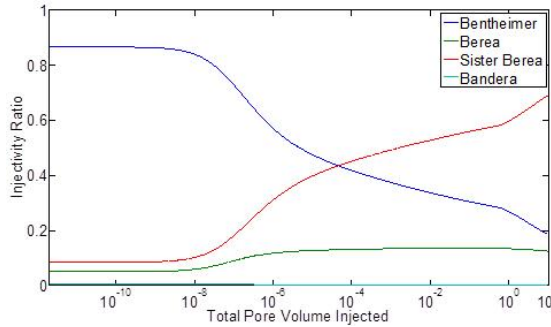


Figure 2.13: Relative gas injection rate R_i (Eq. 2.6) into the four layers as a function of total pore volumes injected t_{Dt} for gas injection in SAG with surfactant initially saturating all layers; STARS foam model.

We examine three cases: a) all four layers fully saturated with surfactant. b) finite surfactant slug preceding gas injection. The surfactant slug enters the various layers according to the layer heights and permeabilities. c) finite surfactant slugs pumped into the Bentheimer, Berea and Sister Berea layers, with no surfactant injection into the Bandera Gray layer. Gas is then injected into all four layers.

2.4.1. SURFACTANT FILLING ALL LAYERS

Figs. 2.13 and 2.14 show gas injection rate and cumulative gas injection into the four layers over time using the STARS model fit, on a logarithmic and linear time scale, respectively. The small value for $epdry$ for the Bentheimer layer means mobility remains low near the well there even after a long period of gas injection (Table 2.4, Fig. 2.4). In contrast, the larger value of $epdry$ for the Sister Berea layer means foam weakens near the well and injectivity rises over time. Therefore, early in gas injection (less than 10^{-4} PV injection) injection into the Sister Berea layer surpasses that into the Bentheimer layer. Fig. 2.15 shows overall injectivity over time. It is much better than for foam injection (Table 2.3), but still poor.

With the Namdar-Zanganeh modification of the STARS model, mobility increases in the Bentheimer layer as well as the near-well region dries out. More flow passes into that layer (Fig. 2.16) and dimensionless injection pressure P_{Dt} (not shown) peaks at about 17 instead of 26.

2.4.2. FINITE SURFACTANT SLUGS

By far most of the surfactant slug enters the Bentheimer layer, and hence the foam bank is much larger in that layer; the fractions of total surfactant injection into the Bentheimer, Berea, Sister Berea and Bandera Gray layers are 0.864, 0.049, 0.083 and

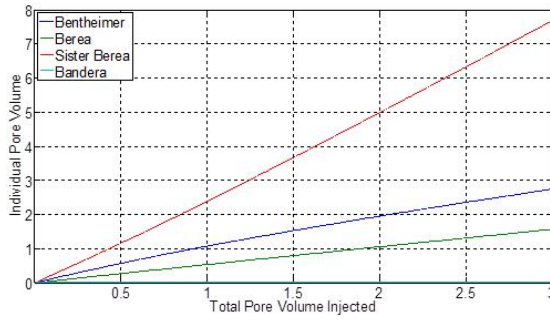


Figure 2.14: Cumulative gas injection into the four layers t_{Di} as a function of total pore volumes injected t_{Dt} for gas injection in SAG with surfactant initially saturating all layers; STARS foam model.

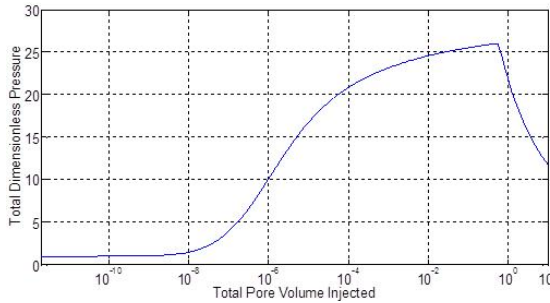


Figure 2.15: Dimensionless injection pressure P_{Dt} as function of total pore volumes injected t_{Dt} for gas injection in SAG with surfactant initially saturating all layers; STARS foam model.

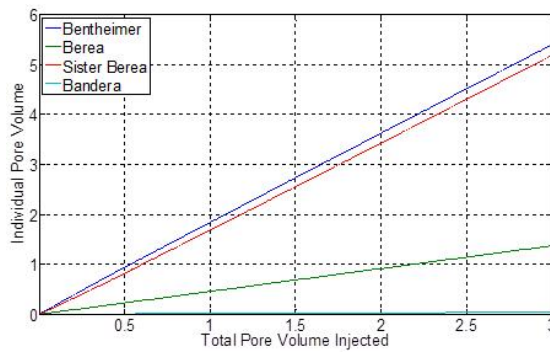


Figure 2.16: Cumulative gas injection into the four layers t_{Di} as a function of total pore volumes injected t_{Dt} for gas injection in SAG with surfactant initially saturating all layers; Namdar Zanganeh model.

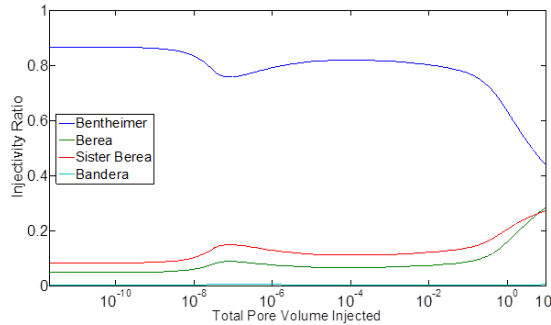


Figure 2.17: Fraction of gas injected into the four layers R_i over time for a SAG process with a 10^{-8} PV surfactant slug; STARS foam model.

0.003, respectively. However, in radial flow the effect of this difference decreases if enough surfactant is injected to place a foam bank around the injection well in all layers. Because the foams studied by Kapetas et al. (2017) were strong in all the layers, small slugs of surfactant suffice to divert flow.

STARS model

Figs. 2.17, 2.18 and 2.19 show the fraction of total gas injection into each of the four layers over time for surfactant slugs of 10^{-8} , 10^{-7} and 10^{-6} PV. Time is shown on a logarithmic scale to emphasize dynamics at early times. On such a scale, the injection ratios at times near 10^0 (1 PV injection) represent most of the gas injection. The optimal surfactant slug size for diversion is about 10^{-7} PV, which would put a foam bank a few cm deep around the 10-cm injection wellbore in the Bentheimer layer; less in the other layers. **Fig. 2.20** shows cumulative gas injection over time into all layers for a surfactant slug of 10^{-7} PV. For larger surfactant slugs, injection into both the Bentheimer and Berea layers suffers at the expense of the Sister Berea layer, as is already evident with a 10^{-6} PV surfactant slug.

Fig. 2.21 shows dimensionless injection pressure P_{Di} over time for a range of surfactant slug sizes. For a surfactant slug of 10^{-7} PV, the red curve indicated by the arrow, P_{Di} briefly rises but then drops to a value less than 1. It takes less time to inject 1 PV gas in this SAG process than to inject 1 PV water into a water-saturated reservoir.

Namdar Zanganeh model

In the Namdar Zanganeh et al. (2014) modification of the STARS foam model, mobility near the injection well increases with time in even the Bentheimer layer after long gas injection (**Table 2.5**). Therefore larger surfactant slugs are required for effec-

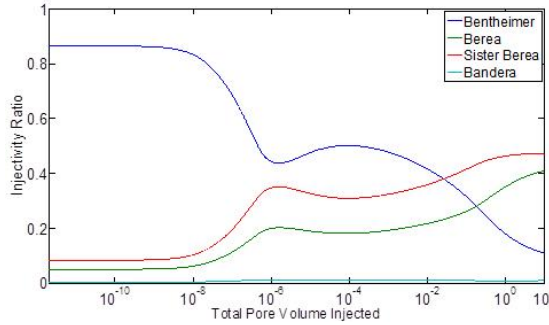


Figure 2.18: Fraction of gas injected into the four layers R_i over time for a SAG process with a 10^{-7} PV surfactant slug; STARS foam model.

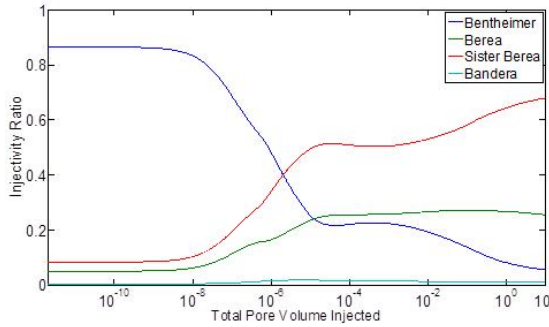


Figure 2.19: Fraction of gas injected into the four layers R_i over time for a SAG process with a 10^{-6} PV surfactant slug; STARS foam model.

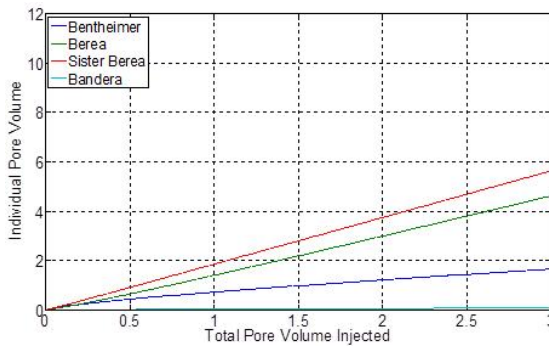


Figure 2.20: Cumulative gas injection into the four layers t_{Di} over time for a SAG process with a 10^{-7} PV surfactant slug; STARS foam model.

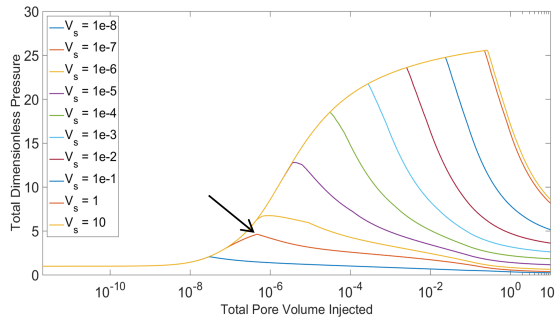


Figure 2.21: Dimensionless injection pressure P_{DI} vs. time for SAG process with various surfactant slug sizes; STARS foam model. Arrow indicates 10^{-7} PV surfactant slug.

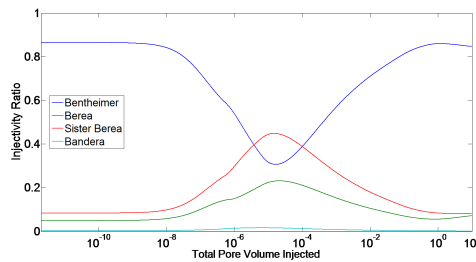


Figure 2.22: Fraction of gas injected into the four layers R_i over time for a SAG process with a 10^{-6} PV surfactant slug; Namdar Zanganeh foam model.

tive diversion. **Figs. 2.22, 2.23, 2.24** and **2.25** show the fraction of total gas injection R_i (**Eq. 2.6**) into each of the four layers over time for surfactant slugs of 10^{-6} , 10^{-4} , 10^{-2} and 1 PV. For a 10^{-4} PV surfactant slug, diversion into the Sister Berea layer, and to a lesser extent the Berea layer, is effective. For a 10^{-2} PV slug the Sister Berea layer takes most of the gas, while for a 1 PV slug the Bentheimer and Sister Berea layers share most of the injected gas.

Injectivity considerations (**Fig. 2.26**) favor the smaller (10^{-4} PV) surfactant slug. With this slug, it is possible to inject a pore volume of gas more easily than injecting a pore volume of water into a water-saturated reservoir. This surfactant slug size gives roughly equal injection into the Bentheimer and Sister Berea layers, and some diversion into the Berea layer, though no diversion into the Bandera Gray layer (**Fig. 2.27**).

We focus on vertical conformance at the well in this study and neglect gravity override within the layers. If gravity override were an issue, larger surfactant slugs would be needed. Once gas breaks through the surfactant bank in each layer it would rapidly segregate to the top of that layer. Single-slug SAG processes like those exam-

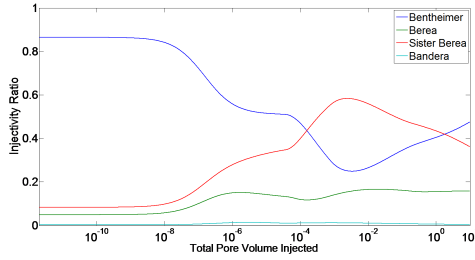


Figure 2.23: Fraction of gas injected into the four layers R_i over time for a SAG process with a 10^{-4} PV surfactant slug; Namdar Zanganeh foam model.

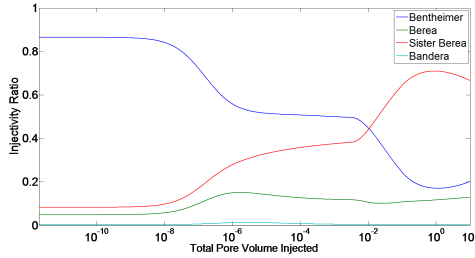


Figure 2.24: Fraction of gas injected into the four layers R_i over time for a SAG process with a 10^{-2} PV surfactant slug; Namdar Zanganeh foam model.

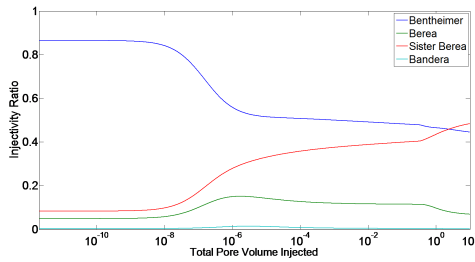


Figure 2.25: Fraction of gas injected into the four layers R_i over time for a SAG process with a 1 PV surfactant slug; Namdar Zanganeh foam model.

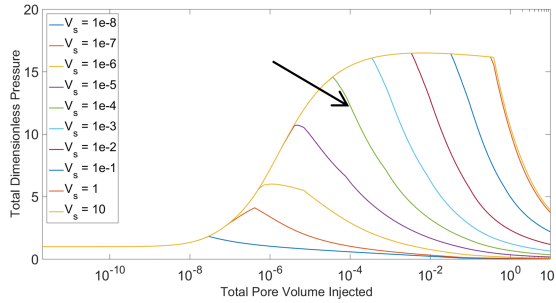


Figure 2.26: Dimensionless injection pressure P_{Dt} vs. time for SAG process with various surfactant slug sizes; Namdar Zanganeh model. Arrow indicates 10^{-4} PV surfactant slug.

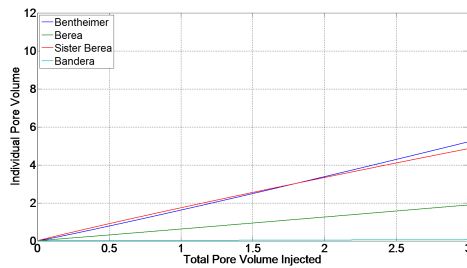


Figure 2.27: Cumulative gas injection into the four layers over time for a SAG process with a 10^{-4} PV surfactant slug; Namdar Zanganeh model.

ined here can be very effective at controlling gravity override as long as surfactant stays ahead of the front of the gas bank (Grassia et al., 2014; Shan and Rossen, 2004).

No foam in the lowest-permeability layer

None of the injection strategies described above diverts flow effectively into the Bandera Gray layer. We consider therefore a design where surfactant is injected into the other three layers, but not into the Bandera Gray layer. As above, we consider cases with surfactant completely filling all layers and finite surfactant slugs, and use the STARS model fit and the Namdar Zanganeh model modification.

With surfactant solution completely filling the other three layers, and using the STARS model, the greatest flow goes into the Bandera Gray layer (Fig. 2.28), despite the large permeability contrast. Mobility increases in the Bandera Gray layer upon gas injection, even as foam reduces mobility in the other layers. Injectivity is poor, however; it takes 12 times as long to inject a pore volume of gas in this process as to inject a pore volume of water into a water-saturated reservoir. With the Namdar Zan-

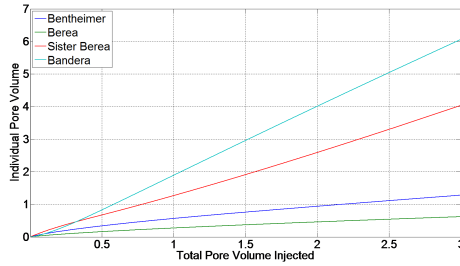


Figure 2.28: Cumulative gas injection into the four layers t_{Di} over time for a SAG process with surfactant filling all layers except the Bander Gray layer; STARS foam model.

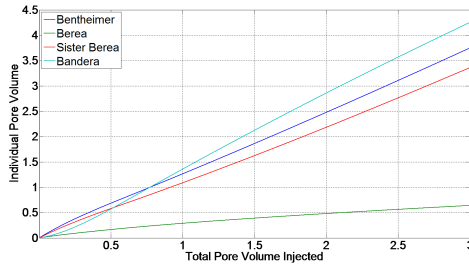


Figure 2.29: Cumulative gas injection into the four layers t_{Di} over time for a SAG process with surfactant filling all layers except the Bander Gray layer; Namdar Zanganeh model.

ganeh model (Fig. 2.29), the Bentheimer, Sister Berea and Bandera Gray layers take roughly equal gas flow, with less than 10% entering the Berea layer. Injecting 1 PV of gas takes roughly 10 times as long as injecting 1 PV of water into a water-saturated reservoir.

With finite surfactant slugs, large slugs are needed to equalize flow between the Bentheimer, Sister Berea and Bandera Gray layers, while the Berea layer receives less gas. Using the STARS model, for surfactant slugs between 10^{-6} and 0.1 PV, the Sister Berea layer gets most of the flow (Fig. 2.30). For a 1 PV surfactant slug, the Bandera Gray and Sister Berea layers share most of the flow. Fig. 2.31 shows gas injectivity over time for various sizes of surfactant slugs. With a 1 PV surfactant slug injected before gas, the Bentheimer layer receives over 3 PV of surfactant because of the initial permeability contrast. Furthermore, with a 1 PV surfactant slug, it would take about 8 times as long to inject 1 PV gas as to inject the same volume of water into a water-saturated reservoir.

With the Namdar Zanganeh model, the Bentheimer layer takes most gas flow for

surfactant slug sizes of 10^{-8} and 10^{-7} PV, and the Sister Berea layer for slug sizes from 10^{-3} to 0.1 PV. For a 1 PV surfactant slug, there is roughly equal gas injection into the Bandera Gray, Bentheimer and Sister Berea layers, with less than 10% of the gas entering the Berea layer (Fig. 2.32). With a 1 PV surfactant slug, it would take about six times as long to inject 1 PV of gas compared to injecting water into a water-saturated reservoir.

2.5. DISCUSSION

This study makes a number of simplifying assumptions. We neglect gravity effects, both between layers and leading to override within layers, and the effects of oil and oil displacement on foam. We assume each layer is homogeneous within itself, and we assume foam comes to local equilibrium (LE) instantaneously. Especially in cases where the foam bank is only cm deep around a well, the "entrance effect" (foam coming to local equilibrium over a distance of cm (Ransohoff and Radke, 1988) would be important. Slow approach to local equilibrium is especially problematic for initial gas injection in SAG processes (Kapetas et al., 2014). Population balance models can in principle account for this effect (Ashoori et al., 2011a,b; Kam et al., 2007; Kovscek and Radke, 1994; Kovscek et al., 2010), but most current applications of population-balance models predict that foam comes rapidly to LE. Ignoring capillary-pressure gradients and dispersion and treating the shock as a discontinuity in saturation could be problematic if the entire foam bank is only cm deep around the well. We also exclude the effects of compressibility on gas superficial velocity. Compressibility affects gas superficial velocity, which is relatively unimportant in the high-quality regime crucial to gas injection in a SAG process (Alvarez et al., 2001). Compression or expansion of gas would affect the size of the gas or foam bank, but this effect become less important as gas moves beyond the near-well region. In addition, for carbon dioxide foam applications, the gas solubility effect could be significant.

A numerical simulation could incorporate all these effects, but numerical simulations, which do not represent the shock front in a SAG process accurately, cannot represent the injectivity of a SAG process as well as fractional-flow methods. without extraordinary grid refinement around the injection well (Leeftink et al., 2015).

To illustrate the effects of foam model parameters on predicted diversion, we extrapolate data taken at ideal conditions (low temperature, no oil, low salinity, etc.) to a hypothetical field case. We also extrapolate to pressure gradients in the field likely to be very different from those measured in the laboratory. This is seen directly in the effect of pressure gradient on diversion; but, more fundamentally, any model fit extrapolated to pressure gradients so different from those in the laboratory would be uncertain. The approach used here could be applied to data for field application of foam under more realistic conditions as such data become available.

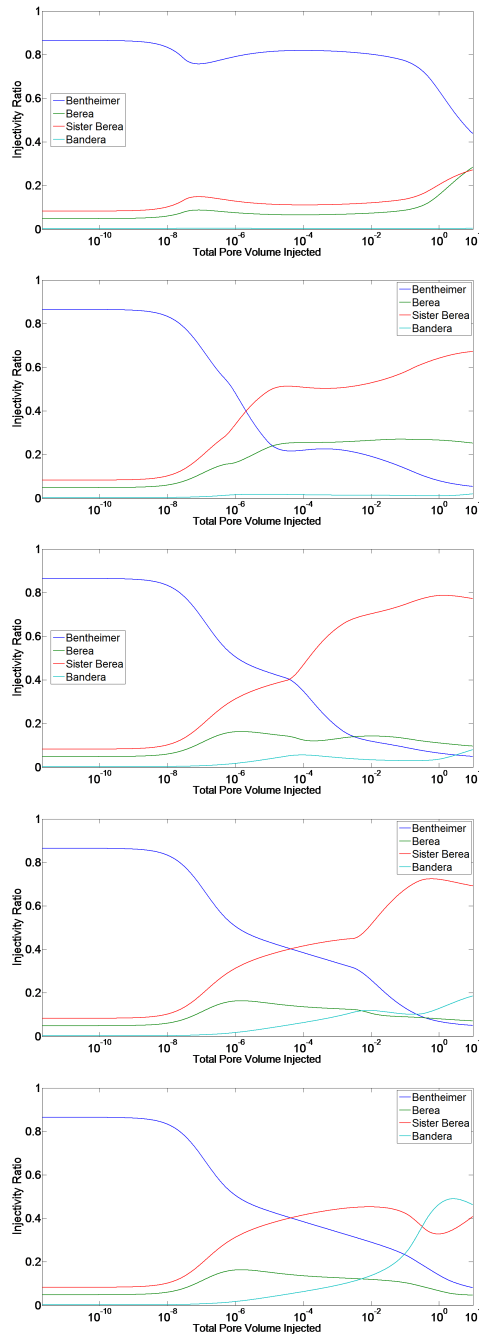


Figure 2.30: Fraction of gas injected into the four layers R_i over time for a SAG process with finite surfactant slug injected into layers excluding the Bandera Gray layer; STARS foam model. From top to bottom, 10^{-8} , 10^{-6} , 10^{-4} , 10^{-2} and 1 PV surfactant slugs.

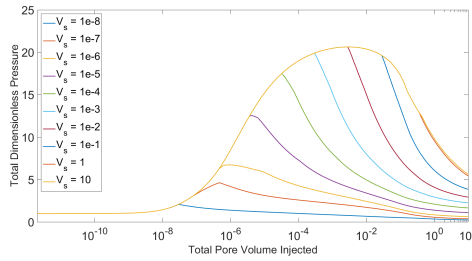


Figure 2.31: Dimensionless injection pressure P_{Dt} vs. time for SAG process with various surfactant slug sizes injected into all layers except the Bandera Gray layer; STARS foam model.

This study illustrates the difficulty in assigning a ranking of foam strength based on individual foam-model parameters. Based on $fmmob$, the reference gas-mobility reduction in the low-quality regime, the strongest foam by far (by over a factor of 10) is in the Berea formation (Table 2.2). Comparisons of $fmmob$ where the non-Newtonian factor F_5 is included must refer to the product of F_5 and $fmmob$ at a particular pressure gradient or superficial velocity. More fundamentally, the value of $fmmob$ is a reference value at the reference capillary number (in essence, a reference pressure gradient) $fmcap$; its value can be altered by an adjustment of $fmcap$ without altering the fit to the data. This casts further doubt on comparisons based on $fmmob$ alone. Table 2.6 shows values of the product ($F_5 fmmob$) at pressure gradients 400 bar/m, 40 bar/m (in the range of the experimental data), and 4 bar/m. At 40 bar/m by far the strongest foam in the low-quality regime is in the Sister Berea layer, while foam is stronger in the Bandera Gray formation than the Bentheimer formation. Extrapolated to 4 bar/m, foam virtually plugs the Sister Berea formation, is extremely strong in the Berea formation, and is again stronger in the Bandera Gray formation than in Bentheimer. Extrapolated to 400 bar/m, foam is much weaker in the Sister Berea formation than any of the others, and foam is weaker in the Bandera Gray formation than in Bentheimer.

In radial flow, the effect of shear-thinning foam mobility is more complex than represented here. Cheng et al. (2000) note that if one represents gas as a shear-thinning power-law fluid, the power-law exponent n is roughly $(1/(1+epcap))$. Thus a value of $epcap = 4.39$ in the Sister Berea (Table 2.2) layer corresponds to a power-law exponent (Bird et al., 2006) of $n \approx 0.23$. In our model total superficial velocity varies by a factor of 1000 from the 0.1-m wellbore radius to the outer radius of 100 m. For Newtonian fluids, this would mean that pressure gradient is 1000 times larger at the wellbore than at the outer radius. For $n = 0.23$, however, this ratio is only 4.8. The effect of radial flow on pressure gradient and diversion is much different for fluids showing such strong shear-thinning behavior.

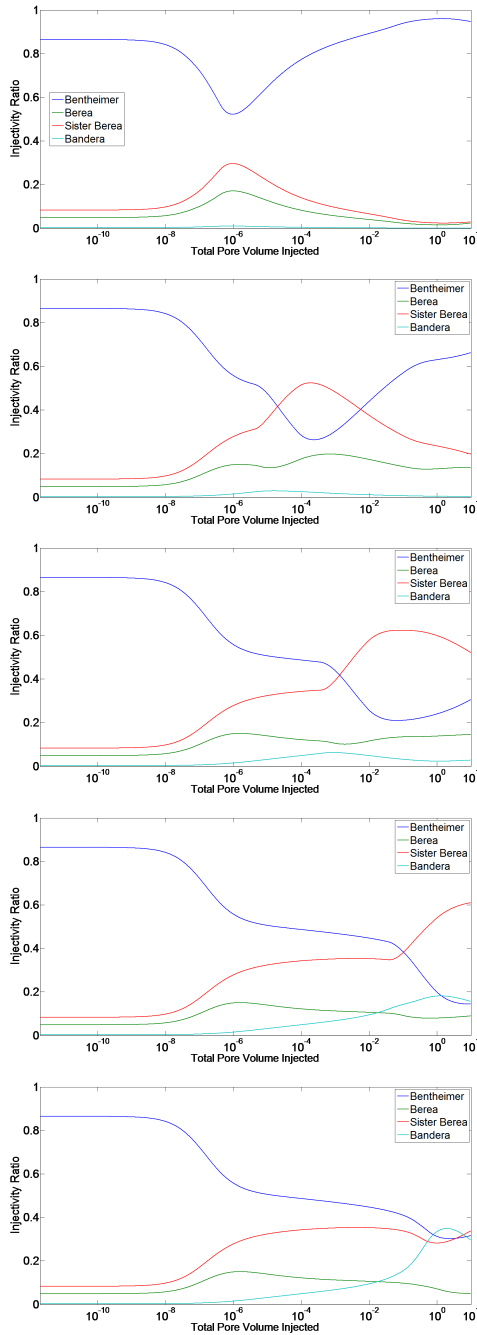


Figure 2.32: Fraction of gas injected into the four layers R_i over time for a SAG process with finite surfactant slug injected into layers excluding the Bandera Gray layer; Namdar Zanganeh foam model. From top to bottom, 10^{-8} , 10^{-6} , 10^{-4} , 10^{-2} and 1 PV surfactant slugs.

For foam injection at a fixed quality in the high-quality regime, total relative mobility depends on $fmdry$ (Boeije and Rossen, 2015a). Direct comparison based on values of $fmdry$ is complicated by the different values of S_{wr} and relative-permeability functions between the formations, however. For foam of a fixed quality, total relative mobility in the high-quality regime is proportional to water relative permeability at the limiting water saturation ($fmdry$ in the STARS model):

$$\lambda_{rt} \approx \frac{k_{rw}(fmdry)}{\mu_w f_w} \quad (2.9)$$

This equation is exact in the limit $epdry \rightarrow \infty$. Thus at fixed quality in the high-quality regime, foam is 48, 7 and 7.4 times as strong in the Bentheimer, Berea and Sister Berea formations as in Bandera Gray (Table 2.6). The "limiting capillary pressure" concept leads one to expect this result: stronger foam in higher-permeability formations in the high-quality foam regime (Alvarez et al., 2001; Apaydin and Kovscek, 2001; Khatib et al., 1988; Rossen and Zhou, 1995). This effect suffices to compensate partially, but not fully, for the permeability contrast between the layers here.

For a SAG process, mobility at the foam front reflects an interplay of $fmdry$, $epdry$ and $fmmob$, which together determine the point of tangency at the shock (Fig. 2.3) and mobility behind the shock (Tables 2.4 and 2.5). Injectivity and diversion depend also on mobility at S_{wr} , i.e. mobility at the well; this depends especially on $epdry$ (as well as $fmmob$) in the STARS model. A model fit to data over a wide range of foam qualities may misrepresent the behavior of foam during gas injection in a SAG process; the difference between the STARS and Namdar Zanganeh models here illustrate the importance of data at very high foam quality (cf. Rossen and Boeije (2015)). Evaporation of water into injected gas (Pickup et al., 2012) could also weaken or destroy foam near the well.

Based on mobility at the shock, the foam studied here is strongest in the Bentheimer formation, followed by Bandera Gray. Ironically, the Bandera Gray formation has the weakest foam at fixed foam quality in the high-quality regime ($k_{rw}(fmdry)$ - Table 2.6). In the STARS model a ranking based on mobility at S_{wr} (Table 2.4) is in the same order as one based on relative mobility at the shock, but the contrast is by one to more than two orders of magnitude rather than a factor of five to ten at the shock (Table 2.4). If foam collapses completely at S_{wr} , as in the Namdar Zanganeh model (Table 2.5), then total relative mobility is nearly the same among the layers close to the well. Field data on long-term gas injection in a single-slug SAG process in the Cusiana field in Colombia (which involved a much-weaker foam than that represented here) suggests that foam does approach complete foam collapse at S_{wr} , though perhaps not as rapidly as in the Namdar Zanganeh model (Rossen et al., 2017).

Layer	$fmmobF_5$ 4 bar/m	$fmmobF_5$ 40 bar/m	$fmmobF_5$ 400 bar/m	$fmdry$	$k_{rw}(fmdry)$
Bentheimer	47200	46200	45100	0.271	3.43×10^{-5}
Berea	6.07×10^6	726000	86700	0.336	2.34×10^{-4}
Sister Berea	4.14×10^{11}	1.68×10^7	684	0.396	2.18×10^{-4}
Bandera Gray	250000	90700	33000	0.549	1.63×10^{-3}

Table 2.6: Properties of Foam Predicted for Gas Injection in SAG in Each Layer for Parameters Used in Namdar Zanganeh Model. Total relative mobilities λ_{rt} are given in $(Pas)^{-1}$.

2.6. SUMMARY AND CONCLUSIONS

This is the first study to apply foam model parameters fit to the two foam flow regimes for the same surfactant formulation over this wide range of permeabilities, in a comparison of vertical conformance with different injection strategies with foam. The foam parameters of Kapetas et al. (2017) represent ideal conditions (low salinity, low temperature, and absence of oil). They measured very low mobilities, lower than would be practical to apply in the field. Nevertheless, we believe the following conclusions apply more broadly.

The only process that gave effective diversion into the lowest-permeability layer (300 times lower permeability than the highest-permeability layer) was a SAG process that isolated the lowest-permeability layer from receiving surfactant injection. One of the other layers (Berea) still failed to get an equal share of gas in that process.

Single-slug SAG processes have much better injectivity than foam injection, especially if foam collapses at residual water saturation S_{wr} (as in the Namdar Zanganeh model). In some SAG processes examined here, with successful diversion of foam into two of the three lower-permeability layers, injectivity is better with foam than injecting water into a water-saturated reservoir.

Single-slug SAG processes have the additional advantage that most surfactant is injected into the highest-permeability layer, giving the largest foam bank there. With the extremely strong foams modeled here, very small surfactant slugs suffice for effective diversion. The advantage remains during subsequent gas injection in SAG, unlike diversion in direct foam injection, in which foam eventually fills the near-wellbore region of all layers.

It is extremely important whether foam collapses at S_{wr} , both for diversion and injectivity in SAG processes. This is reflected here in the different results for the STARS model and the Namdar Zanganeh modification of that model. A process of direct foam injection performs better than in the plots of Kapetas et al. (Fig. 2.1)

because more foam is placed over time in the layers taking most of the flow. This advantage declines with time as foam fills more of all the layers.

Diversion between layers reflects an interplay between various foam parameters. For foam injection, in the low-quality regime, total relative mobility depends on $fmmob$, the mobility reduction in the low-quality regime, and $epcap$, which rescales $fmmob$ with pressure gradient (i.e., introduces non-Newtonian behavior); see **Table 2.6**. In the high-quality regime, if $epdry$ is large, mobility depends most of all on $fmdry$, the water saturation at which foam collapses. We have only illustrated the effects of non-Newtonian behavior in the low-quality regime here, for simplicity, but that effect is significant, as illustrated in **Figs. 2.9, 2.10, 2.11** and **2.12**. For SAG injection, diversion depends on mobility at the shock, which depends on several foam parameters, and on whether foam collapses completely at irreducible water saturation.

3

FRACTIONAL-FLOW THEORY FOR NON-NEWTONIAN SURFACTANT-ALTERNATING-GAS FOAM PROCESSES

Foam can improve sweep efficiency in gas-injection enhanced oil recovery. Surfactant-alternating-gas (SAG) is a favored method of foam injection due to injectivity and operational considerations. Laboratory data indicate that foam can be non-Newtonian at low water fractional flow f_w , and therefore during gas injection in a SAG process. We investigate the implications of this finding for mobility control and injectivity, by extending fractional-flow theory to gas injection in a non-Newtonian SAG process in radial flow.

Non-Newtonian behavior at low f_w implies that the limiting water saturation for foam stability varies as superficial velocity decreases with radial distance from the well. We discretize the domain radially and perform Buckley-Leverett analysis on each narrow increment in radius. As solution characteristics move outward, they maintain constant f_w . For the first time, we show the implications of this behavior for mobility control at the displacement front as well as for injectivity. We base the foam-model parameters and the extent of non-Newtonian behavior on laboratory data in the absence of oil. We compare results to mobility and injectivity determined by conventional simulation, where grid resolution is usually limited.

For shear-thinning foam, mobility control improves as the foam front propagates from the well, but injectivity declines somewhat with time. The change of mobility ratio at the front can be considerable, given the huge velocity difference between the well-

bore and further out. This change is not simply that measured at steady state at fixed water fractional flow in the laboratory, however, because the shock front in a non-Newtonian SAG process does not propagate at fixed fractional flow (though individual characteristics do). Moreover, the shock front is not governed by the conventional condition of tangency of the shock to the fractional-flow curve, though it continually approaches this condition. Injectivity benefits from the increased mobility of shear-thinning foam near the well. The foam front, which maintains a constant dimensionless velocity for Newtonian foam, decelerates somewhat with time for shear-thinning foam. For shear-thickening foam, mobility control deteriorates as the foam front advances, though injectivity improves somewhat with time. Overall, however, injectivity suffers from reduced foam mobility at high superficial velocity near the well. The foam front accelerates somewhat with time. Overall, mobility and injectivity are complex results of changing saturations and varying superficial velocities with distance from the well. Conventional simulators cannot adequately represent these effects, or estimate injectivity accurately, in the absence of extraordinarily fine grid resolution near the injection well.

3.1. INTRODUCTION

3.1.1. FRACTIONAL-FLOW THEORY

Fractional-flow theory, or the method of characteristics, has proved useful for understanding foam displacements in porous media (Al Ayyesh et al., 2017; Ashoori et al., 2010; Boeije and Rossen, 2015b; Lake et al., 2014; Namdar-Zanganeh et al., 2011; Rossen et al., 2011; Rossen et al., 1999; Zhou and Rossen, 1994). Its predictions are not rigorous because of the number of simplifying assumptions made, but they provide valuable insights, even if the assumptions are not strictly satisfied. This theory applies to Newtonian displacements directly and it has been extended to model a collection of non-Newtonian foam cases (Rossen et al., 2011). In this paper we make the usual assumptions of fractional flow theory (Rossen et al., 2011), namely:

1. One-dimensional (radial or linear) flow.
2. Two mobile and incompressible phases.
3. Instantaneous equilibrium adsorption of surfactant on rock. In this study, for simplicity we assume adsorption was satisfied during injection of the preceding liquid slug.
4. No dispersive processes, including fingering, capillary diffusion or dispersion.
5. Instantaneous attainment of local steady-state mobilities, which depend on local saturations. In this study, mobilities depend on total superficial velocity as well.
6. No chemical or biological reactions.

In addition, in this study of non-Newtonian flow, we make an additional assumption:

7. Fixed total volumetric flow rate Q .

The isothermal flow of two immiscible and incompressible fluids through a permeable medium is governed by the following equation (Lake et al., 2014):

$$\frac{\delta S_w}{\delta t_D} + \frac{f_w}{x_D} = 0 \quad (3.1)$$

where t_D and x_D denote dimensionless time and position, respectively, and S_w and f_w denote liquid saturation and liquid fractional flow, respectively. The dependence of t_D and x_D on the geometry of a cylindrical reservoir with wellbore radius r_w and open outer boundary radius r_e is described by the following equations:

$$x_D = \frac{r^2 - r_w^2}{r_e^2 - r_w^2} \quad (3.2)$$

$$t_D = \frac{Qt}{\pi(r_e^2 - r_w^2)h\phi} \approx \frac{Qt}{\pi r_e^2 h\phi} \quad (3.3)$$

where ϕ and h denote porosity and the thickness of the reservoir, respectively.

The superficial velocity of an incompressible fluid injected at a fixed rate Q into a cylindrical reservoir decreases continuously from the wellbore radius to the outer radius. This implies that a non-Newtonian fluid experiences not only a different superficial velocity, but a different rheology, as a function of radial position. Mathematically this means that f_w is a function of S_w and x_D . The fractional-flow analysis with this additional constraint results in characteristics that in general do not have a fixed dimensionless velocity (Rossen et al., 2011; Wu et al., 1993). Liquid fractional flow is fixed for each characteristic as it travels through the porous medium, although liquid saturation is not.

3.1.2. FOAM IN POROUS MEDIA

Foam increases sweep efficiency during gas injection in enhanced-oil-recovery applications (Blaker et al., 2002; Lake et al., 2014). It is also used in aquifer remediation projects and in acid diversion in well-stimulation treatments (Cheng et al., 2002; Hirasaki et al., 1997). Foam flow in porous media exhibits two flow regimes: a low-quality (large f_w) regime and a high-quality (small f_w) regime (Alvarez et al., 2001; Osterloh and Jante, 1992). The low-quality regime is characterized by a gas-mobility reduction and a pressure gradient independent of liquid superficial velocity, whereas the high-quality regime is characterized by a limiting capillary pressure P_c^*

and a pressure gradient independent of gas superficial velocity. Foam can be non-Newtonian in both regimes. The rheology in the low-quality regime is found to be consistently shear-thinning with respect to total superficial velocity at fixed f_w , but it can be either shear-thickening or shear-thinning in the high-quality regime. **Figure 3.1** shows two examples. On the left, foam is shear-thinning with respect to liquid superficial velocity, or with respect to total superficial velocity at fixed f_w . An increase in velocity produces a less-than-proportional increase in pressure gradient. On the right, foam is shear-thickening with respect to liquid superficial velocity.

“Implicit Texture” models, here referred to as “IT” models for simplicity, are regularly used in combination with fractional-flow theory to describe foam displacements (AlAyesh et al., 2017; Rossen et al., 2011). Unlike “Population Balance” models, they assume local equilibrium in the dynamics of bubble creation and destruction and represent the effects of foam on gas mobility through a mobility-reduction factor (Chen and Mohanty, 2014). “Population Balance” models can also be constrained to conditions of local equilibrium between foam-generation and -destruction processes (Kam et al., 2007; Kovscek et al., 2010). In the present study we use an IT model because it requires fewer parameters and avoids some of the numerical challenges that are present in “Population Balance” models (Ashoori et al., 2012).

Most IT models allow for non-Newtonian behavior in the low-quality regime (Cheng et al., 2000; CMG, 2015) but not in the high-quality regime. In the high-quality regime bubble size is controlled by a limiting capillary pressure (Khatib et al., 1988). This limiting capillary pressure corresponds to a limiting water saturation S_w^* . Since foam does not alter the liquid relative-permeability function, a stronger foam corresponds to lower limiting liquid saturation, S_w^* (Zhou and Rossen, 1995). Thus, non-Newtonian behavior in the high-quality regime requires that S_w^* be a function of water superficial velocity. If it depended on gas superficial velocity, the pressure-gradient contours in **Fig. 3.1** would not be vertical. In this study, however, for simplicity we assume that S_w^* is a function of total superficial velocity.

Surfactant-alternating-gas, or SAG, is the preferred method to inject foam into a reservoir for both operational and sweep-efficiency reasons (Blaker et al., 2002; Shan and Rossen, 2004). This method of injection offers, among other advantages, better injectivity than direct foam injection and a low-mobility shock front that displaces the fluids ahead of it while it propagates downstream. The shock is to a state a very low f_w , and thus is governed by the high-quality regime (**Figure 3.2**). Here for simplicity we focus on injection of the first gas slug. For the first gas slug, the initial condition I is 100% saturation of surfactant solution, and the injection condition J is at residual water saturation, S_{wr} . The path connecting I and J along the fractional flow-curve $f_w(S_w)$ does not have monotonically increasing slope df_w/dS_w ; therefore a portion of the trajectory is replaced by a discontinuity, or shock, from I to a

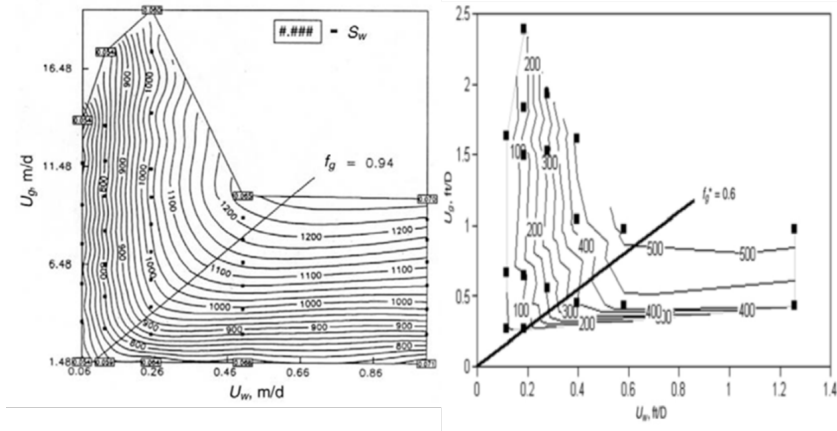


Figure 3.1: The two steady-state foam regimes. On the left, pressure difference across a 2-ft sandpack as a function of superficial velocities of water (U_w) and gas (U_g). In this case foam is shear-thinning in the high-quality (upper left) regime (Osterloh and Jante, 1992). On the right, pressure gradient as a function of superficial velocities in a coreflood study (Alvarez et al., 2001). This case is shear-thickening.

point of tangency to the $f_w(S_w)$ curve. Because of the abrupt foam collapse as a function of S_w near S_w^* (Khatib et al., 1988) the $f_w(S_w)$ curve is steep near S_w^* (Rossen and Zhou, 1995). This means the point of tangency is at low f_w , in the high-quality regime. An example is depicted in Figure 3.2.

A spreading wave forms behind the shock. The spreading wave is made of characteristics that travel with fixed saturation and velocity (for a Newtonian process). Figure 3.3 shows the dimensionless time-distance diagram of one SAG process. The shock (solid line) mobility has a fixed value, Behind it, the spreading wave contains many characteristics, with a continuous range of (fixed) mobilities. Figure 3.3 illustrates this for four characteristics (dotted lines).

The methodology described above has been shown to be more accurate than numerical simulation as long as the assumptions of fractional-flow theory apply (Rossen, 2013). In particular, the abrupt transition imposed by the limiting capillary pressure is difficult to model correctly using finite-difference methods without using an extremely refined grid near the wellbore Leefink et al. (2015). Boeije and Rossen (2015b) use the theory to derive an analytical formula to estimate the injectivity of the first gas slug in a SAG process. The formula predicts that, soon after injection begins, the pressure gradient across the foam bank is nearly constant as it advances.

A previous work on non-Newtonian foam displacements (Rossen et al., 2011) was limited to foam injection or gas injection in a SAG process behind the shock front,

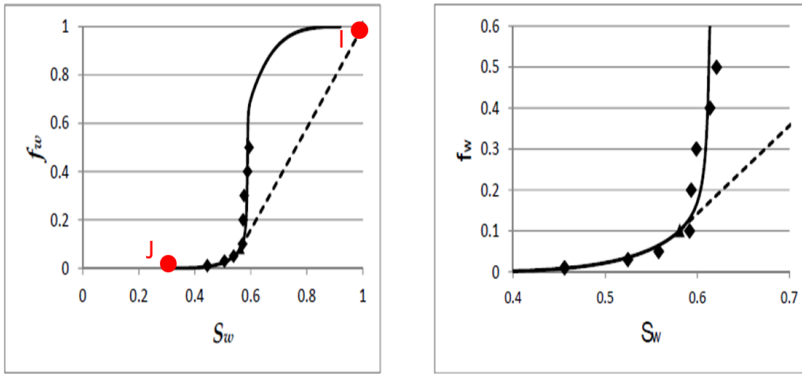


Figure 3.2: On the left, a fractional-flow curve adapted from Boeije and Rossen (2018). Black diamonds are coreflood data used to construct the fractional-flow curve. Red dots denote the initial (I) and injection (J) conditions. On the right, an expanded view of the same curve near the point of tangency defining the shock.

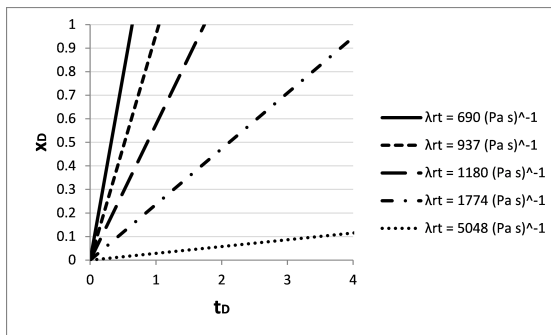


Figure 3.3: A dimensionless time-distance diagram (Rossen and Boeije, 2015). The mobilities of the shock and of a few of the characteristics are included.

and included only shear-thinning behavior. The SAG analysis showed the effect of changing gas saturation and non-Newtonian behavior in the near-well region after the shock passes out of this region. The study showed that shear-thinning behavior affects mobility near the well; this implies that the injectivity is better than that predicted by a Newtonian model.

In this study, we extend the previous work to include both shear-thinning and shear-thickening behavior, as observed in the laboratory (**Figure 3.1**). Equally important, we provide a methodology to solve issues that arise, e.g., when new characteristics emerge from the shock or when a characteristic and the shock collide. Finally, we show the consequences of non-Newtonian behavior for overall injectivity and mobility control at the leading edge of the foam bank.

3.2. FRACTIONAL-FLOW SOLUTIONS FOR GAS INJECTION IN NON-NEWTONIAN SAG PROCESSES

Consider a homogenous cylindrical reservoir that is initially fully saturated with surfactant solution. Starting at time zero, gas is injected at a fixed volumetric rate Q into the reservoir. In this situation the gas-injection process is governed by the high-quality regime, where foam strength depends on the limiting water saturation, S_w^* , named *fmdry* in the foam model described in Appendix A. Under these assumptions (including incompressible fluids), total superficial velocity u_t is a function of radial distance from the well.

In **Figure 3.1**, total mobility of foam is a power-law function of water superficial velocity, not total superficial velocity u_t . Here for simplicity, we assume that it is a power-law function of u_t . In the high-quality regime, $S_w \approx S_w^*$, i.e. *fmdry* in our model. For the purpose of deriving model parameters, consider injection of a foam at fixed water fractional flow but decreasing superficial velocity as foam moves further from the well. From the power-law equation (Bird et al., 2006),

$$\nabla p = C u_t^n \tag{3.4}$$

Applying Darcy's law to the water phase, with water saturation fixed at *fmdry*,

$$\nabla p = \frac{k k_{rw}(S_w = \textit{fmdry})}{\mu_w} f_w u_t \tag{3.5}$$

where n , C , ∇p , k , $k_{rw}(S_w)$ and μ_w denote, respectively, the power-law exponent, a constant, pressure gradient, permeability, liquid relative permeability and liquid viscosity. Combining these equations, one can show that the ratio $k_{rw}(S_w)/u_t^{n-1}$ is a constant, which in cylindrical flow can be rewritten as $k_{rw}(S_w)/r^{1-n}$. As next step, we apply this ratio to the outer radius r_e and at any other radius r . Finally, using a

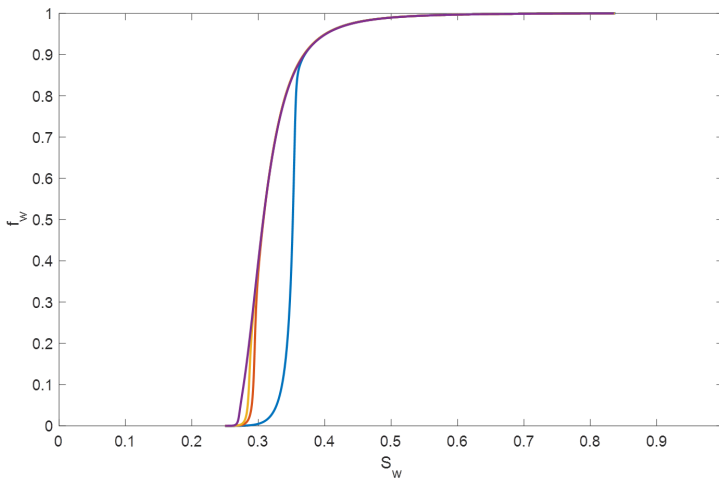


Figure 3.4: Fractional-flow curves for different radii for a shear-thinning foam with a power-law exponent of $n=0.33$. The parameter $fmdry$ varies from 0.356 at the wellbore radius ($r_w=0.1$ m) (blue curve) to 0.312 at $r = 1.0$ m (red), 0.286 at $r = 10$ m (yellow), and 0.271 at the outer radius ($r_e=100$ m) (purple).

Corey-Brooke model for k_{rw} (see **Appendix A**), we derive an expression for $fmdry$ as a function of r :

$$fmdry(r) = S_{wr} + (fmdry_e - S_{wr}) \left(\frac{r}{r_e} \right)^{\frac{n-1}{n_w}} \quad (3.6)$$

where $fmdry(r)$ denotes the water saturation at which foam collapses at a given radial position, S_{wr} is the irreducible water saturation, r radius, and n_w the Corey-Brooke exponent for $k_{rw}(S_w)$. The subscript e denotes a reference value, in our study taken at the outer radius. **Equation 3.6** indicates that for a shear-thinning foam the fractional-flow curve shifts to the left (smaller S_w) as the radius increases, while for a shear-thickening foam it shifts to the right. **Figures 3.4** and **3.5** illustrate this phenomenon for a shear-thinning foam with a power-law exponent of $n = 0.33$ and for a shear-thickening foam with an exponent $n = 1.34$, respectively. **Figures 3.4** and **3.5** reflect only non-Newtonian behavior in the high-quality regime, not in the low-quality regime, since it is the high-quality regime that dominates behavior during gas injection in a SAG process (**Figure 3.2**).

We discretize the reservoir domain in increments along x_D . Within each increment foam properties are assumed to be constant, i.e. Newtonian. Therefore, within each increment, the characteristics and the shock are straight lines. However, as each characteristic crosses to the next increment, its velocity changes. This continuous variation of velocity makes the characteristics curve on a large scale; **Figure 3.6** shows

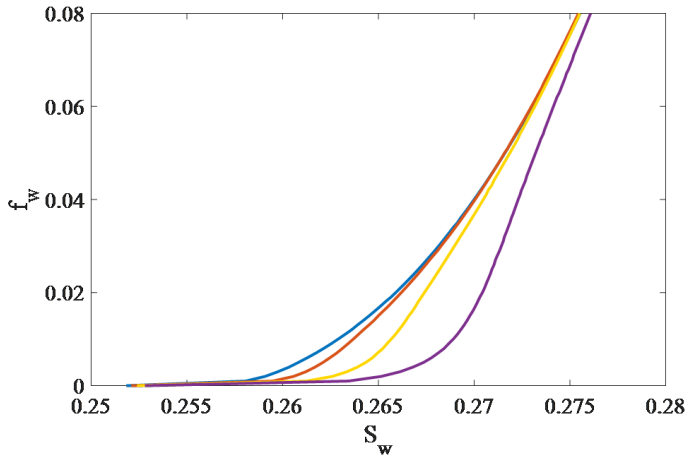


Figure 3.5: Fractional-flow curves for different radii for a shear-thickening foam ($n=1.34$), where f_w varies from 0.259 at $r_w=0.1$ m (blue curve) to 0.262 at $r = 1$ m (red), 0.266 at $r = 10$ m (yellow), and 0.271 at the outer radius $r_e = 100$ m (purple).

an example. **Figure 3.6** uses for illustration very large increments in $\Delta x_D = 0.1$; in our calculation the increments are much smaller. The approximation to continuous variation in properties becomes exact in the limit as the increment in x_D approaches zero.

A characteristic no longer carries its water-saturation value as it crosses between increments, but its water fractional-flow value instead (Rossen et al., 2011; Wu et al., 1993). The individual characteristics within the spreading wave do not collide with each other, because, at any value of x_D , velocity df_w/dS_w decreases monotonically with S_w . Thus individual characteristics spread further apart as they move downstream. Interactions with the shock are possible however.

We use the approach of Lake et al. (2003) to resolve the complications raised by the collision between a characteristic and a shock or by an accelerating shock that sheds additional characteristics.

Figure 3.7 illustrates this approach for a shear-thinning foam using, for illustration, a very large increment in x_D . Within the first increment (**Figure 3.7a**), starting at the wellbore, the fractional-flow curve is fixed and the Buckley-Leverett solution is the same as for a Newtonian SAG, i.e., a shock followed by a spreading wave. As the shock (point *A*) leaves the first increment and enters the second increment, conserving its value f_w (**Figure 3.7b**), it slows down as it displaces initial condition *I*. As the

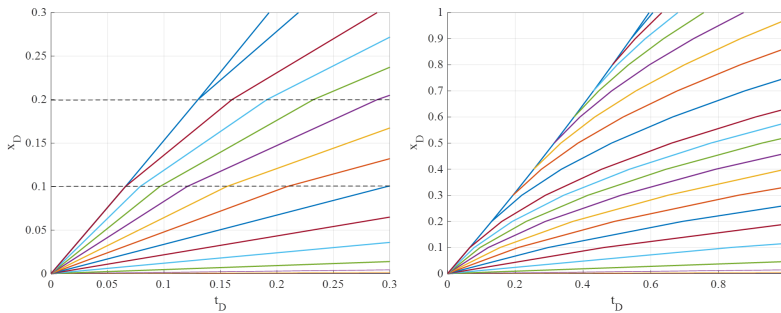


Figure 3.6: On the left, an augmented view of the dimensionless position (x_D) vs dimensionless time (t_D) diagram for a shear-thinning foam. The characteristics are straight lines within each increment in x_D . On the right, larger scale plot of the same diagram, showing how the characteristics curve.

characteristics behind the shock cross the boundary to the second increment their velocities increase. An example is that at characteristic B (denoted B' in the second increment), which accelerates greatly and rapidly intersects the shock. This collision imposes a new Buckley-Leverett problem with initial condition ($f_w = 1$) and injection condition B' . The solution is a new shock from $f_w = 1$ to B' ; see **Figure 3.7 c**. This new shock does not necessarily satisfy the tangency condition, though, if it does not, other characteristics behind it approach as well; further collisions are possible. Whenever this occurs we solve locally the arising Buckley-Leverett problem using the same methodology. **Figure 3.8** illustrate the collision of a characteristic and the shock in a dimensionless time-distance diagram. In our discrete approximation to the continuous variation in properties, the shock velocity is recalculated as it enters each new increment. When a collision occurs within an increment the characteristic that was the shock is eliminated, replaced by the characteristic that collides with (Ponners, 2017; Ter Haar, 2018).

We construct the fractional-flow solution for a shear-thickening foam by considering, again, two increments in x_D starting at the injection face. For a shear-thickening foam the first increment corresponds to a weaker foam, represented by the red fractional-flow curve in **Figure 3.9**. Within first increment, the solution is a shock from a point of tangency to point I at $f_w = 1$, followed by a spreading wave as in a Newtonian SAG; see **Figure 3.9a**. As the shock enters the next increment in x_D (**Figure 3.9b**) it imposes a new Buckley-Leverett problem with initial condition $f_w = 1$ and injection condition A' . The solution is a spreading wave from A' to a new point of tangency and an accelerated shock. The state previously immediately upstream of the shock is now a characteristic within the spreading wave; see **Figure 3.9c**. As the shock enters each new increment, additional characteristic(s) split off from it. **Figure 3.10** summarizes the fractional-flow solution on a dimensionless

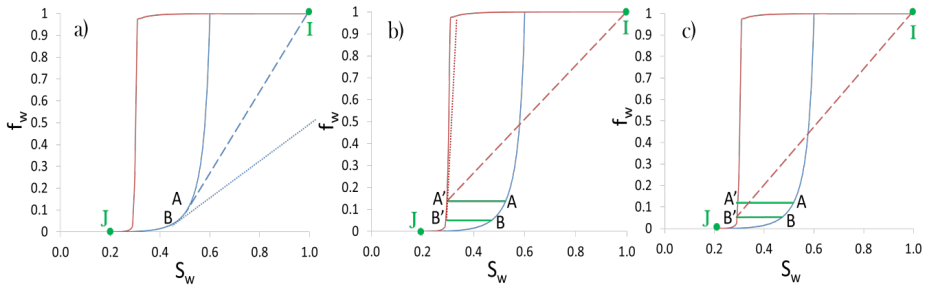


Figure 3.7: Schematic of fractional-flow solution for a shear-thinning foam. The dashed lines represent the shock and the dotted lines represent a characteristic. a) Shock and a characteristic for the first increment in x_D , at the wellbore. b) The shock and the characteristic in the second increment. Note that the shock velocity decreases while the velocity of the characteristic behind it increases with respect to the first increment. c) The collision between the characteristic and the shock results in a new shock and the disappearance of the characteristic that had formerly been the shock.

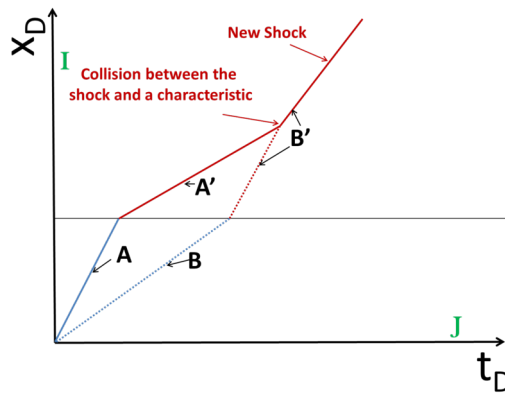


Figure 3.8: Dimensionless time-distance diagram illustrating collision of characteristic and shock in a shear-thinning foam; cf. **Figure 3.7**.

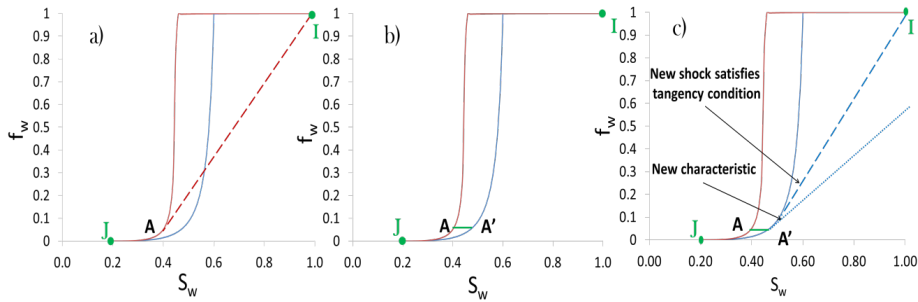


Figure 3.9: Fractional-flow solution for a shear-thickening foam. The dashed line represent the shock and the dotted line represents a new characteristic. a) A shock forms in the first increment. b) As the shock enters the next increment, it imposes a new fractional-flow problem in the second increment with initial condition, I , and with injection condition, A' . c) Solution of the fractional-flow problem in the second increment including an accelerated shock and a new characteristic.

time-distance diagram. Note that while collisions occur within increments for shear-thinning foam, additional characteristics are created at the boundaries between increments for shear-thickening foam (Ponners, 2017; Ter Haar, 2018).

We carry out the calculations as follows. We discretize x_D into 1000 increments, spaced so that total superficial velocity increases by 0.7% between consecutive increments. Thus increments are smaller near the wellbore, where total superficial velocity changes rapidly. For shear-thinning foam, we calculate velocities for 300 characteristics in the first increment. In each new increment moving outward, we calculate the intersection point between the shock and the characteristic immediately behind it. If the intersection is within the increment, we recalculate the new shock velocity and eliminate the characteristic from that point forward. We then check whether the next characteristic would then intersect the new shock trajectory within the increment; if so, we update shock velocity and eliminate the next characteristic, and so forth.

For shear-thickening foam, we calculate velocities for 300 characteristics in the outer increment. We carry out calculations moving inward; in essence working from Figure 3.9c to 3.9a at each new increment moving inward. At each new increment, we calculate the shock velocity using the tangency condition. Any characteristics with larger velocities are eliminated. In the example shown below, there are 169 characteristics left at the inner increment, so resolution is good throughout the domain of interest. For both shear-thinning and shear-thickening cases, results were substantially unchanged whether we started with 200 or 300 characteristics, or whether they were initially spaced equally in S_w or in f_w .

In the end, we have a table of dimensionless times at which each characteristic

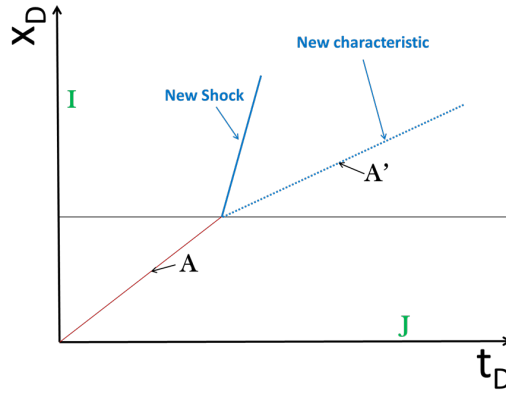


Figure 3.10: Dimensionless time-distance diagram corresponding to a shear-thickening foam. Dimensionless time-distance diagram corresponding to a shear-thickening foam.

passes the outer boundary of each increment in x_D , along with the values of f_w and S_w for that characteristic. From S_w the total mobility corresponding to that characteristic in that increment can be determined.

We compute the pressure difference between the wellbore and the outer radius by integrating $\nabla p(r)$ between r_w and r_e (Al Ayesh, 2016; Ponnens, 2017; Ter Haar, 2018). We define dimensionless pressure rise at the well P_D by dividing by the pressure difference needed to inject water into a fully liquid-saturated reservoir at the same rate Q . Assuming a water viscosity of 0.001 *Pas*,

$$P_D = \frac{\frac{Q}{2\pi kh} \int_{r_w}^{r_e} \frac{1}{\lambda_{rt}(S_w)} dr}{\frac{Q}{2\pi kh \lambda_w} \ln\left(\frac{r_e}{r_w}\right)} = \frac{\int_{r_w}^{r_e} \frac{1}{\lambda_{rt}(S_w)} dr}{\frac{1}{1000} \ln\left(\frac{r_e}{r_w}\right)} \quad (3.7)$$

Computing P_D requires converting the table of dimensionless times when characteristics and shocks pass boundaries between increments into a table of positions of characteristics within the various increments at a fixed time. We use linear interpolation to calculate the dimensionless positions of the shock and characteristics within the increments. Within each increment, between each pair of characteristics, we take the average of the mobilities of the two characteristics to determine the difference in pressure between the two. Then, the total relative mobility (λ_{rt}) as a function of x_D at a fixed t_D can be used to numerically solve the integral in **Equation 3.7** by summing up the increments between characteristics. In our final results we distinguish ΔP_f , the pressure difference across the foam bank, from ΔP_w , the pressure difference across the water-saturated region ahead of foam (region *I* in **Figures 3.8** and **3.10**). For a Newtonian foam, the pressure difference across the foam bank

Viscosities	
$\mu_w = 1 \times 10^{-3}$ Pa s	$\mu_g = 2 \times 10^{-5}$ Pa s
Corey-Brooke Relative-Permeability Parameters	
$S_{wr} = 0.25$	$S_{gr} = 0.20$
$k_{wr}^0 = 0.39$	$k_{gr}^0 = 0.59$
$n_w = 2.86$	$n_g = 0.7$
Foam Parameters at the outer radius r_e	
$fmdry = 0.271$	
$fmmob = 47700$	
$epdry = 400$	

Table 3.1: Summary of the input parameters used in this study Kapetas et al. (2017).

approaches a constant value soon after injection begins (Boeije and Rossen, 2015b).

3.3. APPLICATION

We apply the methodology described above to a homogeneous cylindrical reservoir with wellbore and open-outer-boundary radii of 0.1 m and 100 m, respectively. The superficial velocity varies by a factor of 1000 from the outer radius to the wellbore radius. Experimental data on the non-Newtonian behavior of foam in the high-quality regime extend over ranges very much smaller than this (cf. **Figure 3.1**); thus our results illustrate the implications if these trends continue over a much-wider range of velocities. We describe the computer programs used in this study in **Appendix E**.

The STARS foam model is able to reproduce an abrupt, though not complete, foam collapse at a water-saturation value $fmdry(S_w^*)$ (Cheng et al., 2000; CMG, 2015). However, this version of the dry-out function can underestimate the injectivity observed in the field during gas injection in a SAG (Rossen et al., 2017). Therefore, in this study we use the Namdar-Zanganeh modification of this model, which assumes complete foam collapse at residual water saturation S_{wr} (Namdar Zanganeh et al., 2014; Rossen et al., 2017). See **Appendix A** for a description of the foam model used in this study.

With the exception of $fmdry$, all rheological and petrophysical properties are constant (**Table 3.1**). As the base case, we use the $fmdry$ value determined by Kapetas et al. (2017) for Bentheimer sandstone and apply it to the outer radius ($r_e = 100$ m). At other radial positions, $fmdry$ is given by **Equation 3.6**. The experimental data of Kapetas reflect a very strong foam, with very low mobility.

We apply the power-law exponents reported by Alvarez et al. (2001) ($n = 1.34$)

and by Osterloh and Jante (1992) ($n = 0.33$) to the entire range of velocities. As noted, these trends were determined experimentally over a much-narrower range of velocities than assumed here. Our results illustrate the implications if those trends continue over the entire range of velocities around an injection well.

3.4. RESULTS

3.4.1. SHEAR-THINNING FOAM ($N=0.33$)

For the shear-thinning case we use the exponent $n = 0.33$ from the data of Osterloh and Jante (1992). **Figure 3.11** depicts the resulting dimensionless time-distance diagram using our methodology. The characteristics accelerate with increasing dimensionless distance, while the shock slows down.

Figure 3.12 plots total relative mobility as a function of dimensionless position for $t_D = 0.5$. As expected, there is an abrupt transition in mobility at the shock. This drop in mobility offers good mobility control at the leading edge of the foam bank. Moving back toward the well, mobility increases, which helps gas injectivity. These advantages are also observed with a Newtonian foam.

Figure 3.13 plots water saturation behind the shock as a function of $fmdry$, as the shock advances from the wellbore to the outer radius. Also plotted is the water saturation satisfying the conventional tangency condition for the same values of $fmdry$. At the wellbore, the initial shock is determined by the tangency condition, but the two deviate as the shock advances. In addition, the mobility at the shock need not match exactly the power-law function observed for fixed-quality (fixed- f_w) injection in **Figure 3.1**, used to construct our model parameters (**Equation 3.6**). The mobility at fixed f_w in the high-quality regime depends primarily on $fmdry$, but the tangency condition in a SAG process is sensitive to other factors as well. **Figure 3.14** shows total relative mobility at the shock as a function of dimensionless position. Also plotted is the mobility that would be computed from the tangency condition at each position. The mobility at the shock decreases as the shock advances, but not in exact agreement with the tangency condition.

Figure 3.15 shows total dimensionless pressure rise at the well (P_D) during injection of the first pore volume of gas for this shear-thinning foam. The magnitude of pressure rise is very large, which reflects the extremely strong foam found by Kapetas et al. in their corefloods. We believe the trends here would also be reflected in weaker foams applied in the field. Total dimensionless pressure increases up to foam breakthrough, in contrast to a Newtonian SAG process. For comparison, **Figure 3.15** shows also P_D for two Newtonian foams, applying properties at the outer and wellbore radii, i.e. $fmdry = 0.356$ and 0.271 , throughout the displacement, The injectivity of the

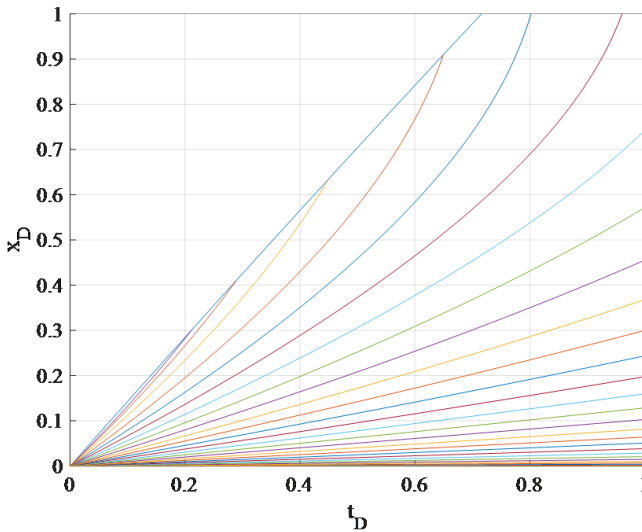


Figure 3.11: Dimensionless time-distance diagram for the shear-thinning foam with a power-law exponent $n = 0.33$. Note that some characteristics collide with the shock. For illustration purposes we plot only 50 characteristics.

shear-thinning foam lies between the injectivity corresponding to the two limiting (Newtonian) cases .

These results illustrate two general trends for gas injection in SAG with shear-thinning foam: mobility control at the foam front improves as foam advances from the well, but injectivity declines. The mobility at the shock is consistently less than that estimated from the tangency condition for the $f_w(S_w)$ function starting at a radius, $r = 0.13$ m. Mobility at the shock decreases by about a factor of 0.03, instead of $(1000)^{-0.77} \approx 0.01$ suggested by the power law.

3.4.2. SHEAR-THICKENING FOAM ($N=1.34$)

Figure 3.16 presents the dimensionless time-distance diagram for a shear-thickening foam with power-law exponent of 1.34; this is one of the estimates reported by Alvarez et al. (2001) based on coreflood data. The characteristics slow down as they advance, and new characteristics appear at the shock, which accelerates. **Figure 3.17** shows total relative mobility at the shock as it advances; in this case it everywhere satisfies the tangency condition. The increase in mobility at the shock, however, is much less than suggested by the power-law exponent at fixed f_w . Mobility increase by about a factor of 3.3, instead of $(1000)^{0.34} \approx 10.5$ suggested by the power law. This discrepancy is explained by the fact that the shock satisfies the tangency condition at

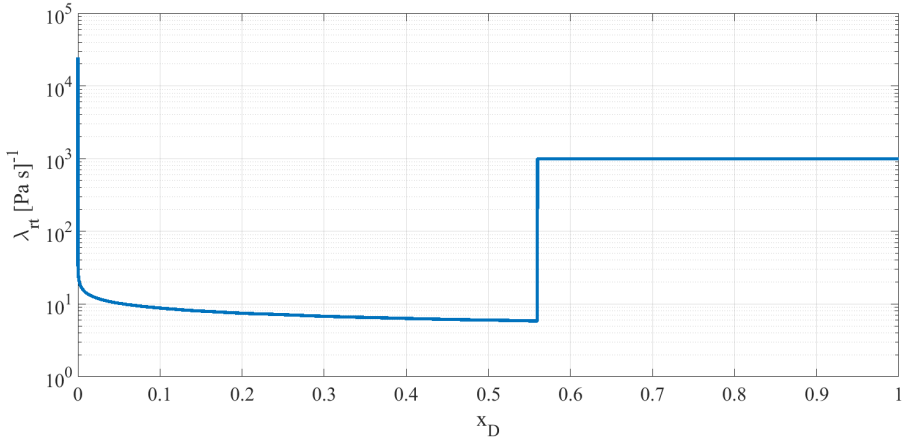


Figure 3.12: Total relative mobility (λ_{rt}) as a function of dimensionless position (x_D) at a fixed dimensionless time ($t_D = 0.5$) for a non-Newtonian foam with power-law exponent n equal to 0.33.

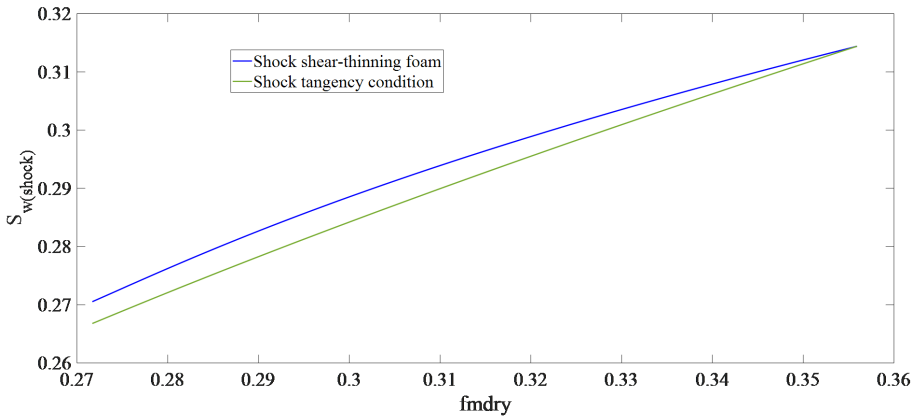


Figure 3.13: Water saturation behind the shock plotted as a function of $fmdry$, as both change with radial position, for shear-thinning foam with power-law exponent n equal to 0.33. The blue curve shows the water saturation behind the shock for the shear-thinning foam and the green curve shows the saturation for the shock calculated with the tangency condition for a fractional-flow curve at the same dimensionless position.

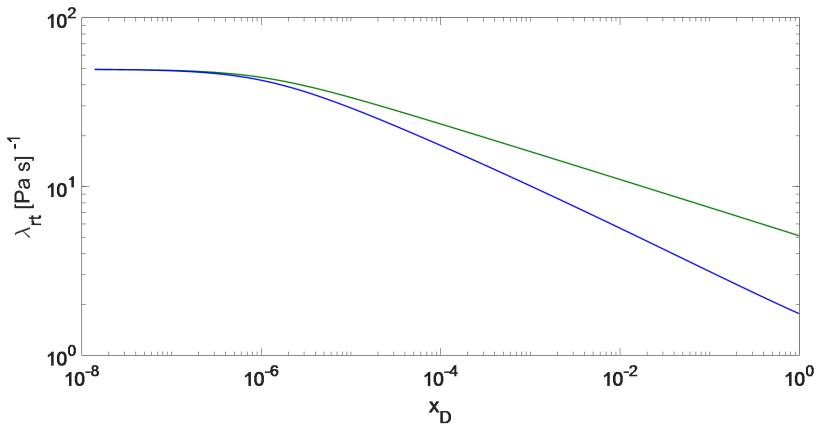


Figure 3.14: Total relative mobility behind the shock (blue curve) as a function of dimensionless position for a shear-thinning foam with power-law exponent n equal to 0.33. The green curve shows total relative mobility for the corresponding positions calculated from the tangency condition.

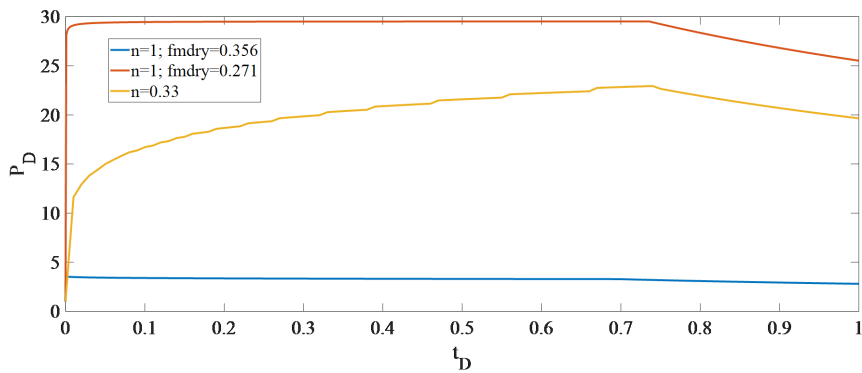


Figure 3.15: Dimensionless pressure rise (P_D) as a function of dimensionless time (t_D) for a shear-thinning foam with power law exponent n equal to 0.33.

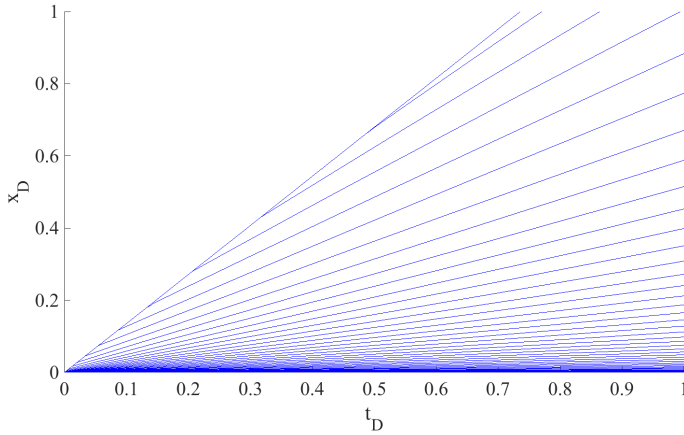


Figure 3.16: Dimensionless time-distance diagram for a shear-thickening foam with a power-law exponent (n) of 1.34. For illustration purposes we plot only 50 characteristics.

each increment and therefore no longer carries a unique f_w value.

Figure 3.17 plots dimensionless pressure rise at the well (P_D) as a function of dimensionless time. The maximum dimensionless pressure occurs near the start of gas injection, with value of P_D approximately equal to 48. As gas injection progresses, the dimensionless pressure drops to 34.7 before the shock breaks through. Thereafter, it decreases at an even faster rate. As the dimensionless pressure declines far from the injection well, the mobility control offered by the foam bank suffers. As in shear-thinning SAG, the shear-thickening case lies between the two non-Newtonian limiting cases (based on mobility at r_w and at r_e). However, in contrast to a shear-thinning foam, the strongest foam, with $fmdry = 0.259$, is located in the near-wellbore region.

We also modeled a shear-thickening foam with $n = 1.67$, another value reported by Alvarez et al. (2001). As seen in **Figure 3.17**, for $n = 1.34$ $fmdry$ approaches S_{wr} near the wellbore. For $n = 1.67$, and assuming a strong foam at r_e , $fmdry$ approaches so close to S_{wr} near the wellbore that the adjustment of Namdar Zanganeh, which requires foam collapse at S_{wr} , gives shear-thinning behavior very near the well. Therefore we do not show that case. Details are in Ter Haar (2018).

3.4.3. FINITE-DIFFERENCE SIMULATION

In this chapter we present the evolution of total dimensionless pressure for non-Newtonian SAG processes during gas injection, calculated using a finite-difference

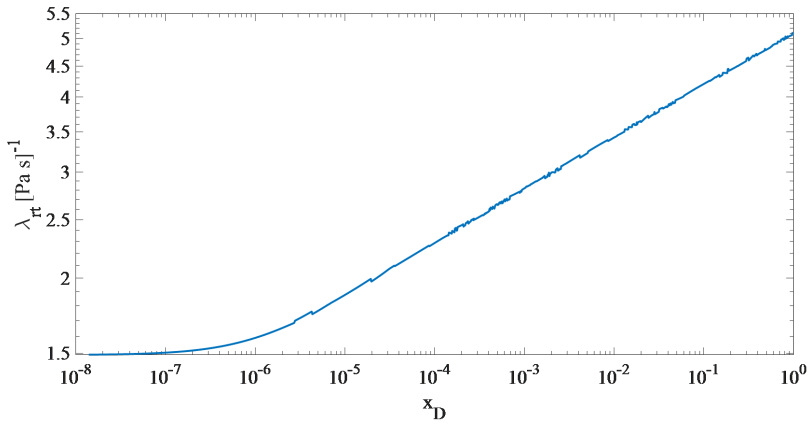


Figure 3.17: Total relative mobility at shock as function of dimensionless position for a shear-thickening foam with power-law exponent $n = 1.34$.

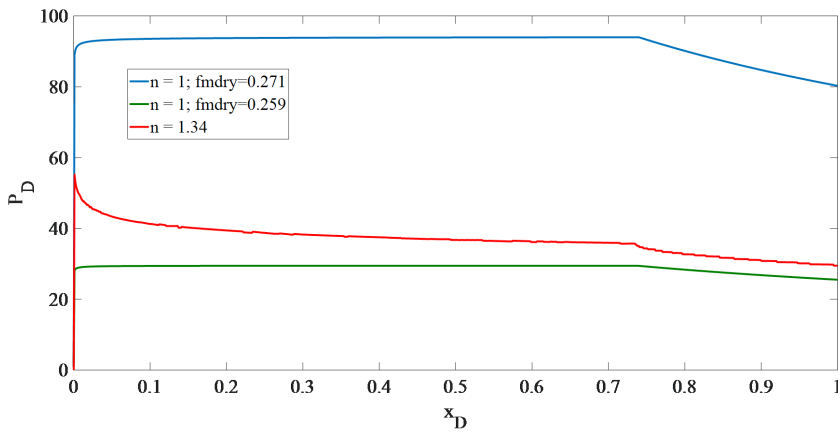


Figure 3.18: Total dimensionless pressure (P_D) as a function of dimensionless time (t_D) for the Newtonian foams that apply at the wellbore radius (on the left, $fmdry = 0.259$) and at the outer radius (on the right, $fmdry = 0.271$).

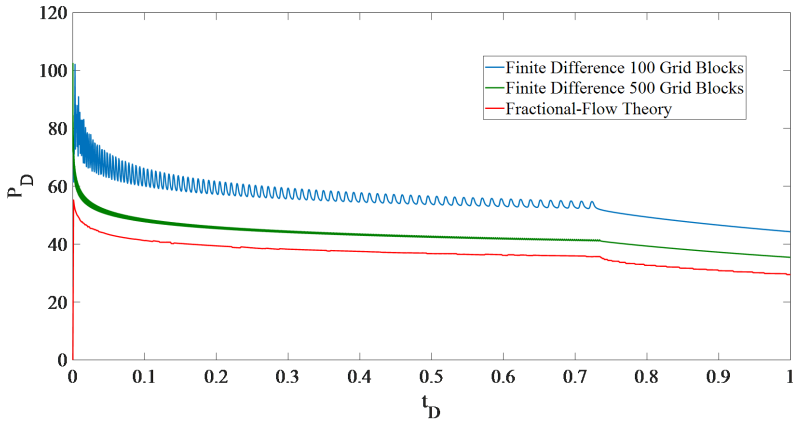


Figure 3.19: Effect of grid-block resolution on calculated injectivity using finite-difference simulation. In blue, the dimensionless pressure evolution calculated using 100 grid blocks, for a foam with power-law exponent $n = 1.34$. In green, using 500 grid blocks, for the same foam parameters; in red fractional-flow calculation.

simulator. A description of the discretization scheme used in the simulator is included in **Appendix B**; see also Bos (2017). The input parameters correspond to the petrophysical and foam parameters listed in **Table 3.1**.

Figure 3.19 shows total dimensionless pressure calculated using 100 and 500 grid blocks in radial geometry, linearly spaced in r , for shear-thickening foam with $n = 1.34$. With 500 grid blocks, the first block extends from the wellbore at 10 cm to 30 cm. The fluctuations in **Figure 3.19** reflect the movement of the shock through consecutive grid blocks (Rossen, 2013). Qualitatively, the behavior resembles the fractional-flow results: injection pressure increases until foam breaks through. However, even with this extraordinary grid resolution, the injectivity calculated by the finite-difference simulator is in significant error.

3.5. CONCLUSIONS

We present a method of solution for initial gas injection in a non-Newtonian SAG process that includes the interactions between the shock and the characteristics. The methodology can be applied to both shear-thinning and shear-thickening behavior.

For a shear-thinning foam, we find that mobility control improves as the foam front propagates from the well, but injectivity declines somewhat with time. However, the injectivity is still more favorable than for a Newtonian foam with the same

mobility at the outer radius. In case of a foam with marginal mobility control, there could be problems with viscous fingering as foam initially advances from the near-well region. For a shear-thinning foam, the shock does not necessarily satisfy the conventional tangency condition that applies to Newtonian foam, though it does continually approach it. In addition, the mobility at the front need not fit the power-law behavior seen at fixed gas fraction in the laboratory.

For a shear-thickening foam, mobility control deteriorates as the foam front advances, though injectivity improves somewhat with dimensionless time. However, injectivity is less favorable than for a Newtonian foam with the same mobility far from the well. In case of marginal mobility control, the foam could have problems with viscous fingering far from injection well.

Overall, injectivity is a complex result of changing saturations and varying superficial velocities in the direct vicinity of the well. Conventional simulators cannot adequately represent these effects, or estimate injectivity accurately, in the absence of exceptional grid resolution near the injection well.

4

SCALE-UP OF LABORATORY DATA FOR SINGLE-SLUG SURFACTANT-ALTERNATING-GAS FOAM FOR ENHANCED-OIL-RECOVERY

Foam increases sweep efficiency during gas injection in enhanced oil recovery (EOR) processes. Surfactant Alternating Gas, or SAG, is the preferred method to inject foam for both operational and injectivity reasons. Dynamic SAG corefloods are unreliable for direct scale-up to the field because of core-scale artifacts. In this study we scale-up local-equilibrium (LE) data measured at very low injected liquid fractions in a Bentheimer core for different surfactant concentrations and total superficial velocities.

We fit LE data to an Implicit-Texture foam model for scale-up to a dynamic foam process on the field scale using fractional-flow theory. We apply different parameter-fitting methods (least-squares fit to entire foam-quality scan and the method of Rossen and Boeije (2015)) and compare their fits to data and predictions for scale-up. We also test the implications of complete foam collapse at irreducible water saturation for injectivity.

Each set of data predicts a shock front with sufficient mobility control at the leading edge of the foam bank. Mobility control improves with increasing surfactant concen-

tration. In every case scaled-up injectivity is much better than with co-injection of gas and liquid. The results illustrate also how the foam model without the constraint of foam collapse at irreducible water saturation (Namdar Zanganeh et al., 2014) can greatly underestimate injectivity for strong foams.

For the first time we examine how the method of fitting the parameters to coreflood data affects the resulting scale-up to field behaviour. The method of Rossen and Boeije (2015) does not give a unique parameter fit, but the predicted mobility at the foam front is roughly the same in all cases. Predicted injectivity does vary somewhat among the parameter fits, however. Gas injection in a SAG process depends especially on behavior at low injected water fraction and whether foam collapses at the irreducible water saturation, which may not be apparent from a conventional scan of foam mobility as a function of gas fraction in the injected foam. In two of the five of cases examined this method of fitting the whole scan gives a poor fit for the shock in gas injection in SAG. We also test the sensitivity of the scale-up to the $k_{rw}(S_w)$ function assumed in the fit to data.

4.1. INTRODUCTION

After primary production of oil, gas may be injected into the reservoir. Under ideal conditions, gas is able to displace virtually all of the remaining oil, as long as the injected gas contacts the residing oil (Lake et al., 2014). However, geological heterogeneity and gravity segregation cause gas to migrate to high-permeability layers and to the top of the reservoir. Low gas viscosity compounds these effects. Foam is able to divert flow from high-permeability layers to low-permeability layers (Rossen, 1996; Schramm, 1994). Foam is able to reduce gravity segregation by reducing gas mobility. These combined properties increase gas's sweep efficiency and result in an attractive enhanced-oil-recovery method.

For operational and sweep-efficiency reasons, the best method of injection of foam is usually a Surfactant-Alternating-Gas process, or SAG (also called FAWAG) (Heller, 1994; Matthews, 1989; Shan and Rossen, 2004). During a SAG process foam is formed away from the injection well, thus offering better injectivity than a co-injection process (Al Ayesh et al., 2017). Also, SAG is uniquely suited to overcoming gravity override (Boeije and Rossen, 2015b; Kloet et al., 2009; Velde Harsenhorst et al., 2014).

Scaling-up laboratory results to the field scale remains a challenge (Rossen and Boeije, 2015). One approach involves dynamic coreflood experiments, where gas is injected into a fully surfactant-saturated core. These experiments often do not reach local equilibrium (LE) during the injection of the first pore volume of gas (Kapetas et al., 2014). This failure to reach LE on the laboratory scale can greatly distort the

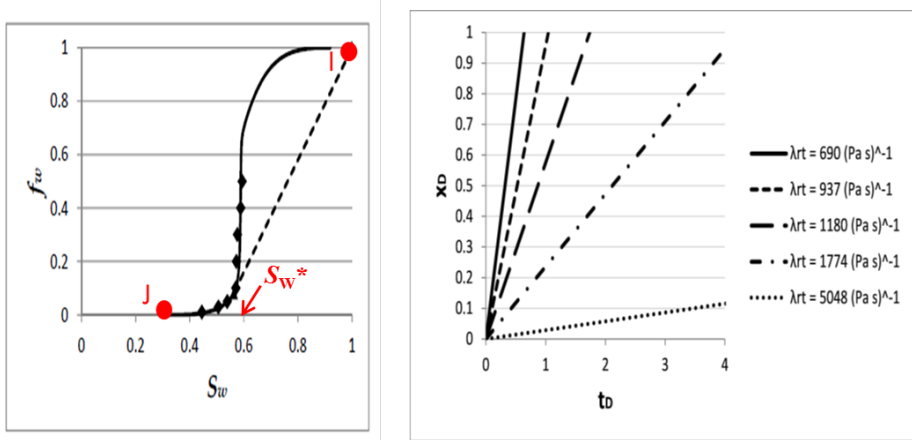


Figure 4.1: On the left, a fractional-flow curve adapted from Boeije and Rossen (2018). The red dots denote the initial (I) and injection (J) conditions for injection of the first gas slug. On the right, the dimensionless time-distance diagram for the corresponding gas-injection process. The mobilities of the shock, solid line, and four of the characteristics, represented as dotted lines, are included.

interpretation of the data in terms of LE foam models. Other effects, such as the entrance region and dispersion, could also distort laboratory-scale experiments.

At the field scale, foam models generally assume that local equilibrium applies. Therefore, steady-state corefloods are a feasible alternative approach to dynamic experiments. According to fractional-flow theory, during gas injection in SAG, the mobility of the foam bank depends on the fractional-flow curve $f_w(S_w)$ at extremely low liquid fraction f_w (Shan and Rossen, 2004; Zhou and Rossen, 1995). In consequence, some studies have aimed to upscale a gas-injection process during a SAG by focusing on steady-state experiments in this region of the $f_w(S_w)$ curve (Boeije and Rossen, 2018; Kibodeaux and Rossen, 1997; Xu and Rossen, 2004).

Figure 4.1 depicts a gas-injection process, specifically injection of the first gas slug into a surfactant-saturated reservoir. The initial, I , and injection, J , conditions correspond to water saturation $S_w = 1$ and water fractional flow $f_w = 0$, respectively. Note that the abrupt increase in foam mobility at a distinctive water saturation, S_w^* , imposed by the limiting capillary pressure (Khatib et al., 1988), results in a steep fractional-flow curve $f_w(S_w)$ near S_w^* Zhou and Rossen (1995). The resulting fractional-flow curve does not have a path from I to J with monotonically increasing slope df_w/dS_w . Therefore, the portion of the path connecting I to a point of tangency must be replaced by a shock or discontinuity. After the shock a spreading wave connects the point of tangency and J .

The dimensionless time-distance diagram for the injection of the first gas slug in SAG is illustrated on the right of **Figure 4.1**. The mobilities of the shock and of the characteristics continuously increase as one approaches the injection well at dimensionless position $x_D = 0$, at any given dimensionless time, t_D . The mobility at the shock is crucial to maintaining viscous stability during the foam displacement. Only relatively low mobility behind the shock can provide a stable front.

Another complication in laboratory foam corefloods is the capillary end effect at the core outlet, where foam generation occurs because of a higher water saturation there (Ransohoff and Radke, 1988). Experimental studies (Apaydin and Kovscek, 2001; Nguyen et al., 2003; Simjoo and Zitha, 2015) have reported an eruption of a much stronger foam at the core outlet and subsequent, slow upstream propagation of a stronger foam state. Apaydin and Kovscek (2001) observed this behaviour at relatively high surfactant concentrations. They claim it is initiated by the capillary end effect, and upstream propagation of the foam front reflects greater gas trapping just upstream of the foam. However, the mechanism for this increased trapping is not specified. Moreover, estimation of gas trapping in coreflood experiments (Nguyen et al., 2009) is difficult. Thus, there is still no complete explanation for the upstream propagation of this stronger foam state. Nevertheless, the eruption of a much stronger foam depends on behaviour near the core outlet; its relevance to a foam process in a homogenous reservoir at the field scale is unclear, and its implications to heterogeneous reservoirs are not yet established.

Several previous studies have found fractional-flow curves $f_w(S_w)$ that are non-monotonic in S_w . **Figure 4.2** illustrates how in these cases the fractional-flow curve, $f_w(S_w)$, shifts to higher S_w as f_w decreases. Then S_w decreases again upon further decrease in f_w . In fact, about half of the published examples from laboratory LE studies are not monotonic (Boeije and Rossen, 2018; Kibodeaux and Rossen, 1997; Wassmuth et al., 2001; Xu and Rossen, 2004). Rossen and Bruining (2007) show that this behaviour, scaled-up to the field, indicates a shock to complete foam collapse and therefore failure of mobility control at the leading edge of the foam bank, as illustrated in **Figure 4.2**.

In this paper we present a variety of data sets that follow the monotonic pattern, as in **Figure 4.1**. Each data set consists of a foam scan, i.e. foam mobility as a function of fractional flow, f_w . From foam mobility we estimate water saturation assuming a water relative-permeability function $k_{rw}(S_w)$. We examine the effects of surfactant concentration and total superficial velocity on the fractional-flow curve $f_w(S_w)$. We fit the data to foam-model parameters using the conventional method of a least-squares fit to the entire foam scan (Eftekhari and Farajzadeh, 2017; Kapetas et al., 2017) and the method of Rossen and Boeije (2015) for a SAG, which focuses in fitting the data in the low range of f_w . We do the scale-up with the parameters

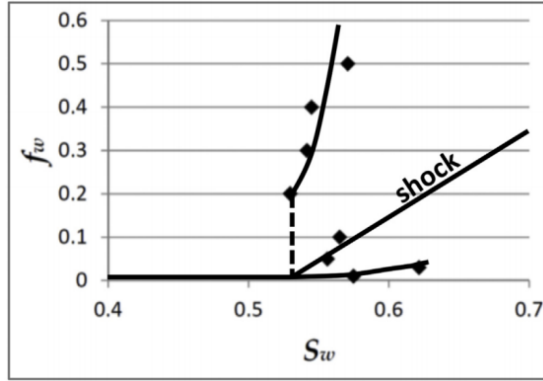


Figure 4.2: Shock construction for the injection of the first gas slug in a SAG for a multivalued fractional-flow curve (Boeije and Rossen, 2018)

4

determined from the model fits and calculate the mobility at the shock for a hypothetical field application. The method of Rossen and Boeije (2015) does not guarantee a unique parameter fit. We present a range of possible reasonable fits to the data using this method and indicate the corresponding range of differences in the scale-up. We compare the mobilities at the shock predicted by both fitting methods and illustrate how the injection strategy impacts the most suitable fitting method. We test the impact of complete foam collapse at the residual water saturation on the obtained parameters and on the injectivity by incorporating the Namdar Zanganeh et al. (2014). Finally, we test the sensitivity of the fit to the $k_{rw}(S_w)$ function assumed on the upscaled behavior for one of our experiments.

In **Chapter 5** we examine cases where we see non-monotonic behavior, as depicted in **Figure 4.2**. In that chapter we discuss what characterizes those cases and whether they reflect a laboratory artifact or would scale up to failure in the field. In this study we do not address liquid injectivity in SAG, except as it may be affected by foam collapse during injection of gas. Gong et al. (2019b) discuss the effect of gas injection on subsequent liquid injectivity.

4.2. EXPERIMENTAL APPARATUS

We conducted coreflood experiments in two setups, *A* and *B*. Apparatus *A*, depicted in **Figure 4.3**, is able to co-inject gas (N_2) and surfactant solution over a range of total superficial velocities between 0.82 and 16 ft/day. We injected the liquid phase using a Vindum pump model VP1, which is able to deliver a minimum flow rate accurately as low as 1×10^{-4} mL/min. To inject the gas phase we used a Bronkhorst gas mass-flow controller Model F-033CI which, in combination with a Coriolis flow me-

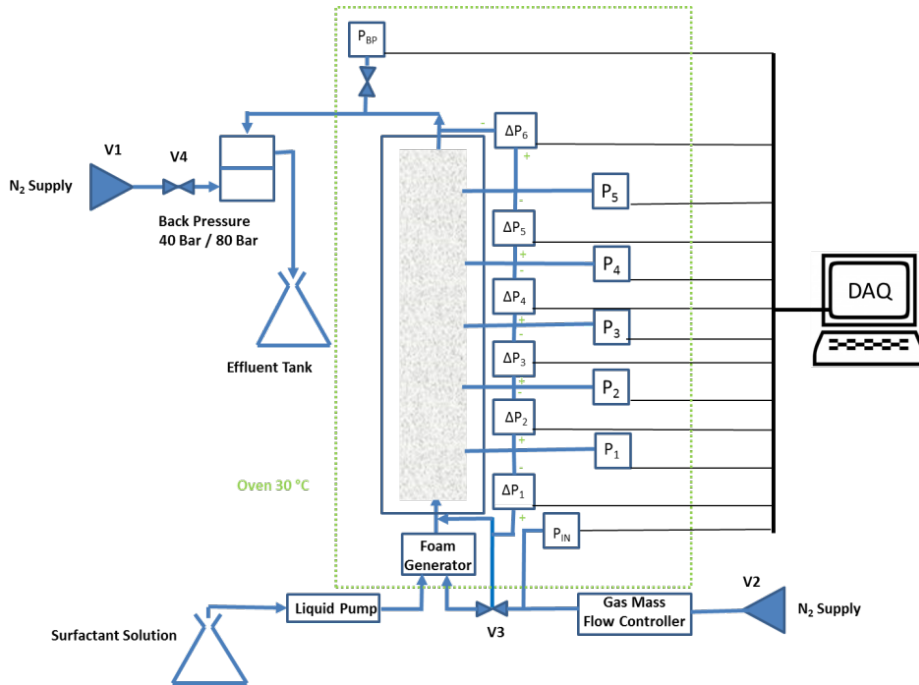


Figure 4.3: Experimental apparatus *A*, with controlled temperature. Apparatus *B* is substantially similar, with changes noted in the text.

ter, is able to deliver a flow rate between 1.2 and 60 g/h. A glued core is placed into a PEEK (polyether ether ketone) core holder with a narrow liquid-filled gap in between, pressurized to the injection pressure. We placed the core holder vertically and we injected the fluids from bottom to top. To help achieve steady-state, in some cases we used a foam generator upstream of the core inlet: a PEEK three-way-connector with a built-in micrometric filter. In order to reduce gas expansion along the core, a back-pressure regulator fixed at either 40 or 80 bar was placed at the outlet of the core. Seven absolute- pressure transducers and six differential- pressure transducers were connected using lines filled with liquid, connected to the core, to monitor gas expansion and foam mobility along the core. The setup was placed inside an oven maintained at 30°C. Apparatus *B* is an adaptation of apparatus *A* to fit in a CT-scanner in order to monitor water saturation during corefloods. The core holder was placed horizontally in the CT-scanner. PEEK lines replaced the metal lines connected to the core holder to reduce the X-ray attenuation. In both setups we digitally recorded the pressure and temperature data every 1.7 s using a program coded in *Labview*.

4.3. MATERIALS

During the coreflood experiments we co-injected nitrogen and surfactant solution to generate foam. The nitrogen was supplied by a 200-bar cylinder with a purity of 99.98%. We prepared surfactant solutions that consisted of a synthetic brine prepared with demineralized water, 1.0 wt.% sodium chloride, and anionic AOS surfactant (Stepan BIO-TERGE AS-40). We prepared four formulations with surfactant concentrations, C_S , of 0.037 wt.%, 0.1 wt.%, 0.5 wt.% and 1.0 wt.%, respectively. To clean the core between experiments we used a solution of 50 vol.% tap water and 50 vol.% isopropyl alcohol. The alcohol purity was 99.7%. We used two cylindrical Bentheimer cores cut from the same outcrop. The length of the cores was 38 cm and diameter 3.8 cm. The measured average permeabilities were 2300 md and 2100 md, respectively. We measured an average porosity of 0.226 for the second core using the CT-scanner.

4

4.4. EXPERIMENTAL PROCEDURE

Before each experiment we injected 10 PV of CO_2 to displace any gas inside the core. Next we injected at least 10 PV of brine at elevated pressure (80 bars) to dissolve any CO_2 that remained in the core. Then we measured the liquid permeability of the core. Finally, we injected 10 PV of surfactant solution to satisfy adsorption.

During each experiment we performed several foam-quality scans. Foam quality is gas fractional flow, i.e. $(1 - f_w)$. A foam scan is a series of steady-state measurements at different values of f_w and fixed total superficial velocity, u_t . Since our goal is to upscale a gas-injection process in SAG, we focus on data at low f_w . In most experiments we infer water saturation S_w from measured mobility using an estimated water-relative-permeability function $k_{rw}(S_w)$ for Bentheimer sandstone, as discussed below. In one foam scan we monitored S_w using a medical CT-scanner.

At the end of each foam scan we cleaned the core as follows, following a procedure similar to that used by Eftekhari and Farajzadeh (2017) and Kahrobaei et al. (2017) on shorter cores. First, we injected 10 PV of a 50/50 water/isopropyl alcohol solution at elevated pressure (80 bar) to kill foam. Second, we injected 10 PV of water initially at elevated (80 bar) back-pressure, and we reduced pressure slowly to atmospheric in order to allow the expansion of trapped gas. Third, we injected 10 PV of CO_2 followed by an additional 10 PV of water at atmospheric pressure. Fourth, we flushed the core again with 20 PV of water while gradually raising the back-pressure until its value reached 80 bar. Then we gradually reduced pressure to atmospheric. Fifth, we vacuum-cleaned the core, followed by the injection of at least 10 PV of CO_2 . Finally, we performed the preparation procedure described above and verified that the core had been restored to its initial permeability.

In our experiments we obtained monotonic fractional-flow curves $f_w(S_w)$ in two cases. First, we measured steady-state behavior when a second front of a much stronger foam did not erupt at the core outlet and subsequently propagate upstream. Second, in cases where such an eruption occurred, we used a foam generator and measured foam mobility in the core behind the foam front before gas breakthrough and eruption of the stronger foam state. In these cases we verified that foam behind the first foam front was at local equilibrium by comparing pressure data from multiple segments along the core. In agreement with Apaydin and Kavscek (2001), we did not observe this eruption of stronger foam at the outlet in experiments with a relatively low surfactant concentration (0.037 wt.%). To avoid hysteresis, during a foam scan we varied foam quality randomly while maintaining a fixed total superficial velocity.

4.5. FOAM MODEL

Foam rheology in porous media can be represented using either “Implicit Texture” (IT) or “Population Balance” (PB) models. PB models represent foam texture explicitly by dynamic simulation of bubble size (Kam et al., 2007; Kavscek et al., 2010). Gas mobility is then calculated as a function of bubble size. This approach is essential in cases where a foam-generation process is in question or is the object of study. IT models represent foam rheology using a mobility-reduction factor (Cheng et al., 2000). Both models represent local equilibrium in a SAG accurately. However, there have been only a few attempts to represent SAG processes with a PB model (Kavscek et al., 1995). Therefore, in this study we chose the STARS foam model (CMG, 2015), a widely used IT model (see description in **Appendix A**). This model predicts relatively strong foam even at irreducible water saturation, S_{wr} . However, a strong foam at irreducible water saturation might not represent long-term foam behavior at the field scale (Gong et al., 2019b; Rossen et al., 2017). Therefore in this study we also apply the modification of Namdar Zanganeh et al. (2014) that gives complete foam collapse at S_{wr} .

During gas injection in a SAG our interest is to describe foam behavior at low f_w . Therefore, we focus on the function(s) that describe foam collapse at low f_w : in this case, the dry-out function in the STARS foam model. However, there are cases where the data range includes experimental data at higher f_w , i.e. in both the low-quality and high-quality foam regimes (Alvarez et al., 2001). In order to obtain a correct fit at low f_w in these cases one must include functions that describe non-Newtonian behaviour in the low-quality regime. The details about these functions are in **Appendix A**.

4.6. MODEL-FITTING

We start by assuming that a single $k_{rw}(S_w)$ function applies in a given core even in the presence of foam. Eftekhari and Farajzadeh (2017) found that the effect of foam on the $k_{rw}(S_w)$ function for relatively high capillary numbers is not pronounced and can be ignored. They obtained a single $k_{rw}(S_w)$ fit for a set of data with measurements of pressure gradient and water saturation, in the absence and in the presence of foam. We describe the parameters of this $k_{rw}(S_w)$ function in detail in **Appendix A**. They used a Bentheimer core with a permeability of 2410 mD, which is similar to that measured in our own experiments. They employed two different surfactants and varied the value of C_S for one of these surfactants (AOS). They varied C_S in a similar manner as we do in this study.

4

We test if this function correctly estimates S_w data measured with the CT scanner in our own experiments. To that end, we performed a foam scan while measuring water saturation using a CT-Scanner. We performed this foam scan at a total superficial velocity of 4.25 ft/day (1.47×10^{-5} m/s) with $C_S = 0.5$ wt.%. The blue curves in **Figure 4.4** illustrate the fractional-flow data as a function of water saturation $f_w(S_w)$ in two sections of the core at steady state. In this case, we report the measured water saturation with the CT scanner. The red curves in **Figure 4.4** illustrate $f_w(S_w)$ data for the same foam scan. In this case we inferred water saturation using the $k_{rw}(S_w)$ function for a Bentheimer core reported by Eftekhari and Farajzadeh (2017). The green curves in **Figure 4** report $f_w(S_w)$ data where S_w was inferred using the $k_{rw}(S_w)$ function reported by Kapetas et al. (2017), which was measured only in the absence of foam. Both k_{rw} functions correctly predict the trend in which S_w increases with decreasing f_w seen in the CT data. We discuss the details of the non-monotonic trend in $f_w(S_w)$ in **Chapter 5**. From our own data it is clear that the k_{rw} function reported by Eftekhari and Farajzadeh (2017) better reflects the water saturations measured with the CT scanner in our own experiments. Moreover, since the function was measured by Eftekhari and Farajzadeh (2017) over a wide range of surfactant concentrations C_S we assume it is suitable for analysing our foam scans performed at different values of C_S . Eftekhari and Farajzadeh (2017) also obtained separate fits for individual $k_{rw}(S_w)$ functions at a single values of C_S for relatively low capillary numbers. For the sake of simplicity, in this study, we analyse our experimental data using a single $k_{rw}(S_w)$ function, the one that is fitted over a wide range of surfactant concentrations. Nevertheless, for our sensitivity analysis, as we explain below, we use the $k_{rw}(S_w)$ function reported by Kapetas et al. (2017). We include the parameters of this function also in **Appendix A**.

We fit the $f_w(S_w)$ data using two methods. The first method (Eftekhari and Farajzadeh, 2017; Kapetas et al., 2017) is a least-squares optimization routine which fits the model parameters to apparent viscosity over a wide scan of foam qualities. This method assigns equal weight to all the experimental points in a foam scan, including

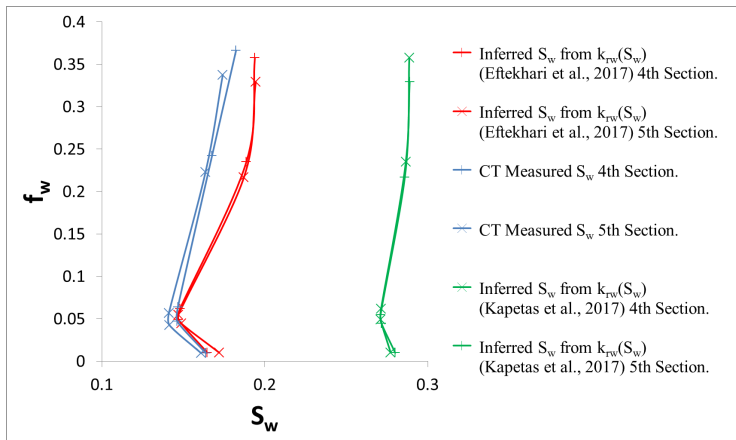


Figure 4.4: Fractional-flow function $f_w(S_w)$ for a foam scan performed at a total superficial velocity of 4.21 ft/day (1.48×10^{-5} m/s) with $C_S = 0.5$ wt.%. In the blue curves, S_w was measured directly using a CT scanner. In the red curves, S_w is inferred using the $k_{rw}(S_w)$ function presented by Eftekhari and Farajzadeh (2017). In the green curves, S_w is inferred using the $k_{rw}(S_w)$ function reported by Kapetas et al. (2017) with no foam present.

those in the low-quality regime. The second method focuses on experimental data in the high-quality regime (Rossen and Boeije, 2015), specifically near the point of tangency (cf. Figure 4.1). This method involves visual comparison of the data and the model fit. Therefore, the obtained parameters might not be unique. We illustrate the sensitivity to how this fit is done by making three different fits to the mobility data of one of the foam scans using the criteria of three different people. We describe the parameters used in both methods in Appendix A. With the model parameters obtained we scale up to a hypothetical field application. We describe the calculations in Appendix C. The parameter corresponding to the water saturation at which foam abruptly weakens, S_w^* , or $fmdry$ in the STARS foam model, is fixed in all our fits in which we used the method of Rossen and Boeije (2015). In addition, we fit the $f_w(S_w)$ data using a least-squares fit to the entire foam scan (Eftekhari and Farajzadeh, 2017; Kapetas et al., 2017), using a first guess based on the method of Boeije and Rossen (2015a). Therefore, for each foam scan, we obtain four parameter sets, where two were obtained with the method of Rossen and Boeije (2015) for a SAG and two using the fit to the entire foam scan (Eftekhari and Farajzadeh, 2017; Kapetas et al., 2017). Finally, we perform the fits again using the correction of Namdar Zanganeh et al. (2014), here denoted as NZ. This modification gives complete foam collapse at S_{wr} , which is expected if foam stability depends on capillary pressure (Khatib et al., 1988). We show the sensitivity of the up-scaled injectivity and mobility control at the shock at the field scale to the method of fitting the parameters and in the presence and in the absence of the correction of NZ.

Sometimes a suitable $k_{rw}(S_w)$ function is not available in the literature for a particular core sample. Therefore we illustrate the sensitivity of predicted field performance to the liquid-relative-permeability function, $k_{rw}(S_w)$, and the gas-relative-permeability function, $k_{rg}(S_w)$, by doing again the model fit using the functions reported by Kapetas et al. (2017). Then, we compare the mobility at the shock and injectivity predicted by these new parameter sets against our previous results.

4.7. RESULTS

As mentioned above, for a relatively low C_S (0.037 wt.%) there was no eruption of stronger foam at the core outlet, and we use steady-state data. For greater concentrations (0.1, 0.5 and 1.0 wt.%) we employed a foam generator. In these cases, where a stronger foam erupts at the core outlet at foam breakthrough, we report local-equilibrium mobility in the foam bank before foam breakthrough. **Appendix D** shows examples with evidence that foam is at local equilibrium in both cases. In all the experiments in the high-quality regime reported here, we found consistently uniform pressure gradient in the intermediate sections of the core (excluding the entrance and exit regions), in spite of increasing gas superficial velocity downstream due to modest effects of gas expansion. This is expected for foam in the high-quality regime (Alvarez et al., 2001).

Figure 4.5 shows the experimental data corresponding to the five foam scans performed in this study. This figure shows apparent foam viscosity, μ_{app} , as function of foam quality, $f_g = (1 - f_w)$. We define apparent viscosity as $\mu_{app} = k\Delta P / (Lu_t)$, where k and L denote rock permeability and the length of the core section used and ΔP is the pressure difference across that section, respectively. **Figure 4.5** also shows the model fit to the whole foam scan using the least-squares approach used by Eftekhari and Farajzadeh (2017) and Kapetas et al. (2017).

Figure 4.6 illustrates the experimental data around the point of tangency for each of the five foam scans performed in this study. We plot the $f_w(S_w)$ data in the colour of the corresponding foam scan in **Figure 4.5**. In all of these plots, we inferred S_w using the foam-scan data in combination with the $k_{rw}(S_w)$ function reported by Eftekhari and Farajzadeh (2017); see **Appendix A** for a complete description of the $k_{rw}(S_w)$ functions used in this study. On the left of **Figure 4.6**, we plot the $f_w(S_w)$ curves corresponding to the parameters obtained with the least-squares optimization of the whole foam scan. On the right, we plot the $f_w(S_w)$ curves corresponding to the parameters obtained using the method of Rossen and Boeije (2015) for a SAG. The complete set of parameters obtained with the least-squares optimization and the method of Rossen and Boeije (2015) are summarized in **Table 4.1** and **Table 4.2**, respectively. We provide a complete description of the foam parameters used in this

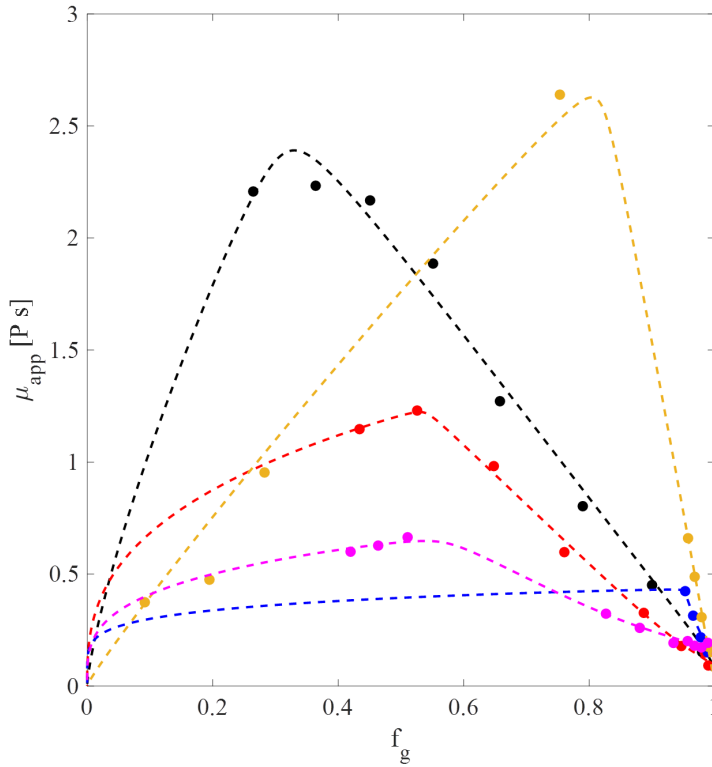


Figure 4.5: Experimental data for the five foam scans performed in this study. The black dots denote the experimental data for the foam scan performed with $u_t = 2.94 \times 10^{-6}$ m/s and $C_S = 0.037$ wt.%; the red dots data for $u_t = 7.35 \times 10^{-6}$ m/s and $C_S = 0.037$ wt.%; the pink dots data with $u_t = 1.47 \times 10^{-5}$ m/s and $C_S = 0.1$ wt.%; the blue dots data with $u_t = 1.47 \times 10^{-5}$ m/s and $C_S = 0.5$ wt.%; the yellow dots with $u_t = 7.35 \times 10^{-6}$ m/s and $C_S = 1.0$ wt.% AOS. The dashed lines denote the model fit to the whole foam scan in each case.

study in **Appendix A**. The shocks for a gas-injection process are represented in **Figure 4.6** by solid black lines. The mobilities just behind these shocks in $[\text{Pa s}]^{-1}$ predicted by the corresponding model fit are listed in **Table 4.1** and **Table 4.2**. We calculate these mobilities using the equation $\lambda_{rt} = k_{rw}(S_w)/(f_w\mu_w)$, where μ_w denotes the water viscosity, here equal to 1.0 m Pa s. This viscosity corresponds to a mobility of $\lambda_w = 1.0 \times 10^3 [\text{Pa s}]^{-1}$. Every set of data predicts excellent mobility control at the leading edge of the foam bank.

We calculate the inverse of injectivity using a dimensionless pressure, P_D , which measures how the scaled-up pressure at the injection well compares to that expected when injecting water into the same reservoir at the same volumetric rate. For instance, this means that a $P_D = 5$ for foam injection corresponds to five times the rise in pressure at the wellbore when injecting water into the reservoir at the same volumetric injection rate. For this upscaling, we assume a cylindrical and homogenous reservoir; we explain our approach in detail in **Appendix C**. For the strong foams reported here the dimensionless pressure rises abruptly at the very beginning of gas injection and stays nearly constant until foam breaks through, as illustrated in **Figure C.1** (cf. Boeije and Rossen (2015b)). Therefore, we report in **Table 4.1** and **Table 4.2** the maximum dimensionless pressure (here denoted as $MaxP_D$) during a gas-injection process.

In this study, we focus on capturing correctly the point of tangency for all of our experiments. Although the model fits use different methodologies and obtain different sets of parameters, both give nearly the same mobility at the shock and injectivity for experiments 1, 2 and 3, as we summarize in **Table 4.1** and **Table 4.2**. However, we found that the least-squares model fit to the whole foam scan for experiments 4 and 5 fails to capture the trend followed by the experimental points near the point of tangency. For example, in **Figure 4.6e** the model fit deviates from the trend of the data below $f_w = 0.005$. This failure produces an underestimation of the mobility control behind the shock front: the least-squares fit to the whole quality scan predicts a mobility of $15.25 [\text{Pa s}]^{-1}$ behind the shock, while the method of Rossen and Boeije (2015), based on closer fit to data in this range, gives an estimate of $5.36 [\text{Pa s}]^{-1}$. In this case the method of Rossen and Boeije (2015) for a SAG gives a better estimation of the mobility behind the shock. However, the method of Rossen and Boeije (2015) does not always give a good fit at lower foam qualities (greater f_w), as is evident at the top part of **Figure 4.6c'**.

We next test the sensitivity of the resulting foam parameters to the modification of Namdar Zanganeh et al. (2014) (NZ). For the model fit to the whole foam scan, the NZ modification does not affect the parameters obtained, as we summarize in **Table 4.1**. For the model fit using the method of Rossen and Boeije (2015) for a SAG, the parameters $fmmob$ and/or $epdry$ do differ when using the NZ correction, as

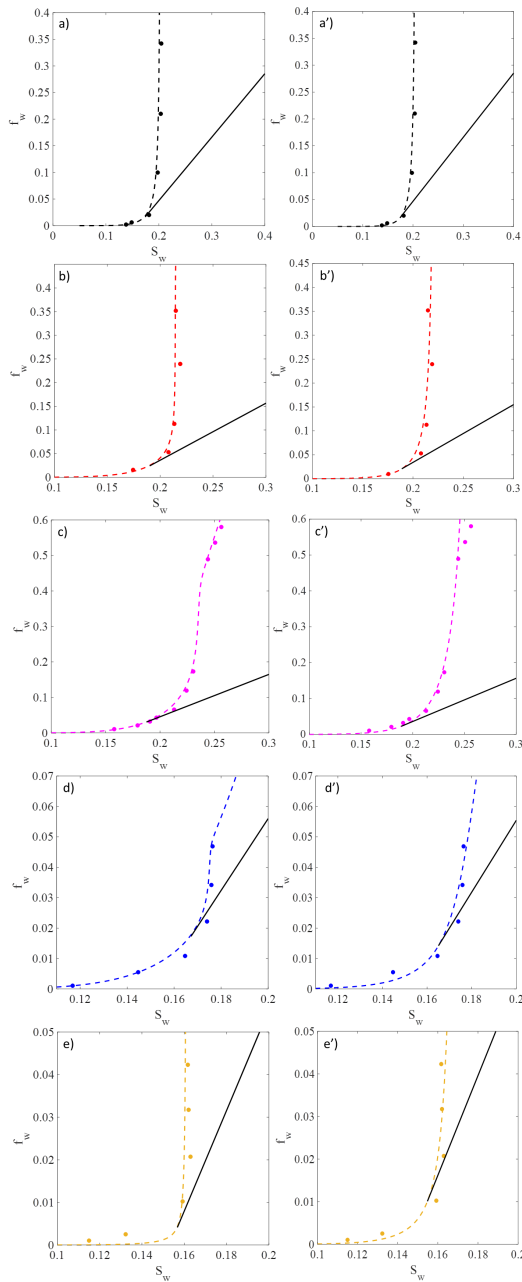


Figure 4.6: Experimental data around the point of tangency corresponding to the foam scans presented in **Figure 4.5**. On the left, $f_w(S_w)$ curves predicted by the model fit performed using the whole foam scan. On the right, $f_w(S_w)$ curves obtained using the method of Rossen and Boeije (2015) for a SAG (middle estimate; see sensitivity analysis below). The solid lines correspond to the predicted shocks during a gas-injection process.

Foam Parameters Optimized to the Entire Foam Scan (EFS)					
Experiment	1	2	3	4	5
C_S [wt.%]	0.037	0.037	0.1	0.5	1.0
u_t [m/s]	2.94×10^{-6}	7.35×10^{-6}	1.47×10^{-5}	1.47×10^{-5}	7.35×10^{-6}
u_t [ft./day]	0.83	2.12	4.25	4.25	2.12
STARS Foam Model					
$k_{rw}(S_w)$	Eftekhari and Farajzadeh (2017)				
$fmdry$	0.202	0.214	0.234	0.175	0.161
$fmmob$	2.98×10^5	9.33×10^5	9.47×10^8	5.47×10^6	8.71×10^4
$epdry$	812	2294	1766	1654	3446
$fmcap$	5.00×10^{-6}	2.00×10^{-5}	1.00×10^{-5}	5.00×10^{-5}	1.00×10^{-5}
$epcap$	0.09	1.00	3.00	4.26	0
$fmmob_{SAG}$	2.67×10^5	5.93×10^5	1.23×10^6	2.23×10^5	8.71×10^4
$MaxP_D$	44.1	32.8	63.0	30.8	13.1
λ_{rt} [Pa s] ⁻¹	6.6	8.7	6.0	7.2	13.0
NZ Correction					
$k_{rw}(S_w)$	Eftekhari and Farajzadeh (2017)				
$fmdry - NZ$	0.202	0.214	0.234	0.175	0.161
$fmmob - NZ$	2.98×10^5	9.33×10^5	9.47×10^8	5.47×10^6	8.71×10^4
$epdry - NZ$	812	2294	1766	1654	3449
$fmcap - NZ$	5.00×10^{-6}	2.00×10^{-5}	1.00×10^{-5}	5.00×10^{-5}	1.00×10^{-5}
$epcap - NZ$	0.09	1.00	3.00	4.26	0
$fmmob_{SAG} - NZ$	2.67×10^5	5.93×10^5	1.23×10^6	2.23×10^5	8.71×10^4
$MaxP_D$	22.9	17.3	25.3	20.3	10.9
λ_{rt} [Pa s] ⁻¹	7.6	10.0	7.6	7.8	13.5

Table 4.1: Foam parameters obtained by the least-squares routine used by Eftekhari and Farajzadeh (2017) and by Kapetas et al. (2017). We include the predicted total relative mobility, λ_{rt} , behind the shock front in [Pa s]⁻¹ and the maximum dimensionless pressure, P_D , reached during gas injection

Foam Parameters Optimized to the Point of Tangency (R&B)					
Experiment	1	2	3	4	5
C_S [wt.%]	0.037	0.037	0.1	0.5	1.0
u_t [m/s]	2.94×10^{-6}	7.35×10^{-6}	1.47×10^{-5}	1.47×10^{-5}	7.35×10^{-6}
u_t [ft./day]	0.83	2.12	4.25	4.25	2.12
STARS Foam Model					
$k_{rw}(S_w)$	Eftekhari and Farajzadeh (2017)				
$fmdry$	0.204	0.22	0.25	0.18	0.167
$fmmob$	5.00×10^5	5.00×10^5	4.00×10^5	2.5×10^4	6.5×10^4
$epdry$	1300	1600	600	75	300
$MaxP_D$	49.0	36.1	54.5	55.5	47.9
λ_{rt} [Pa s] ⁻¹	6.2	8.4	7.2	4.8	4.9
NZ Correction					
$k_{rw}(S_w)$	Eftekhari and Farajzadeh (2017)				
$fmdry - NZ$	0.204	0.22	0.25	0.18	0.167
$fmmob - NZ$	5.00×10^5	4.00×10^5	4.00×10^5	2.5×10^4	6.5×10^4
$epdry - NZ$	1000	1100	480	50	220
$MaxP_D$	28.6	19.7	24.3	38.0	35.7
λ_{rt} [Pa s] ⁻¹	6.3	9.1	8.2	4.6	4.6

Table 4.2: Foam parameters resulting from the method of Rossen and Boeije (2015) for SAG. We include the predicted total relative mobility, λ_{rt} , behind the shock front in [Pa s]⁻¹ and the maximum dimensionless pressure, P_D , reached during gas injection

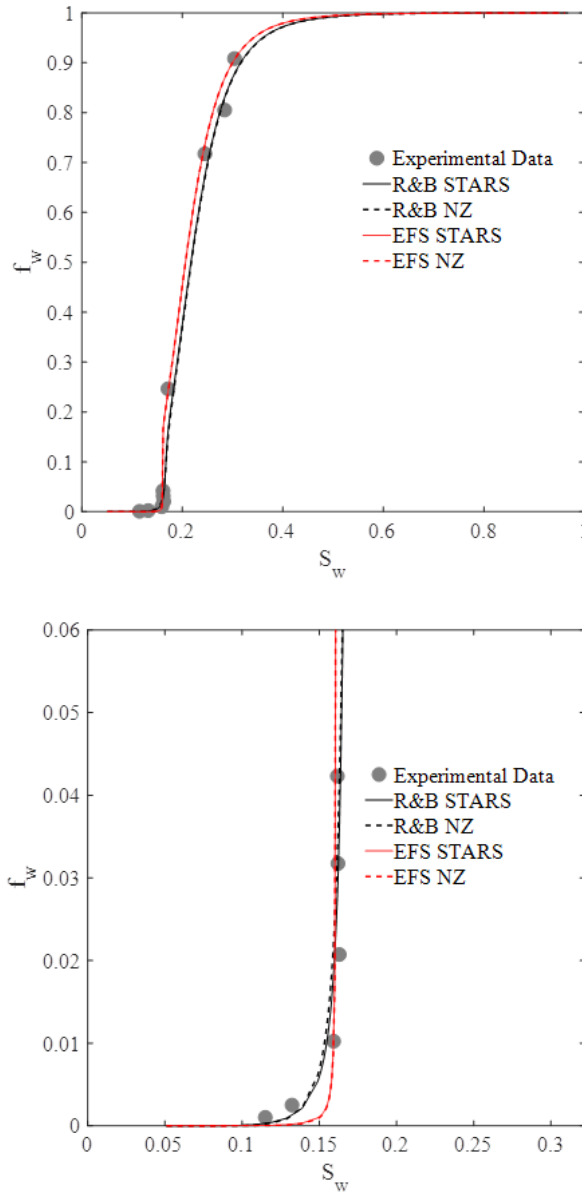


Figure 4.7: Four model fits for the data of Experiment 5. We performed two model fits using the method of Rossen and Boeije (2015) for a SAG; one without the NZ correction (here label as R&B STARS) and one with the NZ correction (here labelled R&B NZ). We performed the other two model fits using the method of Eftekhari and Farajzadeh (2017) to the entire foam scan; with and without the NZ correction, here labelled EFS STARS and EFS NZ, respectively. On the bottom, we present an expanded view near the tangency point.

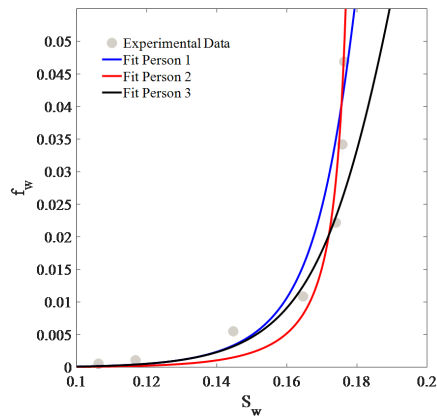


Figure 4.8: Model fits from the sensitivity test of the method of Rossen and Boeije (2015) using different criterion. See description in the text.

we present in **Table 4.2**. Ideally, this variation is not expected because the correction was designed to affect foam mobility at a single water saturation, specifically at S_{wr} . The resulting total relative mobilities, λ_{rt} , however, are practically the same, as we present in **Table 4.2** and illustrate in **Figure 4.7**. In addition, the consistent reduction of the maximum dimensionless pressure, $MaxP_D$, in the presence of the NZ correction, as depicted in **Table 4.1** and **Table 4.2**, illustrates the improvement in injectivity if foam collapses completely at S_{wr} .

We also test the variability in the resulting parameters for the method of Rossen and Boeije (2015) for a SAG, which relies on visual inspection. To that end, we perform a second fit and a third fit for the data of Experiment 4. In our first fit, presented in **Table 4.2**, we imagine a criterion (criterion 1) that focuses on obtaining a best middle estimate for all the experimental data. In the second fit, a criterion 2 that focuses on fitting data at relatively high f_w but accepts a poor fit around the point of tangency at $f_w = 0.01$ and 0.005 . Finally, a criterion 3 focuses on fitting the tangency condition as closely as possible, but disregards data at f_w well above the point of tangency. We present the resulting fits in **Figure 4.8** and we summarize the foam parameters and the up-scaled values in **Table 4.3**. On one hand, the criterion 2 does not capture the point of tangency well and the upscaling underestimates mobility control at the leading edge of the foam bank. Criteria 1 and 3 give similar estimates for mobility control at the leading edge and injectivity.

In the absence of liquid-saturation data, we could have used a different $k_{rw}(S_w)$ function available in the literature. Therefore, we also test the role of the choice of

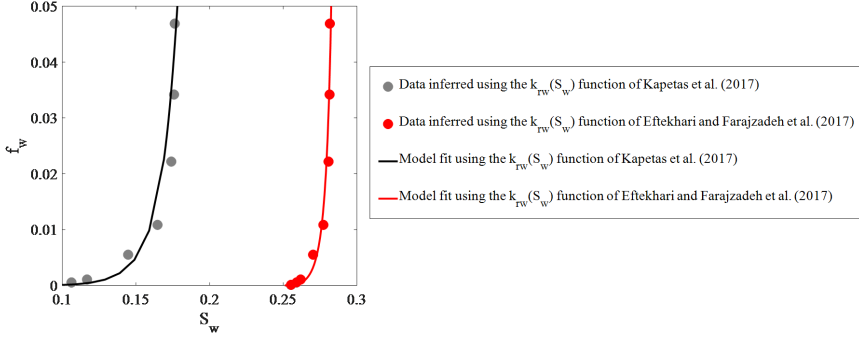


Figure 4.9: Two fits using different $k_{rw}(S_w)$ functions for the data of Experiment 4 using the method of Rossen and Boeije (2015). We summarize the resulting foam parameters in Table 4.4.

Fitting Criterion	1	2	3
Experiment	4	4	4
STARS Foam Model			
$k_{rw}(S_w)$	Eftekhari and Farajzadeh (2017)		
$fmdry$	0.18	0.18	0.18
$fmmob$	2.5×10^4	1×10^5	1.4×10^4
$epdry$	75	700	40
$MaxP_D$	55.5	29.9	56.2
$\lambda_{rt} [\text{Pa s}]^{-1}$	4.8	7.6	4.9

Table 4.3: Foam parameters resulting from the sensitivity test performed on Experiment 4 for the method of Rossen and Boeije (2015) for SAG. We include the predicted total relative mobility, λ_{rt} , behind the shock front in $[\text{Pa s}]^{-1}$ and the maximum dimensionless pressure, P_D , reached during gas injection

Fitting Criterion	1	1
Experiment	4	4
STARS Foam Model		
$k_{rw}(S_w)$	Eftekhari and Farajzadeh (2017)	Kapetas et al. (2017)
$fmdry$	0.18	0.285
$fmmob$	2.5×10^4	4×10^4
$epdry$	75	280
$MaxP_D$	55.5	55.5
$\lambda_{rt}[\text{Pa s}]^{-1}$	4.8	7.3

Table 4.4: Foam parameters fit using the method of Rossen and Boeije (2015). We use two different $k_{rw}(S_w)$ functions. We include the maximum dimensionless pressure, $MaxP_D$, and the total relative mobility, λ_{rt} , behind the shock front during gas injection in $[\text{Pa s}]^{-1}$

a particular $k_{rw}(S_w)$ function on the predicted λ_{rt} behind the shock and in the injectivity during gas injection. This is important because sometimes a directly verified $k_{rw}(S_w)$ is not available for a particular porous medium. We start our analysis considering the $k_{rw}(S_w)$ parameters published by Kapetas et al. (2017); we present a complete description of this function in **Appendix A**. This function was not able to reproduce the water-saturation measurements from our CT scans, as illustrated in **Figure 4.4**. Nevertheless, for illustration purposes we use the function to calculate the corresponding water saturations for each experimental point. Thereafter, we carry out the model fit using the method of Rossen and Boeije (2015). **Figure 4.9** illustrates the model fit and **Table 4.4** summarizes the parameters obtained, together with $MaxP_D$ and λ_{rt} . The mobility behind the shock increases to $7.31 [\text{Pa s}]^{-1}$, while the calculated injectivity remains practically the same. Although the water saturations are very different (**Figure 4.4**), this function can be used to obtain a reasonable estimate for injectivity, and the mobility at the shock is not very different from that with the other $k_{rw}(S_w)$ function. This could be explained by the fact that we use the same pressure data from the foam scan of Experiment 4 to infer both curves. This could of course fail if the $k_{rw}(S_w)$ function completely failed to represent true behavior.

4.8. DISCUSSION AND CONCLUSIONS

For gas injection in a SAG application the most suitable fitting method is the method of Rossen and Boeije (2015). The method is able to estimate the tangency conditions in all of our experiments. The method of Eftekhari and Farajzadeh (2017) to the entire foam scan may produce a poor estimation of mobility control at the shock. The method of Rossen and Boeije can give a poorer fit at higher values of f_w that apply where gas and liquid slugs mix away from the well, however.

The method of Rossen and Boeije (2015) might seem limited by relying on visual

inspection and by the criteria used by the person performing the fit. However, for the cases examined here the impact of these factors is modest given the uncertainty in other factors. For instance, in the worst-case scenario of our sensitivity analysis the difference between our best and worst estimates for mobility control is 2.8 [Pa s]^{-1} (about a 50% difference in mobility), which is not significantly bigger than the difference of 2.5 [Pa s]^{-1} arising from an incorrect selection of the liquid-relative permeability function.

We also find that injectivity can be estimated reasonably well using a different liquid-relative-permeability function. This could of course fail if the $k_{rw}(S_w)$ function completely failed to represent true behavior.

4

If foam collapses at S_{wr} , the Namdar Zaganeh correction is key in better reproducing the injectivity observed at the field scale. For the fits presented here the correction slightly affects the fit to data in the range measured. Therefore, the optimized foam parameters change slightly. The predicted mobility control at the leading edge of the foam bank with and without the correction are nearly the same.

None of the two methods is able in all of our experiments to capture the trends of the experimental points in both the low-quality and in the high-quality regimes using the same list of parameters or fit. We suggest to keep this compromise in mind when performing a model fit using any of the methods discussed here.

Our limited data suggest that increasing the surfactant concentration improves mobility control. Also, it suggests that the effect of total superficial velocity is limited. In other words, for the two velocities studied here at the same surfactant concentration the corresponding foams behave to a good agreement with a Newtonian rheology in the high-quality regime.

5

COREFLOOD STUDY OF NON-MONOTONIC BEHAVIOR WITH FOAM: IMPLICATIONS FOR SURFACTANT-ALTERNATING-GAS FOAM EOR

Foam is able to increase gas's sweep efficiency in Enhanced-Oil-Recovery applications. A surfactant-alternating-gas, or SAG, process is usually preferred for placing foam in the reservoir. During a SAG process, foam is generated away from the wellbore, offering both good injectivity and good mobility control at the leading edge of the foam bank.

Scale-up of laboratory data for SAG to field applications remains a challenge. Direct scale-up of dynamic SAG coreflood results is unreliable because of the dominance of core-scale artifacts. Steady-state coreflood data can be scaled up using fractional-flow theory (Boeije and Rossen, 2018; Kibodeaux and Rossen, 1997; Xu and Rossen, 2004). However, about half the published laboratory studies of foam fractional-flow curves report non-monotonic behavior, where at some point liquid saturation S_w increases with decreasing liquid fractional flow f_w . Rossen and Bruining (2007) warn that such behavior would result in foam collapse during injection of the gas slug in a SAG process at the field scale. Here we report and analyse a series of steady-state and dynamic

coreflood experiments to investigate the occurrence of non-monotonic fractional-flow behavior. These corefloods vary surfactant concentration, injected gas fraction (foam quality) and total superficial velocity and are supported by CT measurements. The CT data confirm that in these cases, as foam weakens with decreasing f_w , liquid saturation increases, confirming the non-monotonic $f_w(S_w)$ behaviour.

In our results, every case of non-monotonic fractional-flow behavior begins with propagation of foam from the inlet, followed by eruption of a much-stronger foam at the outlet of the core and backwards propagation of the stronger foam state to the inlet, similar to behavior reported by Apaydin and Kovscek (2001) and Simjoo and Zitha (2015). This suggests that there may be more than one stable local-equilibrium (LE) foam state. The initial creation of the stronger foam near the outlet is at least in part due to the capillary end effect. It is thus not clear which LE foam state controls behaviour of a SAG process in the field. There is the possibility that the stronger foam state may continue to depend on the end effect at later times. This issue requires further investigation.

5

In our results, the subsequent transition from a stronger- to a weaker-foam state, leading to non-monotonic $f_w(S_w)$ behavior, coincides with conditions for weaker foam (lower surfactant concentration, lower f_w) and less-vigorous foam generation (lower superficial velocity); this agrees with the theory of foam propagation of Ashoori et al. (2012). We discuss the implications of these findings, if confirmed to apply generally, for design of SAG foam processes.

5.1. INTRODUCTION

Foam can improve sweep efficiency in gas-injection enhanced-oil-recovery (EOR) processes (Rossen, 1996; Schramm, 1994). Surfactant-alternating-gas (SAG) injection is the preferred method of placing foam in the reservoir, both for operational and injectivity reasons (Heller, 1994; Matthews, 1989).

Scale-up of laboratory SAG coreflood data is challenging, because foam may not reach local equilibrium rapidly enough at core-scale dimensions, i.e., lengths and time, to scale-up behaviour directly to the field (Kapetas et al., 2014).

Assuming that local equilibrium applies on the field scale, it is possible to scale-up steady-state laboratory coreflood data to field scale using fractional-flow theory (Boeije and Rossen, 2018; Shan and Rossen, 2004; Zhou and Rossen, 1994). Fractional-flow theory teaches that upon injection of a gas slug in SAG there is a shock to a condition of very low water fractional flow f_w . Thus behaviour at low f_w is crucial to foam performance. **Figure 5.1** shows schematically the solution for the displacement as the first gas slug is injected into a reservoir saturated with surfactant solution

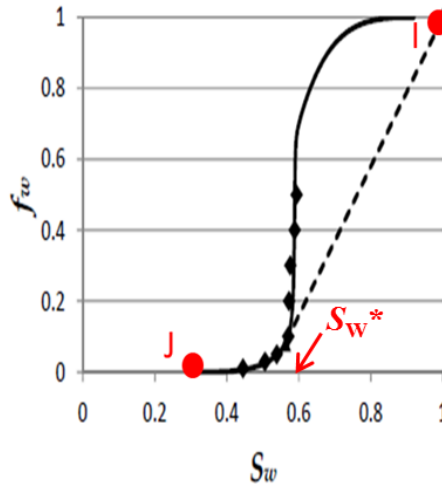


Figure 5.1: Construction of displacement by the first gas slug in a SAG process on fractional-flow curve: monotonic $f_w(S_w)$ function. Modified from Boeije and Rossen (2018)

on a diagram of f_w plotted as a function of water saturation S_w . J represents the injected fluid ($f_w = 0$) and I the initial state ($S_w = 1$). For simplicity we assume here that there is no mobile oil in the near-well region where the displacement takes place. All saturations in the displacement lie at fractional-flow values below the point of tangency representing the shock. Each saturation propagates with dimensionless velocity equal to the slope (df_w/dS_w) of the fractional-flow function at that saturation. The monotonic decrease in this slope and as f_w decreases represents the gradual transition between the low-mobility shock and dry conditions, with very high mobility, at the well. This high mobility helps injectivity (Al Ayesh et al., 2017). Fingering of drier, higher-mobility gas through the lower-mobility gas ahead of it within the foam bank can complicate behaviour (Farajzadeh et al., 2016; van der Meer et al., 2018); this issue is outside the scope of this thesis. The mobility at the shock (point of tangency in Fig. 5.1) is crucial. If mobility control is not maintained across the shock (between the point of tangency and I), viscous instability results and, in addition gravity, segregation of gas worsens.

Measuring steady-state mobilities at such low values of f_w is challenging. In addition, about half of the studies of the $f_w(S_w)$ function for foam processes find, not a monotonic decrease in S_w as f_w decreases, as in Fig. 5.1, but an increase in S_w over some range of f_w , and then a reversion to decreasing S_w , as illustrated in Fig. 5.2. Rossen and Bruining (2007) show that this behaviour then predicts a shock to fully collapsed foam on the bottom branch of the $f_w(S_w)$ curve, as shown in Fig. 5.2. Mobility control would in such a process would be much less favourable than in a

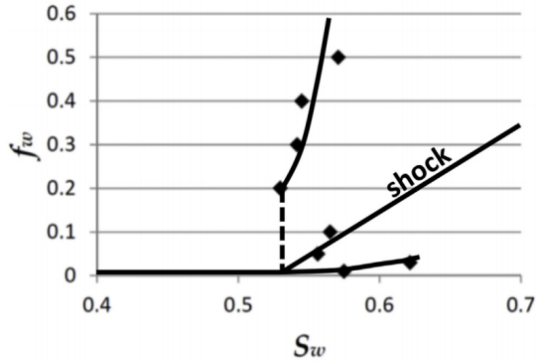


Figure 5.2: Non-monotonic $f_w(S_w)$ function and construction of displacement by the first gas slug in a SAG process. From Boeije and Rossen (2018)

5

process like that in Fig. 5.1.

In this chapter we report on the case with non-monotonic behaviour. In this study, in every case where non-monotonic behaviour was observed, that behaviour started with a laboratory artefact related to the capillary-end effect. In addition, the weakening of foam (increase in S_w and large increase in mobility) with decreasing f_w correlates with factors related either to reduced foam generation or reduced lamella stability. This suggests that the transition to weaker foam can be related either to a failure of foam generation or reduced foam stability. As seen in other studies (Ashoori et al., 2012; Yu et al., 2019a,b), transitions to weaker or stronger foam states depend on factors related to both foam generation and foam stability. We discuss the implications of these results for scale-up and design of SAG processes to field application.

5.2. EXPERIMENTAL PROCEDURE

We use the experimental apparatus described Section 4.2 and the materials presented in Section 4.3. Below we describe our experimental procedure. The experimental procedure is different from the experimental procedure described in Section 4.4 but some steps are repeated.

At the start of each experiment we injected 10 pore volumes (PV) of CO_2 to displace any gas inside the core. Next, we injected at least 10 PV of brine at elevated pressure (80 bars) to dissolve any CO_2 that remained in the core. Then, we measured the liquid permeability of the core. Finally, we injected 10 PV of surfactant solution to satisfy adsorption.

During each experiment we performed one or more foam-quality scans. Foam quality is gas fractional flow, i.e. $(1 - f_w)$. A foam scan is a series of steady-state measurements at different f_w and fixed total superficial velocity, u_t . Since our goal is to upscale a gas-injection process in SAG, we focus on data at low f_w . In order to assure that our results are independent of the initial state of the core, we performed steady-state measurements alternating between high and low foam qualities. Between experiments we injected at least 10 PV of gas.

As in some other experimental studies (Apaydin and Kovscek, 2001; Simjoo and Zitha, 2015), we observed the eruption of a much stronger foam at the end of the core and subsequent slow upstream propagation of the stronger foam state. In this paper we report the data after gas breakthrough and allowed for sufficient time for the stronger foam state to propagate through the core. In such cases we report the data from sections 4 and 5 after the entire core has settled into steady-state.

In most experiments we inferred water saturation, S_w , from measured mobility using an estimated water relative-permeability function $k_{rw}(S_w)$ for Bentheimer sandstone (Eftekhari and Farajzadeh, 2017; Kapetas et al., 2017). In one foam scan we monitored S_w using a medical CT scanner. We scanned the core horizontally in slices of 0.2 mm. Details of this procedure can be found, for example, in Eftekhari and Farajzadeh (2017). From the CT response, we calculated the liquid saturation in each voxel and from that the average in various cross-sections.

At the end of each experiment we cleaned the core as follows, following a procedure similar to that used by Eftekhari and Farajzadeh (2017) and Kahrobaei et al. (2017) on shorter cores. First, we injected 10 PV of a 50/50 water/isopropyl alcohol solution at elevated pressure (80 bar) to kill foam. Second, we injected 10 PV of water initially at elevated (80 bar) back-pressure, and we reduced pressure slowly to atmospheric in order to allow the expansion of trapped gas. Third, we injected 10 PV of CO₂ followed by an additional 10 PV of water at atmospheric pressure. Fourth, we flushed the core again with 20 PV of water while gradually raising the back-pressure until its value reached 80 bar. Then we gradually reduced pressure to atmospheric. Fifth, we vacuum-cleaned the core, followed by the injection of at least 10 PV of CO₂. Finally, we performed the preparation procedure described above and verified that the core had been restored to its initial permeability.

5.3. RESULTS

In this paper, we analyze steady-state data collected after the eruption of stronger foam at the core outlet and the subsequent propagation of this stronger foam state upstream of the core. The plot on the left of **Figure 5.3** depicts the propagation of

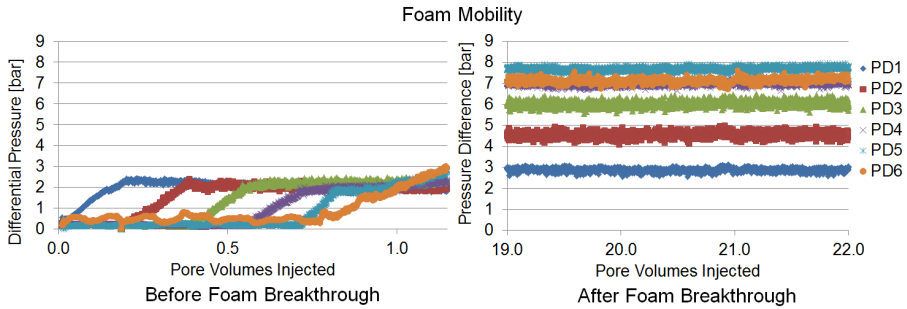


Figure 5.3: Sectional differential pressures in bars in foam coreflood as function of pore volumes injected. Since all sections have the same length, these values are directly proportional to pressure gradient in each section. On the left, before foam breakthrough. On the right, steady-state pressure difference long after foam breakthrough. The nominal foam quality and total superficial velocity and the surfactant concentration of this experiment are 95%, 4.25 ft/day and 0.5 wt%, respectively.

5

pre-generated foam downstream through the core, during a foam scan. The nominal foam quality (at back-pressure), nominal total superficial velocity and surfactant concentration are 95%, 4.25 ft/day and 0.5 wt%, respectively. This foam propagates with nearly uniform pressure gradient ∇p in all sections except the entrance and exit sections. At steady state, foam quality and total superficial velocity varies with gas expansion in the core, but liquid superficial velocity is uniform. At high foam quality, ∇p depends on liquid superficial velocity (Alvarez et al., 2001); thus ∇p in this advancing foam bank agrees with expected local-equilibrium behaviour.

As soon as the flowing foam breaks through to the outlet face of the core at about 1 PV injection, the eruption of a stronger foam starts at the core outlet and propagates upstream; this has just begun in Fig. 5.3, left. After a longer period of time, the system attains steady-state, illustrated in Figure 5.3, right. The foam present after breakthrough is considerably less mobile than the foam before foam breakthrough. Also, ∇p is different in all sections in this final configuration: it increases along the core. This behaviour would not be expected in the high-quality regime.

In contrast, we did not observe the eruption of stronger foam in a similar experiment under the same experimental conditions but with a higher foam quality (98%). Foam mobility before and after foam breakthrough were practically the same. Steady-state foam is considerably weaker in this case, as depicted in Figure 5.4.

A foam scan focused on the high-quality regime performed at a total superficial velocity of 4.25 ft/day (1.47×10^{-5} m/s) with $C_S = 0.5$ wt% is summarized in Figure 5.5. The mobilities measured during the foam scan reveal that foam weakened in an

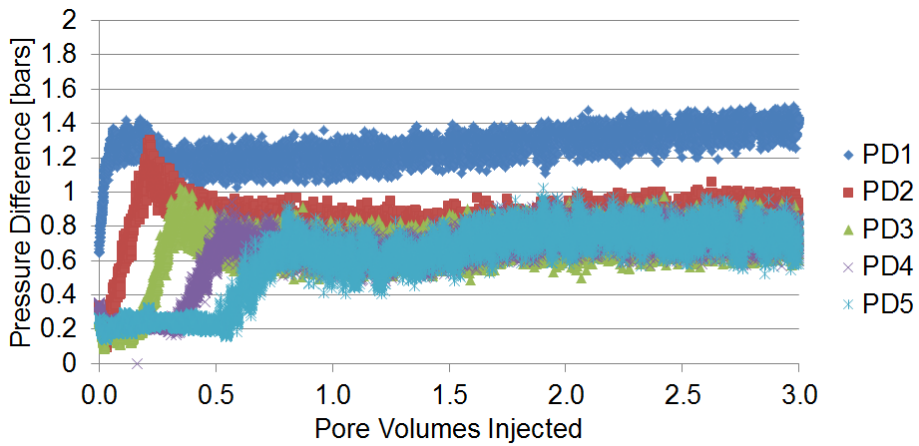


Figure 5.4: Sectional differential pressures in bars as function of pore volumes injected. The nominal foam quality and total superficial velocity and the surfactant concentration of this experiment are 98%, 4.25 ft/day and 0.5 wt%, respectively. Breakthrough has no effect on the mobility of foam upstream of the core.

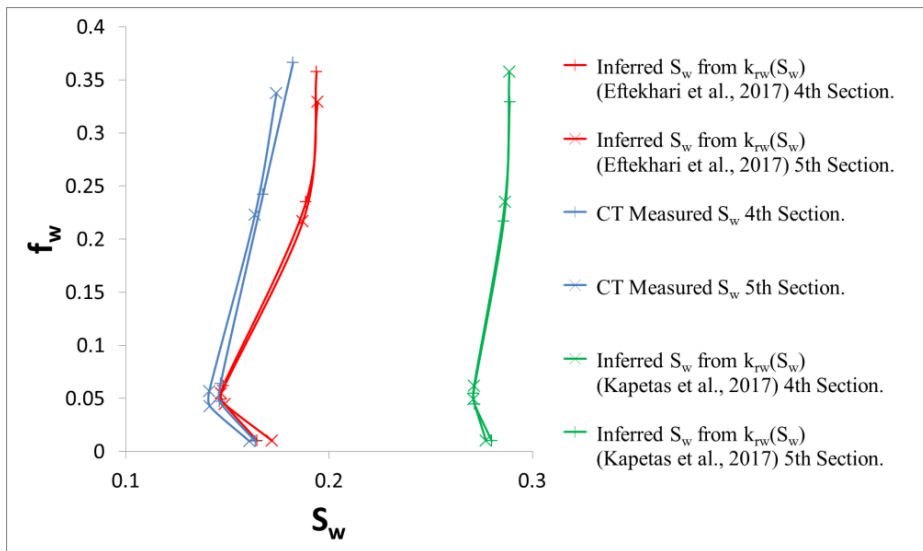


Figure 5.5: Fractional-flow function $f_w(S_w)$ for a foam scan performed at a total superficial velocity of 4.25 ft/day (1.48×10^{-5} m/s) with $C_S = 0.5$ wt%. The blue curves show S_w as measured directly using a CT scanner. The red curves show S_w as inferred using the $k_{rw}(S_w)$ function reported by Eftekhari and Farajzadeh (2017). The green curves show S_w as inferred using the $k_{rw}(S_w)$ function reported by Kapetas et al. (2017) based on data with no foam present.

unexpected manner as f_w decreased. During this foam scan, we used a CT scanner to monitor water saturation S_w . Our S_w measurements confirm that S_w indeed increased at some point as f_w decreased. This trend can be deduced from pressure-gradient data even using an approximate $k_{rw}(S_w)$ function. The green curves in **Figure 5.5** show S_w calculated from ∇p in two sections using the $k_{rw}(S_w)$ function measured by Kapetas et al. (2017) at low capillary number in the absence of foam. The estimated values of S_w are consistently greater than those measured with the CT scanner, but the trend of S_w with decreasing f_w is consistent with the CT data. The larger absolute values of S_w reflects the large value of irreducible water saturation S_{wr} that Kapetas et al. inferred from their fit of data in the absence of foam. Using the $k_{rw}(S_w)$ function measured by Eftekhari and Farajzadeh (2017) in the presence of foam (red curve in **Figure 5.5**) gives a better fit. Though not a quantitatively accurate fit to the CT results, it also fits the trend in the data. Thus, either of these two functions could have been used to deduce the non-monotonic trend of S_w upon decreasing f_w from ∇p data.

5

Our experiments suggest that the non-monotonic $f_w(S_w)$ behaviour is due to the eruption of stronger foam state at the core outlet. This eruption has been reported by others, especially at relatively high surfactant concentration (Apaydin and Kovscek, 2001; Simjoo and Zitha, 2015). In our results, the stronger foam does not appear in displacements at higher foam qualities. **Figure 5.6** illustrates this effect. At the start of the experiment, foam is at steady state with a foam quality of 99%. Liquid saturation is uniform along the core except at the inlet and outlet sections. After foam quality is reduced to 96%, holding the same total superficial velocity, a stronger foam forms near the core outlet and slowly propagates upstream, as illustrated in the S_w profiles at 4.3 and 6.1 pore volumes injected. Finally, steady state is achieved after 35 pore volumes injected. S_w in the final steady-state foam, with $f_g = 96\%$, is lower than the initial S_w of the steady-state foam with $f_g = 99\%$, especially near the outlet of the core, reflecting the stronger foam state.

In every non-monotonic case, with different C_s and u_t , there had been an eruption of stronger foam at the core outlet at mid ranges of f_w but not at the driest conditions. In our experiments, the non-monotonic behaviour is independent of the initial condition. If the initial condition lies at lower water fractional-flow than that at which transition from strong foam to weak foam occurs (i.e., the point where S_w increases as f_w decreases), $0.02 < f_w < 0.05$ in **Figure 5.8**, and next injection condition is at greater f_w , we see this eruption again. Let the water fractional flow at which S_w begins to increase with decreasing f_w (between 0.02 and 0.05 in **Fig. 5.5**) be denoted the transition water fraction, f_{wt} . When we took consecutive data at water fractional flow greater than f_{wt} , we did not observe a new eruption of a stronger foam state, but that stronger state had erupted earlier and filled the core during an earlier first displacement with $f_w > f_{wt}$. As a result, attaining steady state was faster when starting

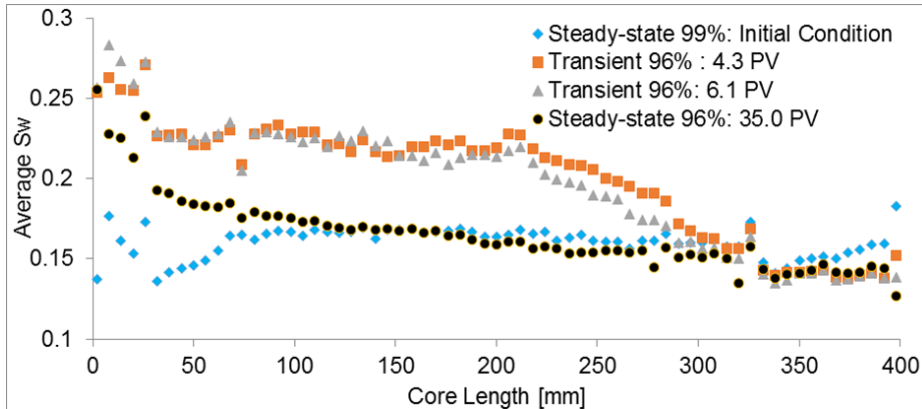


Figure 5.6: Average cross-section water-saturation S_w along the core during displacements at two foam qualities. The direction of the flow is from left to right. The decline in S_w with time at 96% foam quality shows a slow upstream propagation of stronger foam.

from a ‘wet’ initial condition, $f_w = 0.9 \gg f_{wt}$. because the slow upstream propagation of the stronger foam was not needed during the given displacement. This is confirmed by both S_w and pressure-gradient measurements. **Figure 5.7** shows that the final steady-state sectional pressure drops are achieved considerably faster when the displacement by foam with $f_w = 0.05 > f_{wt}$ is started with an initial state with $f_w = 0.9$ rather than $f_w = 0.01$.

Figure 5.8 depicts a non-monotonic fractional-flow curve. For illustration purposes, we upscale these data using fractional-flow theory. To that end, we construct the shock for the effective fractional-flow. We define apparent viscosity as $\mu_{app} = k\Delta P/(Lu_t)$, where k and L denote rock permeability and the length of the core section, respectively. The apparent viscosity predicted for the shock is approximately equal of 0.06 (Pas) (60 cp) which corresponds to a mobility of $\lambda_{rt} = 16.6[\text{Pas}]^{-1}$. This mobility ratio is still favourable for displacing water (viscosity 1.0 cp under these conditions) at 100% saturation, but mobility is much greater than if the shock had been to a point of tangency at larger f_w , as shown schematically in **Fig. 5.1**. Moreover, our experiments were conducted under conditions nearly ideal for foam stability: a clean, high-permeability core, relatively low salinity, relatively low temperature, no oil present, etc. Obtaining successful mobility control under more demanding conditions in the field would be more challenging.

Table 5.1 summarizes our results. At the lowest C_S and u_t we did not see the eruption of a stronger foam state at the core outlet. Increasing C_S is linked in our experiments to an extension of the stronger state to lower f_w . (i.e., a reduction in transition water fraction f_{wt}). Increasing C_S , even far above the CMC, increases lamella stabil-

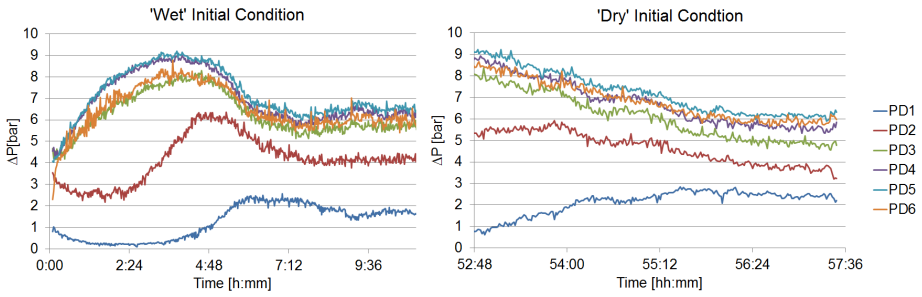


Figure 5.7: Sectional differential pressures in bars as function of time in two coreflood experiments with identical injection conditions but different initial conditions. The nominal foam quality and total superficial velocity and the surfactant concentration of this experiment are 95%, 4.25 ft/day and 0.5 wt%, respectively. On the left, steady state is achieved after 8 hours when the experiment is started from a 'wet' initial condition, $f_w = 0.9$. In contrast, steady state is achieved only after 55 hours when starting from a 'dry' initial condition, $f_w = 0.01$, right.

5

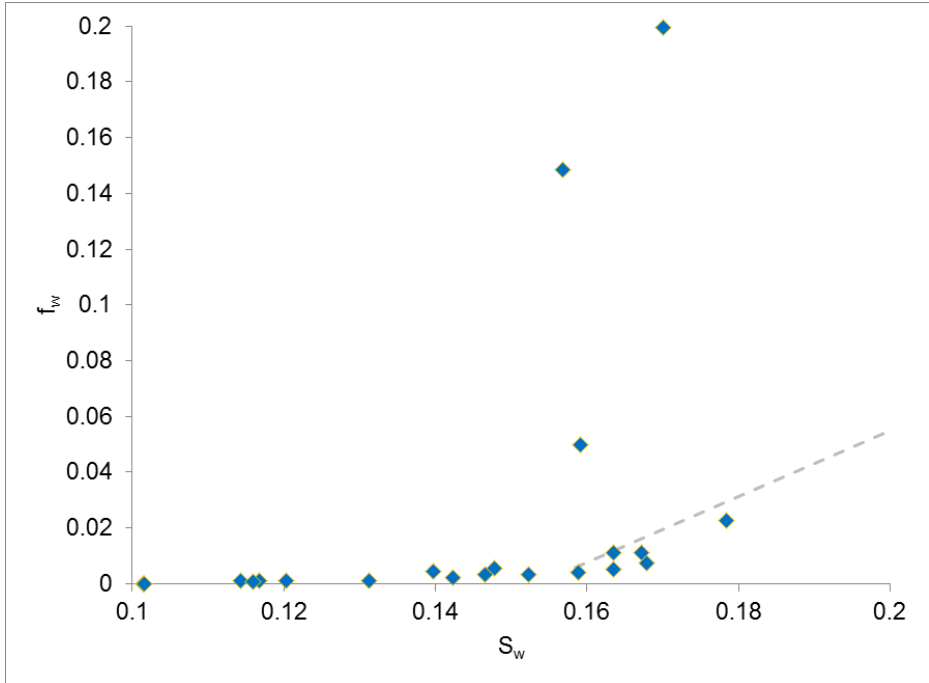


Figure 5.8: Fractional flow as function of water saturation for one non-monotonic set of data. u_t and C_S are equal to 1.5×10^{-5} m/s and 0.5 wt% AOS, respectively. We plot the shock as a dashed line according to the solution method of Rossen and Bruining (2007). f_{wt} denotes the fractional flow at which S_w starts to increase with decreasing f_w , which is between 0.05 and 0.02 in this experiment.

C_S (wt.%)	u_t (m/s,ft/day)	Monotonic at steady state?	Transition water fraction (f_{wt})
0.037	2.94×10^{-6} , 0.83	Yes	N/A
0.037	1.50×10^{-5} , 4.25	No	0.17
0.1	1.50×10^{-5} , 4.25	No	0.17
0.1	3.00×10^{-5} , 8.50	No	0.14
0.5	1.50×10^{-5} , 4.25	No	0.05
1.0	1.50×10^{-5} , 4.25	No	0.03

Table 5.1: Summary of Experimental Findings, f_{wt} denotes the fractional flow at which S_w starts to increase with decreasing f_w .

ity in porous media (Apaydin and Kovscek, 2001; Eftekhari and Farajzadeh, 2017). In the same way, our results indicate that increasing superficial velocity also reduces the value of f_{wt} . Increasing superficial velocity promotes lamella creation (Gauglitz et al., 2002; Kam and Rossen, 2003). These results suggest that the stronger state depends on a shifting balance between lamella stability and lamella creation (cf. Ashoori et al. (2012) and Yu et al. (2019a,b)).

5.4. DISCUSSION

The experiments examined here are limited to a single surfactant and core type, though surfactant concentration, superficial velocity and foam quality do vary. Demonstrating the generality of the results requires further study. Previous studies (Boeije and Rossen, 2018; Kibodeaux and Rossen, 1997; Wassmuth et al., 2001; Xu and Rossen, 2004) did not specifically address possible origins of non-monotonic $f_w(S_w)$ behaviour. Close examination of those studies is needed to see if their results are consistent with our findings.

In this study, every example of a non-monotonic fractional-flow curve began with the eruption of a strong foam state at the core outlet - at least arguably, an experimental artefact of the capillary end effect in a laboratory-scale coreflood (Apaydin and Kovscek, 2001). In addition, when this occurred, the resulting stronger-foam state did not show the invariance of ∇p with gas expansion along the core (cf. Fig. 5.3 left and right and Fig. 5.4) expected in the high-quality regime (Alvarez et al., 2001). It is possible that the stronger foam that erupts is in the low-quality regime, or that it is some state not consistent with either regime. However the increase in steady-state ∇p as one approaches the core outlet (Fig. 5.3, right) suggests the possibility that this lower-mobility state within the core remains, even at steady state, dependent on the capillary end effect at the end of the core. Moreover, the relevance of the capillary end effect to field application of foam is uncertain, although similar effects can oc-

cur at reservoir heterogeneities (Falls et al., 1988; Shah et al., 2019a,b; Tanzil et al., 2002). It is at least plausible that the coreflood data relevant to a SAG process in the field are those unaffected by the capillary end effect. In our study, we could obtain data excluding this effect either at low surfactant concentration or by using data from pre-generated foam, propagating at apparent local equilibrium (Fig. 5.3 left) before foam breakthrough at the core outlet.

Our finding of a transition from this stronger foam to a weaker foam state as f_w decreases agrees with research on foam generation (Yu et al., 2019a), propagation (Ashoori et al., 2012; Yu et al., 2019b) and collapse (Kam et al., 2007; Yu et al., 2019b). Specifically, maintenance and propagation of a strong-foam state depends on both lamella-creation mechanisms (affected in this case by superficial velocity and pressure gradient) and lamella stability (affected in this case by f_w and surfactant concentration). However, much current modelling of foam is based on the idea of a single strong-foam state that is regulated by pore size and the limiting capillary pressure P_c^* (Alvarez et al., 2001; Khatib et al., 1988; Rossen and Zhou, 1995). If there are two steady states of strong foam, this raises the question: which is regulated by P_c^* ? What regulates the other state?

Modelling (Kam and Rossen, 2003) and experimental (Gauglitz et al., 2002) studies that now accommodate multiple foam steady states predict an abrupt transition from a strong-foam state with decreasing superficial velocity to a state of nearly complete foam collapse. The model of Lotfollahi et al. (2017) allows for multiple strong-foam states in that a stronger foam state may be locked in as velocity is reduced. Our laboratory data suggest a gradual transition, over a range of f_w , to a state of distinctly weaker strong foam. We are unaware of a model that predicts this behaviour.

Our data indicate monotonic $f_w(S_w)$ behaviour at the lowest surfactant concentrations. These concentrations are below those usually proposed for field application. However our laboratory conditions (low temperature, mild salinity, clean, water-wet rock, absence of oil) are ideal for strong foam. Under more challenging conditions in many field applications, the behaviour at higher surfactant concentrations may be closer to those we see at low concentration (and hence reduced foam stability in porous media).

5.5. CONCLUSIONS

In this study, every case of non-monotonic $f_w(S_w)$ data began with eruption of a much-stronger foam state at the time of foam breakthrough at the core outlet, an apparent result of the capillary end effect.

The importance and generality of this finding requires further study with a wider

range of surfactant formulations and experimental conditions and a close examination of previous work, especially behaviour before attainment of steady state. At this point, the relevance of laboratory data taken subsequent to this event is uncertain. In this study, if foam eruption at breakthrough occurred at the core outlet, we were able to obtain monotonic $f_w(S_w)$ data by injecting pregenerated foam and taking data before foam breakthrough. No such precaution was needed at the lowest surfactant concentrations tested.

The transition from a stronger to a weaker foam state with decreasing superficial velocity and lower foam quality is consistent with modelling of foam generation, propagation and collapse. It does raise the questions of which steady state is most relevant to field application, and how both steady states can be consistent with the concept of a single limiting capillary pressure at a given surfactant concentration and superficial velocity.

Non-monotonicity in $f_w(S_w)$ was correctly inferred from pressure-gradient data using the water-relative-permeability function, even in cases where that function did not predict the absolute value of water saturation correctly.

6

CONCLUSIONS AND RECOMMENDATIONS

In this thesis we shed some light on several aspects regarding the injection of the first gas slug following the first surfactant slug during a SAG foam EOR process. Using fractional-flow theory we compare directly a co-injection process and a SAG process in a simple heterogeneous reservoir model. We extend fractional-flow theory to explore the implications of a non-Newtonian rheology during the injection of the first gas slug in a homogeneous reservoir. We measure and report mobility data relevant to modeling a gas-injection process during a SAG. We upscale the data to a hypothetical field application at different surfactant concentrations and different total superficial velocities. We perform a sensitivity analysis on the foam parameters obtained from these data. Finally, the analysis of our experimental data suggests that the capillary end effect, observed at high surfactant concentrations and high total superficial velocities, which triggers the generation of a stronger foam at the core outlet, is correlated to a non-monotonic trend in the $f_w(S_w)$ curve. This is true, at least, for our experiments. Below, we describe in detail our findings and give recommendations for future work. In the following sections we list the conclusions of each chapter.

6.1. CONCLUSIONS

6.1.1. CHAPTER 2: "FOAM DIVERSION IN HETEROGENEOUS RESERVOIRS: EFFECT OF PERMEABILITY AND INJECTION METHOD"

This is the first study to apply foam-model parameters fit to the two foam flow regimes for the same surfactant formulation over this wide a range of permeabilities, in a comparison of vertical conformance with different injection strategies with foam. The foam parameters of Kapetas et al. (2017) represent ideal conditions (low salin-

ity, low temperature, and absence of oil). They measured very low mobilities, lower than would be practical to apply in the field. Nevertheless, we believe the following conclusions apply more broadly.

- The only process that gave effective diversion into the lowest-permeability layer (300 times lower permeability than the highest-permeability layer) was a SAG process that isolated this layer from receiving surfactant injection. One of the other layers (Berea) still failed to get an equal share of gas in the process.
- Single-slug SAG processes have much better injectivity than the co-injection of gas and surfactant solution, especially if foam collapses at residual water saturation S_{wr} (as shown in the Namdar Zanganeh model). In some SAG processes examined here, with successful diversion of foam into two of the three lower-permeability layers, injectivity is better with foam than injecting water into a water-saturated reservoir.
- Single-slug SAG processes have an additional advantage when most surfactant is injected into the highest-permeability layer, giving the largest foam bank there. With the extremely strong foams modeled here, very small surfactant slugs suffice for effective diversion. The advantage remains during subsequent gas injection in SAG, unlike diversion in direct foam injection, in which foam eventually fills the near-wellbore region of all layers.
- It is extremely important whether foam collapses at S_{wr} , both for diversion and injectivity in SAG processes. This is reflected here in the different results for the STARS model compared to the Namdar Zanganeh modification of that model.
- A process of direct foam injection performs better than in the plots of Kapetas et al. (2017) (Fig. 2.1) because more foam is placed over time in the layers taking most of the flow. This advantage declines with time as foam fills more of all the layers.
- Diversion between layers reflects an interplay between various foam parameters. For foam injection, in the low-quality regime, total relative mobility depends on model parameter $fmmob$, the mobility reduction in the low-quality regime, and $epcap$, which rescales $fmmob$ with pressure gradient (i.e., introduces non-Newtonian behavior). In the high-quality regime, if $epdry$ is large, mobility depends most of all on $fmdry$, the water saturation at which foam collapses. We have only illustrated the effects of non-Newtonian behavior in the low-quality regime here, for simplicity, but that effect is significant, (Chapter 3 provides further discussion of non-Newtonian behavior in SAG processes.) For SAG injection, diversion depends on mobility at the shock, which depends on several foam parameters, and on whether foam collapses completely at irreducible water saturation.

6.1.2. CHAPTER 3: "FRACTIONAL-FLOW THEORY FOR NON-NEWTONIAN SURFACTANT-ALTERNATING-GAS FOAM PROCESSES"

In this chapter we present a method of solution for behavior during initial gas injection in a non-Newtonian SAG process that includes the interactions between the shock and the characteristics. The methodology can be applied to both shear-thinning and shear-thickening behavior.

- For a shear-thinning foam, we find that mobility control improves as the foam front propagates from the well, but injectivity declines somewhat with time. However, injectivity is still more favorable than for a Newtonian foam with the same mobility at the outer radius. In the case of a foam with marginal mobility control, there could be problems with viscous fingering as foam initially advances from the near-well region. For a shear-thinning foam, the shock does not necessarily satisfy the conventional tangency condition that applies to Newtonian foam, though it does continually approach it. In addition, the mobility at the front need not fit the power-law behavior seen at fixed gas fraction in the laboratory.
- For a shear-thickening foam, mobility control deteriorates as the foam front advances, though injectivity improves somewhat with dimensionless time. However, injectivity is less favorable than for a Newtonian foam with the same mobility far from the well. In a case of marginal mobility control, the foam could have problems with viscous fingering far from injection well.
- Overall, injectivity is a complex result of changing saturations and varying superficial velocities very near the well. Conventional simulators cannot adequately represent these effects, or estimate injectivity accurately, in the absence of exceptional grid resolution near the injection well.
- Finally, we recommend this study to be considered as illustrative and not as predictive. The main reason behind this recommendation is the fact that foam rheology can be far more complex than what we considered here. For example, recent experimental results (Kahrobaei et al., 2017) indicate that a single foam can be shear-thinning within a given range of total superficial velocities and shear-thickening within a different range.

6.1.3. CHAPTER 4: "SCALE-UP OF LABORATORY DATA FOR SINGLE-SLUG SURFACTANT-ALTERNATING-GAS FOAM EOR"

- For gas injection in a SAG application the most suitable fitting method is the method of Rossen and Boeije (2015). The method is able to capture the tangency conditions in all of our experiments. The method of Eftekhari and Farajzadeh (2017) to the entire foam scan may produce a poor estimation of mobility control at the shock. The method of Rossen and Boeije can give a poorer fit

at higher values of f_w that apply where gas and liquid slugs mix away from the well, however.

- The method of Rossen and Boeije (2015) might seem limited by relying on visual inspection and is subject to the criteria used by the person performing the fit. However, for the cases examined here the impact of these factors is modest given the uncertainty in other factors. For instance, in the worst-case scenario of our sensitivity analysis the difference between our best and worst estimates for mobility control is $2.8 [Pa\ s]^{-1}$, which is not significantly larger than the difference of $2.5 [Pa\ s]^{-1}$ coming from an incorrect selection of the liquid-relative-permeability function.
- We also find that injectivity can be estimated reasonably well using a different liquid-relative-permeability function. This could of course fail if the $k_{rw}(S_w)$ function completely fails to represent true behavior.
- If foam collapses at irreducible water saturation S_{wr} , the Namdar Zaganeh correction is key in better reproducing the injectivity observed at the field scale. For the fits presented here the correction slightly affects the fit to data in the range measured. Therefore, the optimized foam parameters change slightly. The predicted mobility control at the leading edge of the foam bank with and without the correction are practically the same.
- None of the two fitting methods is able in every one of our experiments to capture the trends of the experimental data in both the low-quality and in the high-quality regimes using the same list of parameters or fit. We suggest to keep this compromise in mind when performing a model fit using any of the methods discussed here.
- Our limited data suggest that increasing the surfactant concentration improves mobility control. Also, it suggests that the effect of total superficial velocity is limited. In other words, for the two velocities studied here at the same surfactant concentration the corresponding foams behave with a good agreement to a Newtonian rheology in the high-quality regime.

6.1.4. CHAPTER 5: "COREFLOOD STUDY OF NON-MONOTONIC BEHAVIOR WITH FOAM: IMPLICATIONS FOR SURFACTANT-ALTERNATING-GAS FOAM EOR"

- In this study, every case of non-monotonic $f_w(S_w)$ data began with eruption of a much-stronger foam state at the time of foam breakthrough at the core outlet, an apparent result of the capillary end effect.
- The importance and generality of this finding requires further study with a wider range of surfactant formulations and experimental conditions and a close

examination of previous work, especially behavior before attainment of steady state. At this point, the relevance of laboratory data taken subsequent to this event is uncertain. In this study, if foam eruption at breakthrough occurred at the core outlet, we were able to obtain monotonic $f_w(S_w)$ data by injecting pre-generated foam and taking data before foam breakthrough. No such precaution was needed at the lowest surfactant concentrations tested.

- The transition from a stronger to a weaker foam state with decreasing superficial velocity and higher foam quality is consistent with modelling of foam generation, propagation and collapse (Kam et al., 2007). However, no current model can incorporate the existence of two strong steady-states in the absence of oil. The model of Lotfollahi et al. (2016) allows for multiple strong-foam states in that a stronger foam state may be locked in as velocity is reduced—this is a separate issue to that found here. The co-existence of these two strong steady states in our study does raise the question which steady state is most relevant to field applications, and how both steady states can be consistent with the concept of a single limiting capillary pressure at a given surfactant concentration and superficial velocity.
- Non-monotonicity in $f_w(S_w)$ was correctly inferred from pressure-gradient data using the water-relative-permeability function, even in cases where that function did not predict the absolute value of water saturation correctly.

6.2. RECOMMENDATIONS

The model developed in **Chapter 2** offers a good starting point for validating other models that rely on solving the flow equations using a numerical scheme. Once such a model is validated, it can represent cross-flow between layers and gravity segregation, which are not represented in our model. We recommend to put emphasis on the correct reproduction of near-well behavior controlling injectivity and of the shock. The correct reproduction of near-well behavior depends on sufficient grid refinement in this region of the flow domain. The correct reproduction of the shock requires one to implement an adaptive grid that travels with this discontinuity

The methodology that we developed in **Chapter 3** could be implemented to model the more complex scenario found by Kahrobaei et al. (2017) and noted above. However, for complex problems the simplicity of using an analytical method could be lost.

The results of **Chapter 4** still need to be validated against a dynamic SAG experiment in a sufficiently long core. This validation would constitute a direct and final test for the success of the injection of the first gas slug during a SAG. Also, the role of multiple gas and surfactant slugs needs to be studied. In this case, the challenges encountered in this thesis to achieve local equilibrium might not be relevant if after the injection of multiple pore volumes local equilibrium is more rapidly achieved upon injection

of each new slug (Gong et al., 2019a).

In **Chapter 5** we find a correlation between the capillary end effect for high surfactant concentrations and the occurrence of non-monotonic fractional-flow curves. However, this does not exclude the possibility of the existence of other mechanisms correlated to the occurrence of multivalued fractional-flow curves. We think that the physics of this phenomenon is far more complex than we discussed here. Again, experiments in a sufficiently long core would be a more reliable test of our hypothesis. We suggest to use a range of different surfactant concentrations to study the phenomenon in detail. Also, we suggest to pay special attention to possible experimental artifacts that could be responsible for non-monotonic behavior.

A

COREY-BROOKS RELATIVE-PERMEABILITY MODEL AND FOAM MODEL

According to the Corey-Brooks relative-permeability model the water and gas relative-permeabilities are defined as

$$k_{rw} = k_{rw}^0 S^{n_w} \quad (\text{A.1})$$

$$k_{rg} = k_{rg}^0 (1 - S)^{n_g} \quad (\text{A.2})$$

$$S = \frac{S_w - S_{wr}}{1 - S_{wr} - S_{gr}} \quad (\text{A.3})$$

where k_{rw} , k_{rg} , k_{rw}^0 , k_{rg}^0 , n_w , n_g , S , S_w , S_{wr} and S_{gr} denote, respectively, liquid and gas relative permeabilities, the end-point water and gas relative permeabilities, the water and gas Corey-Brooks exponents, normalized water saturation, and the residual water and gas saturations. Table A.1 summarizes the two sets of Corey-Brooks parameters used in this study. Kapetas et al. (2017) obtained their set of parameters in the absence of foam and at relatively small pressure gradient, while Eftekhari and Farajzadeh (2017) performed a fit on a data set containing both data from core-flood experiments in the presence of foam at different surfactant concentrations (0.03 wt.%; AOS, 0.1 wt.% AOS; 0.5 wt.% AOS and 0.5 wt.% Amphosol) and data from the literature in the absence of foam at large pressure gradient. We use the parameters of Eftekhari and Farajzadeh (2017) to infer the water-saturation data

Corey-Brooks Parameters			
Kapetas et al. (2017)		Eftekhari and Farajzadeh (2017)	
No surfactant and at low pressure gradients.		Range of $C_s = [0.03 \text{ wt.}\%; \text{AOS}, 0.1 \text{ wt.}\% \text{ AOS}; 0.5 \text{ wt.}\% \text{ AOS and } 0.5 \text{ wt.}\% \text{ Amphosol}]$	
$S_{wr} = 0.25$	$S_{gr} = 0.2$	$S_{wr} = 0.05$	$S_{gr} = 0.03$
$k_{rw}^0 = 0.39$	$k_{rg}^0 = 0.59$	$k_{rw}^0 = 0.72$	$k_{rg}^0 = 0.59$
$n_w = 2.86$	$n_g = 0.7$	$n_w = 4.42$	$n_g = 0.94$

Table A.1: Corey-Brooks parameters used in **Chapter 4**

reported here and to perform the corresponding fits and calculations. We use the Corey-Brooks parameters of Kapetas et al. (2017) to study the impact of using a function that does not reproduce liquid-saturation measurements and in our study of **Chapter 2**.

In the presence of foam, the STARS model (Chen and Mohanty, 2014; CMG, 2015) represents the effect of foam by altering only the gas relative permeability. To model this effect it incorporates a mobility-reduction factor, FM , in the gas phase as follows,

$$u_t f_g = -\frac{k k_{rg}^f}{\mu_g} \nabla P = -\frac{k k_{rg} FM}{\mu_g} \nabla P \quad (\text{A.4})$$

where u_t , f_g , k , k_{rg} , k_{rg}^f , μ_g and ∇P denote, respectively, total superficial velocity, quality (gas fractional flow), permeability, gas relative permeability in the absence and presence of foam, respectively, gas viscosity and pressure gradient.

The mobility-reduction factor, FM , models the effects of surfactant concentration, water saturation, oil saturation, gas velocity, capillary number and the critical capillary number, respectively, on gas mobility. Here we focus on the dependence on water saturation (and, by implication, on capillary pressure) through the function F_2 , which controls behavior in the high-quality regime. For a fit to an entire foam scan, including the low-quality regime, it is essential to include also the dependence on capillary number through the function F_5 , which is important in that regime. Otherwise, to fit data in this regime, the model distorts the value of $epdry$, which is important in the high-quality regime as well (cf. Farajzadeh et al. (2015)). In that case the mobility-reduction factor becomes

$$FM = \frac{1}{1 + fmmob F_2 F_5} \quad (\text{A.5})$$

where the parameter $fmmob$ is the reference gas-mobility-reduction factor for wet

foams.

F_2 , also known as the dry-out function, models the abrupt collapse of foam produced by the limiting capillary pressure at a characteristic water saturation value ($fmdry$, in the STARS) with the following expression, where $epdry$ controls the abruptness of the transition. The above model does not incorporate foam collapse at irreducible water saturation, S_{wr} . If we further assume complete foam collapse at S_{wr} , we add the NZ modification (Namdar Zanganeh et al. (2014)). In this case the expression for F_2 is,

$$F_2 = \left[0.5 + \frac{\arctan(epdry(S_w - fmdry))}{\pi} \right] - \left[0.5 + \frac{\arctan(epdry(S_{wr} - fmdry))}{\pi} \right] \quad (\text{A.6})$$

where the second term forces a complete foam collapse making $F_2 = 0$ at S_{wr} .

The F_5 function models shear-thinning rheology in the low-quality regime through the parameters $fmcap$ and $fmcap$ as follows,

$$F_5 = \begin{cases} \left(\frac{fmcap}{N_{ca}} \right)^{epcap} & \text{if } N_{ca} > fmcap \\ 1 & \text{any other case} \end{cases} \quad (\text{A.7})$$

where the parameter $fmcap$ acts as a reference capillary number and the parameter $epcap$ is related to the power law exponent, n , by $n \approx 1/(1 + epcap)$. Here, the capillary number for foam is defined as $N_{ca} = (k\nabla P)/\sigma_{wg}$; where σ_{wg} denotes the surface tension between the aqueous and gas phases.

In the high-quality regime that dominates SAG processes, the shear-thinning behaviour of the low-quality regime is not important. Since in the model F_5 is bounded at 1 for $N_{ca} < fmcap$, one must set $fmcap$ to a value at least as small as the smallest value of N_{ca} expected to be encountered in a given simulation (Boeije and Rossen (2015a)). This in turn alters the value of $fmmob$ in the fit. To correct for this alteration in the value of $fmmob$ while excluding F_5 in the scale-up for SAG, we replace the value of $fmmob$ from the model fit with the product of the fitted value of $fmmob$ and the value of F_5 that applies in the range of the pressure gradient of the laboratory data, particularly at the tangency condition which governs the gas injection process of the first slug. Let this value of F_5 that applies approximately in the vicinity of the point of tangency be $F_{5'}$ (a constant). We denote this new $fmmob$ as $fmmob_{SAG}$,

$$fmmob_{SAG} = F_{5'} fmmob \quad (\text{A.8})$$

For the scale-up of SAG data in **Chapter 4**, we drop the F_5 factor from equation A.4 and we replace $fmmob$ with $fmmob_{SAG}$.

B

DISCRETIZATION SCHEME IN OUR FINITE-DIFFERENCE SIMULATOR

Equation 3.1 is discretized as follows,

$$S_{wt}(t + \Delta t) = S_{wt}(t) + \Delta t \left(\frac{f_w(S_{wi-1}(t)) - f_w(S_{wi}(t))}{\Delta x} \right) \quad (\text{B.1})$$

where S_{wi} , S_{wi-1} , f_w , t , Δt and Δx denote the saturation of the given grid block, the saturation of the grid block upstream of this block, water fractional flow, time, time increment and dimensionless grid block length, respectively.

The pressure evolution is calculated using Darcy's Law. In our discretization scheme Darcy's Law takes the form,

$$P_{i-1} = P_i + \left(\frac{Q}{4\pi hk} \right) \left(\frac{1}{\lambda_{rt}(r_i, S_{wi})} + \frac{1}{\lambda_{rt}(r_{i-1}, S_{wi})} \right) \ln \left(\frac{r_i}{r_{i-1}} \right) \quad (\text{B.2})$$

where P_{i-1} , P_i , r_i , r_{i-1} , S_{wi} , λ_{rt} , Q , h and k denote the pressures and radii at the inner and outer boundaries of the grid block, the saturation in the grid block, total relative mobility, total volumetric injection rate, thickness of the reservoir and permeability, respectively.

C

DIMENSIONLESS PRESSURE AS FUNCTION OF DIMENSIONLESS TIME

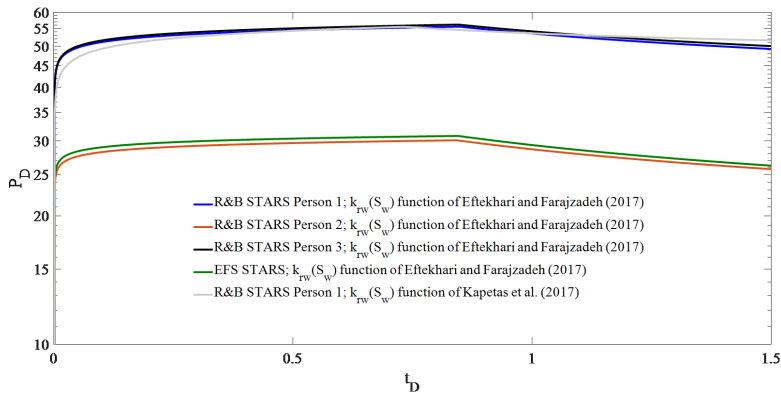


Figure C.1: Injectivity for different fits for the data of Experiment 4. We use the foam scan data corresponding to Experiment 4. The corresponding foam parameters and mobilities behind the shock are listed in [Table 4.1](#), [Table 4.3](#) and [Table 4.4](#).

We upscale our parameters to a hypothetical field application, assuming that the reservoir is cylindrical and homogenous with inner radius $r_w = 0.1 \text{ m}$ and outer radius $r_e = 100 \text{ m}$, where the outer boundary is open. We define the dimensionless pressure, P_D , as the ratio of the pressure rise needed to inject gas into a fully

surfactant-saturated reservoir to the pressure needed to inject water into the same fully liquid-saturated reservoir at the same volumetric injection rate Q . We calculate the pressure difference between the wellbore and the outer radius by integrating $\nabla p(r)$ between r_w and r_e (Al Ayesh et al., 2017; Ponnars, 2017; Ter Haar, 2018). Assuming a water viscosity of 0.001 *Pa s* the expression for P_D is,

$$P_D = \frac{\int_{r_w}^{r_e} \frac{1}{\lambda_{rt}(S_w)} dr}{\frac{1}{1000} \ln\left(\frac{r_e}{r_w}\right)} \quad (\text{C.1})$$

where $\lambda_{rt}(S_w)$ denotes the total relative mobility of each characteristic. We compute the integral numerically using 300 characteristics equally spaced in saturation from the point of tangency to S_{wr} . **Figure C.1** illustrates the evolution of P_D during the injection of the first gas slug in a surfactant-saturated reservoir for the foam of Experiment 4 for the different fits explored here. In all cases P_D increases abruptly and remains nearly constant until foam breaks through the outer radius (Boeije and Rossen, 2015b).

D

STEADY-STATE FOAM DATA

In **Chapter 4** we focus on data relevant to modelling foam mobility in homogenous porous media. Therefore we recorded local equilibrium data either in the absence of an eruption of a much stronger foam at the core outlet or before this foam eruption started. We did not observe this foam eruption at all in our foam scan with the lowest surfactant concentration (0.037 wt.%) and at the lowest total superficial velocity used in our experiments. **Figure D.1** shows experimental data at one foam quality of this foam scan, where a stronger foam did not erupt at the core outlet even after a prolonged injection period. In this experiment the pressure gradient is nearly independent of gas expansion along the core, as expected in the high-quality regime (Alvarez et al., 2001).

For higher surfactant concentrations and total superficial velocities, we observed eruption of stronger foam at the end of the core at foam breakthrough and subsequent upstream propagation of the stronger foam state, as reported by others (Apaydin and Kavscek, 2001; Nguyen et al., 2003; Simjoo and Zitha, 2015). In these cases we used a foam generator to help achieve local equilibrium before foam breakthrough, as confirmed by the following observations. First, the pressure difference in the first section suggest that foam achieves local equilibrium in the core within the first 8 cm, as illustrated in **Figure D.2**. The pressure gradient is independent of gas superficial velocity (which is altered by gas expansion) along most of the core, as we expect in the high-quality regime. In this paper we report only data before the eruption of a much stronger foam at the core outlet occurred. We discuss steady-state behavior after foam breakthrough in **Chapter 5**.

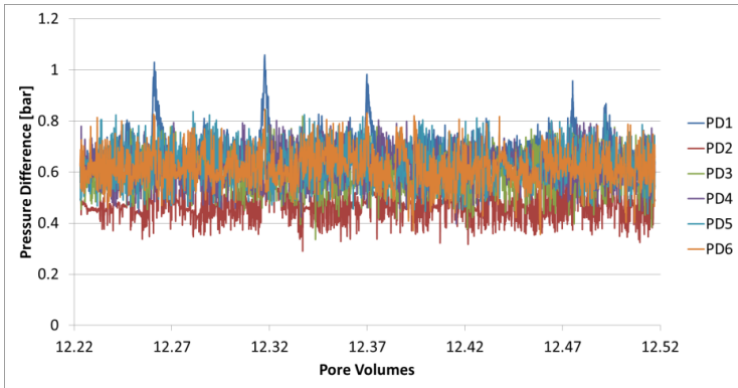


Figure D.1: Experimental data of Experiment 1 at fixed foam quality of 80%.

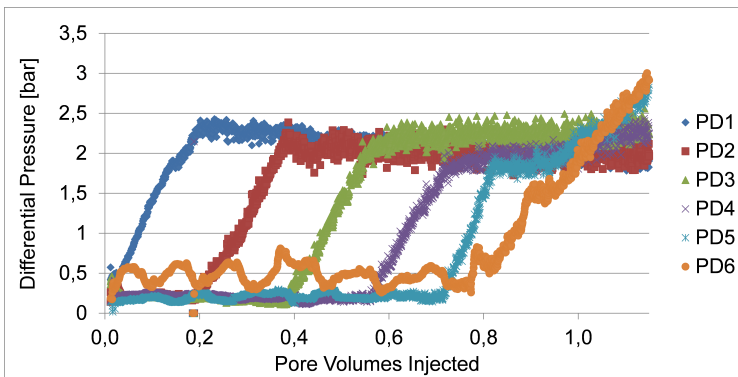


Figure D.2: Experimental data for Experiment 4 at a fixed foam quality of 95%. A stronger foam erupts at the core outlet (Section 6) at about 1.2 PV. Before this, the pressure gradient is nearly uniform along the core, as expected at local equilibrium in the high-quality regime Alvarez et al. (2001).

E

DESCRIPTION OF COMPUTER PROGRAMS FOR NON-NEWTONIAN SAG PROCESSES

We coded in Matlab both the fractional-flow solution and the finite-difference simulator programs. We describe the structure of these programs in the flow diagrams presented in **Figure E.1** and in **Figure E.2**. The codes can be found in Bos and Salazar-Castillo (2019) and in Salazar-Castillo (2019). More details and previous versions of the codes can also be found in Bos (2017), Ponnens (2017) and Ter Haar (2018).

We tested the convergence of both programs. For the fractional-flow theory program, we increased the number of characteristics from 200 to 300 and the number of rings (increments in x_D) from 1000 to 1100. The solutions converged at these resolutions. For the finite-difference simulator, we increased the number of grid blocks. We matched the fractional-flow solution for the Newtonian case using 2500 grid blocks and running the simulation up to a dimensionless time $t_D = 0.01$. Running a simulation with a longer t_D using this grid-block resolution was not possible because of RAM memory limitations. The computation time for the fractional-flow solution was below 1 hour for the cases examined here using a personal computer with 16 GB of RAM and an *Intel i7* processor. Whereas for the finite-difference simulator, the computation time increased exponentially as we increased the number of grid blocks Bos (2017). In order to be able to run the program in a reasonable amount of time (below 2 hours), we had to adjust the length of the simulation by reducing t_D .

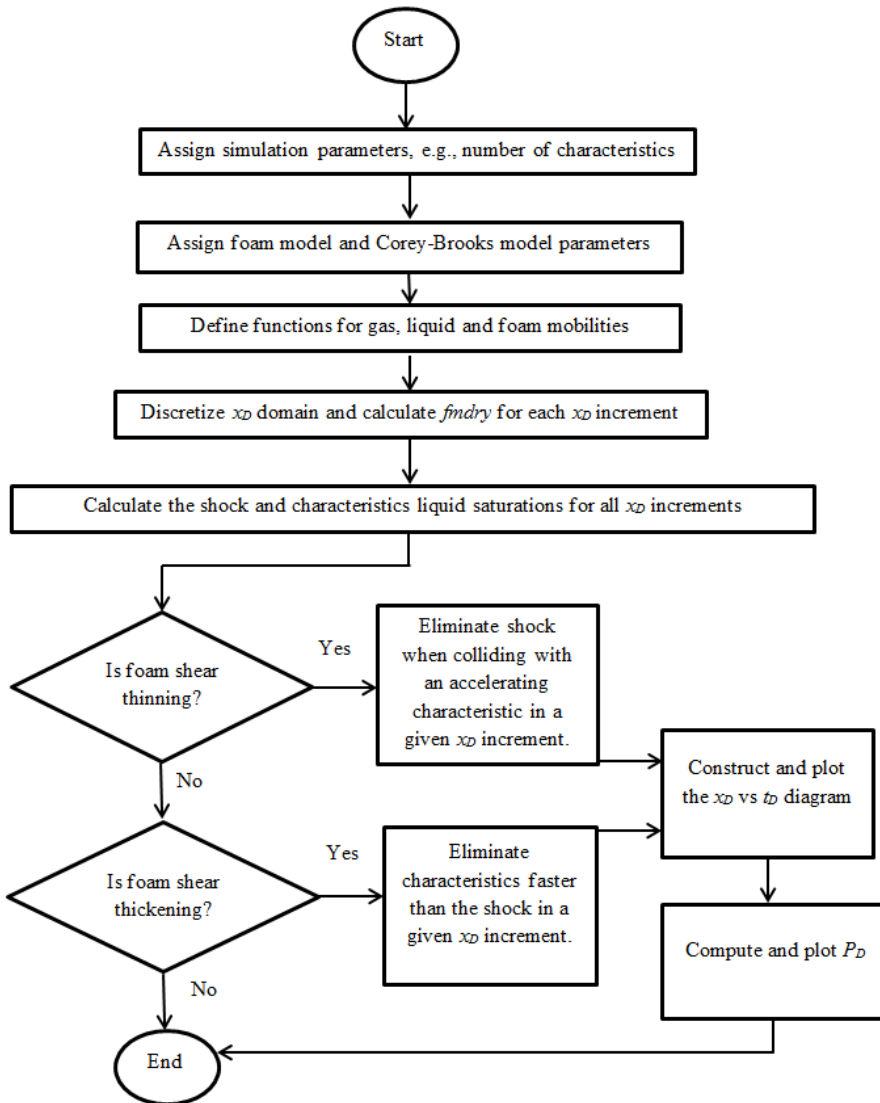


Figure E.1: Flow diagram corresponding to the algorithm for the fractional-flow solution.

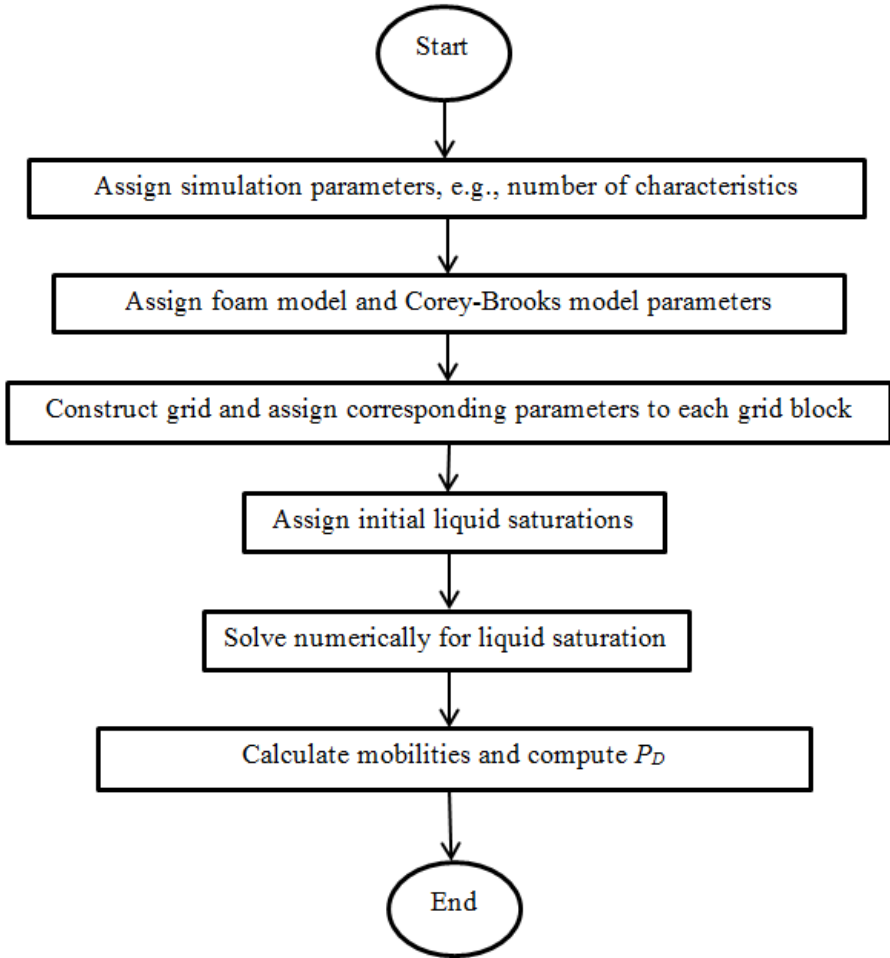


Figure E.2: Flow diagram corresponding to the finite-difference simulator.

BIBLIOGRAPHY

- Al Ayesh, A.H. (2016). “Optimal SAG Design in Heterogeneous Reservoirs: Effect of Permeability on Foam Diversion”. In: *M.Sc, Thesis. TU Delft*. URL: <https://repository.tudelft.nl/islandora/object/uuid%3Ad2d395a1-3cb5-43e6-88bd-c2e7b0ce88af>.
- Al Ayesh, A.H. et al. (2017). “Foam Diversion in Heterogeneous Reservoirs: Effect of Permeability and Injection Method”. In: *SPE Journal*. *SPE-179650-22*(05). DOI: [10.2118/179650-PA](https://doi.org/10.2118/179650-PA).
- Alvarez, J. M., H. Rivas, and W.R. Rossen (2001). “A Unified Model for Steady-State Foam Behavior at High and Low Foam Qualities”. In: *SPE Journal* *SPE-74141-PA* 6, pp. 325–333. DOI: [10.2118/74141-PA](https://doi.org/10.2118/74141-PA).
- Apaydin, O.G. and A.R. Kovscek (2001). “Surfactant Concentration and End Effects on Foam Flow in Porous Media”. In: *Transport in Porous Media* 43(3), pp. 511–536. DOI: [10.1023/A:1010740811277](https://doi.org/10.1023/A:1010740811277).
- Ashoori, E., T.L.M. van der Heijden, and W.R. Rossen (2010). “Fractional-Flow Theory of Foam Displacements with Oil”. In: *SPE Journal*. *SPE-121579-PA* 15(02). DOI: [10.2118/121579-PA](https://doi.org/10.2118/121579-PA).
- Ashoori, E., D. Marchesin, and W.R. Rossen (2011a). “Dynamic Foam Behavior in the Entrance Region of a Porous Medium”. In: *Colloids Surfaces A: Physicochem. Eng. Aspects* 377, pp. 217–227. DOI: [10.1016/j.colsurfa.2010.12.043](https://doi.org/10.1016/j.colsurfa.2010.12.043).
- (2011b). “Roles of Transient and Local Equilibrium Foam Behavior in Porous Media: Traveling Wave”. In: *Colloids Surfaces A: Physicochem. Eng. Aspects* 377, 228–242. DOI: [10.1016/j.colsurfa.2010.12.042](https://doi.org/10.1016/j.colsurfa.2010.12.042).
- (2012). “Multiple Foam States and Long-Distance Foam Propagation in Porous Media”. In: *SPE Journal* *SPE-154024-PA* 17, pp. 1231–1245. DOI: [10.2118/154024-PA](https://doi.org/10.2118/154024-PA).
- Bird, R.B., W.E. Stewart, and E.N. Lightfoot (2006). *Transport Phenomena*. New York: 2nd Edition revised, John Wiley and Sons. ISBN: 978-0-470-11539-8.
- Birol, F. (2019). “The Future of Global Energy Markets: Implications for Security, Sustainability and Economic Growth”. In: *International Energy Agency*. URL: <https://www.tudelft.nl/en/energy/meet-the-energy-leaders/meet-the-energy-leader-fatih-birol/>.
- Birol, F. et al. (2018). “World Energy Outlook”. In: *International Energy Agency*. URL: <https://www.iea.org/weo2018/>.
- Blaker, T. et al. (2002). “Foam for Gas Mobility Control in the Snorre Field: the FAWAG Project”. In: *SPE Reservoir Evaluation and Engineering*. *SPE-78824-PA* 5(04). DOI: [10.2118/78824-PA](https://doi.org/10.2118/78824-PA).

- Boeije, C.S. and W.R. Rossen (2015a). "Fitting foam-simulation-model parameters to data: I. co-injection of gas and liquid". In: *SPE Reservoir Evaluation and Engineering* 18(2), pp. 264–272. DOI: [10.2118/174544-PA](https://doi.org/10.2118/174544-PA).
- (2015b). "Gas Injection Rate Needed for SAG Foam Processes to Overcome Gravity Override". In: *SPE Journal SPE-166244-PA* 20(01), pp. 49–59. DOI: [10.2118/166244-PA](https://doi.org/10.2118/166244-PA).
- (2018). "SAG foam flooding in carbonate rocks". In: *Journal of Petroleum Science and Engineering* 171, pp. 843–853. DOI: [10.1016/j.petrol.2018.08.017](https://doi.org/10.1016/j.petrol.2018.08.017).
- Bond, D.C. and O.C. Holbrook (1958). "Gas Drive Oil Recovery Process". In: *US Patent* 2866507.
- Bos, M. (2017). "Numerical Simulation of Radial Non-Newtonian Foam Flow in a Reservoir". In: *B.Sc, Thesis. TU Delft*. URL: <https://repository.tudelft.nl/islandora/object/uuid:3485b873-142c-4987-b6d8-f53390cf7919?collection=education>.
- Bos, M. and R.O. Salazar-Castillo (2019). *Finite-Difference Simulator for Newtonian and non-Newtonian SAG Gas Injection*. URL: <https://github.com/RockdrigoCastle/finitedifference-nonNewtonian-SAG-GasInjection>.
- Chen, P. and K. K. Mohanty (2014). "Wettability Alteration in High Temperature Carbonate Reservoirs". In: *SPE Improved Oil Recovery Symposium, Tulsa, OK, USA. SPE-169125-MS*. DOI: [10.2118/169125-MS](https://doi.org/10.2118/169125-MS).
- Cheng, L. et al. (2000). "Simulating Foam Processes at High and Low Foam Qualities". In: *SPE Journal SPE-59287-MS*. DOI: [10.2118/59287-MS](https://doi.org/10.2118/59287-MS).
- Cheng, L. et al. (2002). "Simulation of Dynamic Foam-Acid Diversion Processes". In: *SPE Journal. SPE-79639-PA* 7(03). DOI: [10.2118/79639-PA](https://doi.org/10.2118/79639-PA).
- CMG, Computer Modeling Group (2015). *STARS User's Guide*.
- Eftekhari, A.A. and R. Farajzadeh (2017). "Effect of Foam on Liquid Phase Mobility in Porous Media". In: *Scientific Reports* 7, p. 43870. DOI: [10.1038/srep43870](https://doi.org/10.1038/srep43870).
- Ettinger, R.A. and C.J. Radke (1992). "Influence of Texture on Steady Foam Flow in Berea Sandstone". In: *SPE Reservoir Engineering SPE-19688-PA* 7(01). DOI: [10.2118/19688-PA](https://doi.org/10.2118/19688-PA).
- Falls, A.H. et al. (1988). "Development of a Mechanistic Foam Simulator: The Population Balance and Generation by Snap-Off". In: *SPE Reservoir Engineering SPE-14961-PA* 3(03), pp. 884–892. DOI: [10.2118/14961-PA](https://doi.org/10.2118/14961-PA).
- Farajzadeh, R. et al. (2012). "Foam-Oil Interaction in Porous Media: Implications for Foam Assisted Enhanced Oil Recovery". In: *Advances in Colloid and Interface Science* 183-184, pp. 1–13. DOI: [10.1016/j.cis.2012.07.002](https://doi.org/10.1016/j.cis.2012.07.002).
- Farajzadeh, R. et al. (2015). "Effect of Permeability on Implicit-Texture Foam Model Parameters and the Limiting Capillary Pressure". In: *Energy and Fuels* 29(05), pp. 3011–3018. DOI: [10.1021/acs.energyfuels.5b00248](https://doi.org/10.1021/acs.energyfuels.5b00248).
- Farajzadeh, R. et al. (2016). "Simulation of Instabilities and Fingering in Surfactant Alternating Gas (SAG) Foam Enhanced Oil Recovery". In: *Journal of Natural Gas*

- Science and Engineering* 34, pp. 1191–1204. DOI: [10.1016/j.jngse.2016.08.008](https://doi.org/10.1016/j.jngse.2016.08.008).
- Fisher, A.W., R.W.S. Foulser, and S.G. Goodyear (1990). “Mathematical Modeling of Foam Flooding”. In: *SPE/DOE Symposium on Enhanced Oil Recovery, Tulsa, OK, USA. SPE-20195-MS*. DOI: [10.2118/20195-MS](https://doi.org/10.2118/20195-MS).
- Friedmann, F., W. H. Chen, and P. A. Gauglitz (1991). “Experimental and Simulation Study of High-Temperature Foam Displacement in Porous Media”. In: *SPE Reservoir Engineering SPE-17357-PA* 6, pp. 37–75. DOI: [10.2118/17357-PA](https://doi.org/10.2118/17357-PA).
- Gauglitz, P.A. et al. (2002). “Foam Generation in Homogeneous Porous Media”. In: *Chemical Engineering Science* 57, pp. 4037–4052. DOI: [10.1016/S0009-2509\(02\)00340-8](https://doi.org/10.1016/S0009-2509(02)00340-8).
- Gong, J. et al. (2019a). “Injectivity of Multiple Gas and Liquid Slugs in SAG Foam EOR: A CT Scan Study”. In: *IOR 2019 – 20th European Symposium on Improved Oil Recovery. Pau, France*. DOI: [10.3997/2214-4609.201900107](https://doi.org/10.3997/2214-4609.201900107).
- Gong, J. et al. (2019b). “Modelling of Liquid Injectivity in Surfactant-Alternating-Gas Foam Enhanced Oil Recovery”. In: *SPE Journal. SPE-190435-PA*. DOI: [10.2118/190435-PA](https://doi.org/10.2118/190435-PA).
- Grassia, P. et al. (2014). “Analysis of a Model for Foam Improved Oil Recovery”. In: *Journal of Fluid Mechanics* 751, pp. 346–405. DOI: [10.1017/jfm.2014.287](https://doi.org/10.1017/jfm.2014.287).
- Heller, J.P. (1994). “CO₂ Foams in Enhanced Oil Recovery in Foams: Fundamentals and Applications in the Petroleum Industry”. In: *Petroleum Industry, ed. M. J. Comstock, Chap. 5. Advances in Chemistry, Washington, DC, USA. American Chemical Society*. 242, pp. 201–234. DOI: [10.1021/ba-1994-0242.fw001](https://doi.org/10.1021/ba-1994-0242.fw001).
- Hirasaki, G.J. et al. (1997). “Surfactant/Foam Process for Aquifer Remediation”. In: *International Symposium on Oilfield Chemistry, Houston, Texas. SPE-37257-MS*. DOI: [10.2118/37257-MS](https://doi.org/10.2118/37257-MS).
- Islam, M.R. and S.M. Farouq-Ali (1990). “Numerical Simulation of Foam Flow in Porous Media”. In: *Journal of Canadian Petroleum Technology. PETSOC-90-04-03* 29(04), pp. 47–51. DOI: [10.2118/90-04-03](https://doi.org/10.2118/90-04-03).
- Kahrobaei, S., S. Vincent-Bonnieu, and R. Farajzadeh (2017). “Experimental Study of Hysteresis behavior of Foam Generation in Porous Media”. In: *Scientific Reports* 7, p. 8986. DOI: [10.1038/s41598-017-09589-0](https://doi.org/10.1038/s41598-017-09589-0).
- Kam, S. I., Q. P. Nguyen, and W. R. Rossen (2007). “Dynamic Simulations With an Improved Model for Foam Generation”. In: *SPE Journal SPE-90938-PA* 12, pp. 35–48. DOI: [10.2118/90938-PA](https://doi.org/10.2118/90938-PA).
- Kam, S.I. and W.R. Rossen (2003). “A Model for Foam Generation in Homogeneous Porous Media”. In: *SPE Journal. SPE-87334-PA* 8(04), pp. 417–425. DOI: [10.2118/87334-PA](https://doi.org/10.2118/87334-PA).
- Kapetas, L., W.A. van El, and W.R. Rossen (2014). “Representing Slow Foam Dynamics in Laboratory Corefloods for Enhanced Oil Recovery”. In: *SPE Improved Oil Recovery Symposium held in Tulsa, Oklahoma, USA. SPE-169059-MS*. DOI: [10.2118/169059-MS](https://doi.org/10.2118/169059-MS).

- Kapetas, L. et al. (2017). "Effect of Permeability on Foam-Model Parameters: an Integrated Approach from Core-Flood Experiments Through to Foam Diversion Calculations". In: *Colloids and Surfaces A: Physicochemical and Engineering Aspects* 530, pp. 172–180. DOI: [10.1016/j.colsurfa.2017.06.060](https://doi.org/10.1016/j.colsurfa.2017.06.060).
- Khatib, Z.I., G.J. Hirasaki, and A.H. Falls (1988). "Effects of Capillary Pressure on Coalescence and Phase Mobilities in Foams Flowing Through Porous Media". In: *Society of Petroleum Engineers SPE-15442-PA* 3(03). DOI: [10.2118/15442-PA](https://doi.org/10.2118/15442-PA).
- Kibodeaux, K.R. and W.R. Rossen (1997). "Coreflood Study of Surfactant-Alternating-Gas Foam Processes: Implications for Field Design". In: *SPE Western Regional Meeting SPE-38318-MS*. DOI: [10.2118/38318-MS](https://doi.org/10.2118/38318-MS).
- Kloet, M.B., W.J. Renkema, and W.R. Rossen (2009). "Optimal Design Criteria for SAG Foam Processes in Heterogeneous Reservoirs". In: *SPE EUROPEC/EAGE Annual Conference and Exhibition. SPE-121581-MS. Amsterdam, The Netherlands*. DOI: [10.2118/121581-MS](https://doi.org/10.2118/121581-MS).
- Kovscek, A. R. and C. J. Radke (1994). "Fundamentals of Foam Transport in Porous Media." In: *Number 242 in Advances in Chemistry Series. American Chemical Society, Washington, DC, USA*. DOI: [10.1021/ba-1994-0242.ch003](https://doi.org/10.1021/ba-1994-0242.ch003).
- Kovscek, A.R., T.W. Patzek, and C.J. Radke (1995). "A mechanistic population balance model for transient and steady-state foam flow in Boise sandstone". In: *Chemical Engineering Science* 50(23), pp. 3798–3799. DOI: [10.1016/0009-2509\(95\)00199-F](https://doi.org/10.1016/0009-2509(95)00199-F).
- Kovscek, A.R., Q. Chen, and M. Gerritsen (2010). "Modeling Foam Displacement With the Local-Equilibrium Approximation: Theory and Experimental Verification". In: *SPE Journal. SPE-116735-PA* 15(01). DOI: [10.2118/116735-PA](https://doi.org/10.2118/116735-PA).
- Kular, G.S., K. Lowe, and D. Coombe (1989). "Foam Application in an Oil Sands Steam Flood Process". In: *SPE Annual Tech. Conf. and Exhibition, San Antonio, TX, USA. SPE-19690-MS*. DOI: [10.2118/SPE-19690-MS](https://doi.org/10.2118/SPE-19690-MS).
- Lake, L.W., L.B. Steven, and A.N. Araque-Martinez (2003). *Geochemistry and Fluid Flow*. Elsevier. ISBN: 978-0444505699.
- Lake, L.W. et al. (2014). *Fundamentals of Enhanced Oil Recovery*. Richardson, TX: Society of Petroleum Engineers. ISBN: 978-1-61399-328-6.
- Law, D.H., Z.-M. Yang, and T.W. Stone (1992). "Effect of Presence of Oil on Foam Performance: A Field Simulation Study". In: *SPE Reservoir Engineering SPE-18421-PA* 7(02)). DOI: [10.2118/18421-PA](https://doi.org/10.2118/18421-PA).
- Le, V.Q., Q.P. Nguyen, and A.W. Sanders (2008). "A Novel Foam Concept with CO₂ Dissolved Surfactants". In: *SPE/DOE Symposium on Improved Oil Recovery, Tulsa, OK, USA. SPE-113370-PA*.
- Leeftink, T.N., C.A. Latooij, and W.R. Rossen (2015). "Injectivity Errors in Simulation of Foam EOR". In: *Journal of Petroleum Science and Engineering* 126, pp. 26–34. DOI: [10.1016/j.petrol.2014.11.026](https://doi.org/10.1016/j.petrol.2014.11.026).

- Lotfollahi, M. et al. (2016). "Comparison of implicit-texture and population-balance foam models". In: *Journal of Natural Gas Science and Engineering* 31, pp. 84–197. ISSN: 1875-5100. DOI: [10.1016/j.jngse.2016.03.018](https://doi.org/10.1016/j.jngse.2016.03.018).
- Lotfollahi, M. et al. (2017). "Foam Generation Hysteresis in Porous Media: Experiments and New Insights". In: *Transport in Porous Media* 116, 687–703. DOI: [10.1007/s11242-016-0796-6](https://doi.org/10.1007/s11242-016-0796-6).
- Matthews, C. S (1989). "Carbon Dioxide Flooding". In: *Developments in Petroleum Science* 17 part B, pp. 129–156. DOI: [10.1016/S0376-7361\(08\)70458-8](https://doi.org/10.1016/S0376-7361(08)70458-8).
- Mohammadi, S. and D.A. Coombe (1992). "Characteristics of Steam-Foam Drive Process in Massive Multi-Zone and Thin Single-Zone Reservoirs". In: *SPE Western Regional Meeting, Bakersfield, CA, USA. SPE-14030-MS*. DOI: [10.2118/14030-MS](https://doi.org/10.2118/14030-MS).
- Moradi-Araghi, A. et al. (1997). "Laboratory Evaluation of Surfactants for CO₂-Foam Applications at the South Cowden Unit". In: *International Symposium on Oilfield Chemistry, Houston, Texas, USA. SPE-37218-MS*. DOI: [10.2118/37218-MS](https://doi.org/10.2118/37218-MS).
- Namdar Zanganeh, M. et al. (2014). "Challenges to Adjoint-Based Optimization of a Foam EOR Process". In: *Computational Geosciences* 18.3-4, 563–577. DOI: [10.1007/s10596-014-9412-4](https://doi.org/10.1007/s10596-014-9412-4).
- Namdar-Zanganeh, M.N. et al. (2011). "The Method of Characteristics Applied to Oil Displacement by Foam". In: *SPE Journal. SPE-121580-PA* 16(01). DOI: [10.2118/121580-PA](https://doi.org/10.2118/121580-PA).
- Nguyen, Q. P. et al. (2009). "Determination of Gas Trapping With Foam Using X-Ray Computed Tomography and Effluent Analysis". In: *SPE Journal SPE-94764-PA* 14(02). DOI: [10.2118/94764-PA](https://doi.org/10.2118/94764-PA).
- Nguyen, Q.P., P. K. Currie, and P.L.J. Zitha (2003). "Determination of Foam Induced Fluid Partitioning in Porous Media Using X-Ray Computed Tomography". In: *Society of Petroleum Engineers SPE-80245-MS*. DOI: [10.2118/80245-MS](https://doi.org/10.2118/80245-MS).
- Norris, S. et al. (2014). "CO₂ Foam Pilot in Salt Creek Field, Natrona County, WY: Phase II: Diagnostic Testing and Initial Results". In: *SPE Annual Technical Conference and Exhibition, Amsterdam, The Netherlands. SPE-170729-MS*. DOI: [10.2118/170729-MS](https://doi.org/10.2118/170729-MS).
- Osterloh, W.T. and M. J. Jante (1992). "Effects of Gas and Liquid Velocity on Steady-State Foam Flow at High Temperature". In: *Society of Petroleum Engineers SPE-24179-MS*. DOI: [10.2118/24179-MS](https://doi.org/10.2118/24179-MS).
- Patzek, T.W. and N.A. Myhill (1989). "Simulation of the Bishop Steam Foam Pilot". In: *SPE California Regional Meeting, Bakersfield, USA. SPE-18786-MS*. DOI: [10.2118/18786-MS](https://doi.org/10.2118/18786-MS).
- Persoff, P. et al. (1991). "A Laboratory Investigation of Foam Flow in Sandstone at Elevated Pressure". In: *SPE Reservoir Engineering SPE-18781-PA* 6(03), pp. 185–192. DOI: [10.2118/18781-PA](https://doi.org/10.2118/18781-PA).
- Pickup, G.E., M. Jin, and E.J. Mackay (2012). "Simulation of Near-Well Pressure Build-Up in Models of CO₂ Injection". In: *European Conference on the Mathematics of Oil Recovery, Biarritz, France. Paper B34*. DOI: [10.3997/2214-4609.20143238](https://doi.org/10.3997/2214-4609.20143238).

- Ponners, C.G. (2017). "SAG Foam EOR: Buckley-Leverett Fractional-Flow Theory for Non-Newtonian Foam Rheologies". In: *B.Sc, Thesis. TU Delft*. URL: <http://resolver.tudelft.nl/uuid:59f12b6a-2698-44b2-a20e-f64ec408fe47>.
- Ransohoff, T.C. and C.J. Radke (1988). "Mechanism of foam generation on glass-bead packs". In: *SPE Reservoir Engineering SPE-15441-PA3(02)*, 573–585. DOI: [10.2118/15441-PA](https://doi.org/10.2118/15441-PA).
- Rossen, W. R. et al. (2011). "Fractional Flow Theory Applicable to Non-Newtonian Behavior in EOR Processes". In: *Transport Porous Media* 89, pp. 213–236. DOI: [10.1007/s11242-011-9765-2](https://doi.org/10.1007/s11242-011-9765-2).
- Rossen, W. R. et al. (2017). "Long-Time Diversion in SAG Foam Enhanced Oil Recovery From Field Data". In: *SPE Reservoir Evaluation and Engineering. SPE-170809-PA 20(01)*. DOI: [10.2118/170809-PA](https://doi.org/10.2118/170809-PA).
- Rossen, W.R (1996). "Foams in Enhanced Oil Recovery". In: *Foams: Theory, Measurements and Applications. R. K. Prud'homme and S.Khan, ed. Marcell Dekker*.
- Rossen, W.R. (2013). "Numerical Challenges in Foam Simulation: A Review". In: *SPE Annual Technical Conference and Exhibition, New Orleans, Louisiana, USA. SPE-166232-MS*. DOI: [10.2118/166232-MS](https://doi.org/10.2118/166232-MS).
- Rossen, W.R. and C.S. Boeije (2015). "Fitting Foam-Simulation-Model Parameters to Data: II. Surfactant-Alternating-Gas Foam Applications". In: *SPE Reservoir Evaluation and Engineering SPE-165282-PA 18(02)*. DOI: [10.2118/165282-PA](https://doi.org/10.2118/165282-PA).
- Rossen, W.R. and J. Bruining (2007). "Foam Displacements with Multiple Steady States". In: *SPE Journal SPE-89397-PA 12(01)*, pp. 5–18. DOI: [10.2118/89397-PA](https://doi.org/10.2118/89397-PA).
- Rossen, W.R. and Z.H. Zhou (1995). "Modelling Foam Mobility at the 'Limiting Capillary Pressure'". In: *SPE Advanced Technology Series SPE-22627-PA*. DOI: [10.2118/22627-PA](https://doi.org/10.2118/22627-PA).
- Rossen, W.R. et al. (1999). "Simplified Mechanistic Simulation of Foam Processes in Porous Media". In: *SPE Journal. SPE-57678-PA 4*, pp. 279–287. DOI: [10.2118/57678-PA](https://doi.org/10.2118/57678-PA).
- Rossen, W.R. et al. (2010). "Injection Strategies to Overcome Gravity Segregation in Simultaneous Gas and Water Injection Into Homogeneous Reservoirs". In: *SPE Journal SPE-99794-PA 15*, pp. 76–90. DOI: [10.2118/99794-PA](https://doi.org/10.2118/99794-PA).
- Salazar-Castillo, R.O. (2019). *Fractional-flow solution program for non-Newtonian SAG foam displacements: Injection of the first gas slug*. URL: <https://github.com/RockdrigoCastle/fft-SAG-nonNew-GasInjection>.
- Schramm, L.L. (1994). *Fundamentals and Applications in the Petroleum Industry*. Washington, D.C.: American Chemical Society. ISBN: 9780841227194. DOI: [10.1021/ba-1994-0242](https://doi.org/10.1021/ba-1994-0242).
- Shah, S.Y. et al. (2019a). "Foam Generation by Capillary Snap-Off in Flow Across a Sharp Permeability Transition". In: *SPE Journal. SPE-190210-PA 24(01)*. DOI: [10.2118/190210-PA](https://doi.org/10.2118/190210-PA).
- Shah, S.Y. et al. (2019b). "Foam generation by snap-off in flow across a sharp permeability transition". In: *EAGE IOR Symposium, Pau, France*.

- Shan, D. and W.R. Rossen (2004). "Optimal Injection Strategies for Foam IOR". In: *SPE Journal SPE-88811-PA* 9, pp. 132–150. DOI: [10.2118/88811-PA](https://doi.org/10.2118/88811-PA).
- Simjoo, M. and P.L.J. Zitha (2015). "Modeling of Foam Flow Using Stochastic Bubble Population Model and Experimental Validation". In: *Transport in Porous Media* 107(3), pp. 799–820. DOI: [10.1007/s11242-015-0468-y](https://doi.org/10.1007/s11242-015-0468-y).
- Skauge, A. et al. (2002). "Foam-Assisted WAG: Experience from the Snorre Field". In: *SPE/DOE Improved Oil Recovery Symposium, Tulsa, Oklahoma, USA. SPE-75157-MS*. DOI: [10.2118/75157-MS](https://doi.org/10.2118/75157-MS).
- Stone, H.L. (2004). "A Simultaneous Water and Gas Flood Design with Extraordinary Vertical Gas Sweep". In: *International Petroleum Conference SPE-91724-MS*.
- Tanzil, D., G.J. Hirasaki, and C.A. Miller (2002). "Conditions for Foam Generation in Homogeneous Porous Media". In: *SPE/DOE Improved Oil Recovery Symposium, Tulsa, Oklahoma, USA. SPE-75176-MS*. DOI: [10.2118/75176-MS](https://doi.org/10.2118/75176-MS).
- Ter Haar, S.F. (2018). "A Buckley-Leverett Model for Non-Newtonian SAG for Enhanced Oil Recovery". In: *B.Sc. Thesis. TU Delft*. URL: <http://resolver.tudelft.nl/uuid:a735e5df-1c63-4369-9eb9-0c2648b48222>.
- van der Meer, J. et al. (2018). "Influence of foam on the stability characteristics of immiscible flow in porous media". In: *Physics of Fluids* 30(1). DOI: [10.1063/1.5000891](https://doi.org/10.1063/1.5000891).
- Velde Harsenhorst, R.M. de et al. (2014). "Extension and Verification of a Simple Model for Vertical Sweep in Foam Surfactant-Alternating-Gas Displacements". In: *SPE Reservoir Evaluation and Engineering. SPE-164891-PA*. 17(03). DOI: [10.2118/164891-PA](https://doi.org/10.2118/164891-PA).
- Wassmuth, R.F., K.A. Green, and L. Randall (2001). "Details of In-Situ Foam Propagation Exposed With Magnetic Resonance Imaging". In: *SPE Reservoir Evaluation and Engineering. SPE-71300-PA* 4(02), pp. 135–145. DOI: [10.2118/71300-PA](https://doi.org/10.2118/71300-PA).
- Wu, Y., P. Karsten, and Z.X. Chen (1993). "Buckley-Leverett Flow in Composite Porous Media". In: *SPE Advanced Technology Series. SPE-22329-PA* 1(02). DOI: [10.2118/22329-PA](https://doi.org/10.2118/22329-PA).
- Xing, D. et al. (2012). " CO_2 -Soluble, Nonionic, Water-Soluble Surfactants That Stabilize CO_2 -in-Brine Foams". In: *SPE Journal SPE-129907-PA* 17(04). DOI: [10.2118/129907-PA](https://doi.org/10.2118/129907-PA).
- Xu, Q. and W. R. Rossen (2004). "Experimental Study of Gas Injection in Surfactant-Alternating-Gas Foam Process". In: *SPE Reservoir Evaluation and Engineering. SPE-84183-PA*. 7(06), pp. 438–448. DOI: [10.2118/84183-PA](https://doi.org/10.2118/84183-PA).
- Yu, G., W.R. Rossen, and S. Vincent-Bonnieu (2019a). "Coreflood Study of Effect of Surfactant Concentration on Foam Generation in Porous Media". In: *Journal of Industrial and Engineering Chemistry* 30(1). DOI: [10.1021/acs.iecr.8b03141](https://doi.org/10.1021/acs.iecr.8b03141).
- Yu, G., S. Vincent-Bonnieu, and W.R. Rossen (2019b). "Foam Propagation at Low Superficial Velocity: Implications for Long-Distance Foam Propagation". In: *EAGE IOR Symposium, Pau, France*. DOI: [10.3997/2214-4609.201900108](https://doi.org/10.3997/2214-4609.201900108).

- Zhou, Z.H. and W.R. Rossen (1994). "Applying Fractional-Flow Theory to Foams for Diversion in Matrix Acidization". In: *SPE Production and Facilities*. SPE-24660-PA 9, pp. 29–35. DOI: [10.2118/24660-PA](https://doi.org/10.2118/24660-PA).
- (1995). "Applying Fractional-Flow Theory to Foam Processes at the 'Limiting Capillary Pressure'". In: *SPE Advance Technology Series*. SPE-24180-PA 3(01), pp. 154–162. DOI: [10.2118/24180-PA](https://doi.org/10.2118/24180-PA).

ACKNOWLEDGEMENTS

Many thanks to all the people who directly or indirectly contributed to the completion of this project.

First, I want to thank **God** for being my light in the most difficult moments.

To my advisor, **Prof. William Rossen**, thank you for sharing your knowledge, for giving me the space to explore my ideas, for the countless talks we had, for pointing me to the right direction and especially for not giving up and for helping me to keep this project on track. My career as a Petroleum Engineer could not have started without your help. To **Janice Rossen** thank you for your friendship and your art. To **Claire Taylor** thank you for your feedback on my manuscripts. Thank you for your advice on living in the Netherland with children. Thanks to you I did not have to choose between having a family and finishing my Ph.D.

To **Prof. Dr. Michael A Hicks, Prof. Dr. R.A.W.M. Henkes, Dr. Denis Voskov, Dr. Frederich Douarche, Dr. Kun Ma** and **Dr. Frank van der Heyden**; independent members of the Doctoral Committee for your kind comments and feedback on my thesis. Special thanks to **Dr. Voskov** for giving the opportunity to assist him in the course **Properties of Subsurface Fluids** during two years.

To **Michiel Slob, Jolanda van Haagen, Karel Heller, Ellen Meijvogel-de Koning** and **Marc Friebel** for their invaluable technical assistance with our experiments. Special thanks to **Michiel** for his assistance in building the setup I used for two years and for the countless interesting discussions we had.

To **Dr. Patricia Olguin Lora** and **Dr. Andrés Moctezuma Berthier**; advisors from the Instituto Mexicano del Petróleo (IMP). Thank you for your feedback on my reports. To **Dr. Erick Luna Rojero** for introducing me to Prof. William Rossen. To **Leticia Mojica Zavaleta** for her assistance during the selection process of the program PCTRES. To **Gabriela Garcia Haro** for being my contact with IMP during my Ph.D. studies.

To **Ahmed Al-Ayesh, Martijn Bos, Christopher Ponnens** and **Sterre ter Haar**. Thank you for your invaluable contribution to this thesis through your bachelor and master theses. I was honored to be your supervisor. Also to **Lily Qian** who I also supervised during her bachelor thesis. Unfortunately, her thesis did not make it to this doctoral thesis.

To all the guys from the Petroleum Section. Special thanks to **Ahmed, Brandon, Jinyu, Kai, Jiakun, Mark, Martijn, Swej, Xiaocong** and **Xu**. Special thanks to Ahmed for translating my summary into dutch. To **Dr. Sian Jones** for helping me in getting started with my experiments. I apologize in advance is case I forgot to mention somebody.

To my Mexican friends **Dr. Gabriela Díaz** and **Dr. Luis de la Peña**. Thank you for having me at your apartment while I was looking for a place to live. Thank you **Gaby** for being such a nice friend and for preparing Margaritas. I like your charisma. Thank you **Luis** for your friendship and for the lunches we had. I really enjoyed the conversations and views. We have still more adventures to live.

I thank my family. **Bibiana** you are the love of my life. *Sin ti, no. Sin ti, ni un paso más*. Many thanks for giving your love when I needed it the most. In only one thing I feel smarter than Einstein, I did not lose my Mileva. To my daughter, **Lidia Estefania** you are the light in my eyes. You are my example of strength and gratitude. To **Rodrigo Oswaldo**, my son, you are my proud and my blood. You have the talents of your parents and more. To my mother, **María Olga**, thank you for being my first teacher. Thank you for your unconditional love and support. Thank you for always having time to listen. To my father, **Oswaldo Virgilio**, thank you for teaching me to value my personality. Your encouragement words are always with me. When nobody believes in me, you do. To my grandmother, **María Esther**, thank you for your love. Thank you for showing me that a degree does not make you smarter. Thank you for teaching me the value of having a family. Thank you for taking care of me, sometimes even in my dreams. To my brother, **Oswaldo Israel** and his wife **Isabel** for visiting me in the Netherlands and having such a nice time together. To my younger brother, **Luis Alfredo**, for always being supportive and for taking care of our parents while I was abroad.

To **Timoteo, Fernanda, Leticia, Julian** and **Argelia** for their support to Bibi and the children while I was abroad.

Finally, I want to thank the dutch society for their hospitality and open-minded attitude. I could not have chosen a better place to do my Ph.D. and to raise children at the same time.

CURRICULUM VITÆ

Rodrigo Orlando SALAZAR CASTILLO

19-10-1985 Born in Puebla, Puebla, Mexico.

EDUCATION

- 2007-2012 B.Sc. Applied Physics. Optoelectronics and Photonics.
Benemérita Universidad Autónoma de Puebla
Thesis: Analysis of DMP-Na⁺ Complexes Obtained through DFT Calculations.
Promotors: Prof. Valeri Poltev and Prof. Alexandra Deriabina.
- 2013-2015 M.Sc. Applied Physics (*Cum Laude*). Computational Biophysics.
Benemérita Universidad Autónoma de Puebla
Thesis: Computational Study of DNA fragments
Promotors: Prof. Valeri Poltev and Prof. Alexandra Deriabina.
- 2015-2019 Ph.D. Petroleum Engineering and Geosciences.
TU Delft
Thesis: Scale up of Surfactant Alternating Gas Foam Processes.
Promotor: Prof. William Rossen.

LIST OF PUBLICATIONS

4. **Salazar, R. and Rossen W.;** , *Scale-up of Laboratory Data for Surfactant-Alternating-Gas Foam EOR.*, To submitted to the SPE Journal.
3. **Salazar, R., Ter Haar, S., Ponnens, C.G., Bos and Rossen, W.;** , *Fractional-Flow Theory for Non-Newtonian Surfactant-Alternating-Gas Foam Processes*, Under Review in the Journal of Transport in Porous Media.
2. **Salazar, R. and Rossen, W. ,** *Coreflood Study of Non-Monotonic Fractional-Flow Behavior with Foam: Implications for Surfactant-Alternating-Gas Foam EOR*, [IOR 2019 – 20th European Symposium on Improved Oil Recovery](#) .
1. **Al Ayesh, A. H., Salazar, R., Farajzadeh, R., Vincent-Bonnieu, S., and Rossen, W. R. ,** *Foam Diversion in Heterogeneous Reservoirs: Effect of Permeability and Injection Method.*, [SPE Journal SPE-179650-PA](#).